Iowa State University
Digital Repository

Graduate Theses and Dissertations

Iowa State University Capstones, Theses and Dissertations

2017

Optical-based spectroscopic methods for measuring chemical, optical, and physical properties of thin polymer waveguide films

Jonathan M. Bobbitt
Iowa State University

Follow this and additional works at: https://lib.dr.iastate.edu/etd

Part of the Analytical Chemistry Commons

Recommended Citation
Bobbitt, Jonathan M., "Optical-based spectroscopic methods for measuring chemical, optical, and physical properties of thin polymer waveguide films" (2017). *Graduate Theses and Dissertations*. 15491.
https://lib.dr.iastate.edu/etd/15491

This Dissertation is brought to you for free and open access by the Iowa State University Capstones, Theses and Dissertations at Iowa State University Digital Repository. It has been accepted for inclusion in Graduate Theses and Dissertations by an authorized administrator of Iowa State University Digital Repository. For more information, please contact digirep@iastate.edu.

المنارة للاستشارات

www.manaraa.com

Optical-based spectroscopic methods for measuring chemical, optical, and physical properties of thin polymer waveguide films

by

Jonathan M. Bobbitt

A dissertation submitted to the graduate faculty

in partial fulfillment of the requirements for the degree of

DOCTOR OF PHILOSOPHY

Major: Analytical Chemistry

Program of Study Committee:
Emily A. Smith, Major Professor
Robert S. Houk
Young Jin Lee
Jacob Petrich
Javier Vela

Iowa State University

Ames, Iowa

2017

Copyright © Jonathan M. Bobbitt, 2017. All rights reserved.

المنارة للاستشارات

www.manaraa.com

DEDICATION

Dedicated to my family: past, present, and future

المنارة للاستشارات

www.manaraa.com

TABLE OF CONTENTS

Page

DEDICATION ii

ACKNOWLEDGMENTS v

ABSTRACT vii

DISSERTATION OVERVIEW ix

CHAPTER 1 GENERAL INTRODUCTION 1

CHAPTER 2 FOURIER TRANSFORM-PLASMON WAVEGUIDE SPECTROSCOPY: A NON-DESTRUCTIVE MULTI-FREQUENCY METHOD FOR SIMULTANEOUSLY DETERMINING POLYMER THICKNESS AND APPARENT INDEX OF REFRACTION 23

Abstract 24
Introduction 24
Materials and Methods 27
Results and Discussion 30
Conclusions 38
Acknowledgements 38
References 39
Supporting Information 42

CHAPTER 3 SCANNING ANGLE RAMAN SPECTROSCOPY: A NONDESTRUCTIVE METHOD FOR SIMULTANEOUSLY DETERMINING MIXED POLYMER FRACTIONAL COMPOSITION AND FILM THICKNESS 44

Abstract 44
Introduction 45
Materials and Methods 49
Results and Discussion 52
Conclusions 63
Acknowledgements 64
References 64
Supporting Information 68

www.manaraa.com

CHAPTER 4 EXTRACTING INTERFACE LOCATIONS IN MULTILAYER POLYMER WAVEGUIDE FILMS USING SCANNING ANGLE RAMAN SPECTROSCOPY 71
Abstract 71
Introduction 72
Experimental 74
Results and Discussion 79
Conclusions 91
Acknowledgements 92
References 92
Supporting Information 96

CHAPTER 5 GENERAL CONCLUSIONS 100

APPENDIX A HIGH ANGULAR-RESOLUTION AUTOMATED VISIBLE-WAVELENGTH SCANNING ANGLE RAMAN MICROSCOPY 103

APPENDIX B QUANTITATIVE COMPARISON OF ORGANIC PHOTOVOLTAIC BULK HETEROJUNCTION PHOTOSTABILTY UNDER LASER ILLUMINATION 125

APPENDIX C CHARACTERIZING ELECTRIC FIELD EXPOSED P3HT THIN FILMS USING POLARIZED-LIGHT SPECTROSCOPIES 161

المنارة للاستشارات
www.manaraa.com

ACKNOWLEDGMENTS

The journey through graduate school is filled with many trials and tribulations, and successful navigation will leave one indebted to people for their help and constant encouragement. For this reason, I would like to take this time to thank these people for their contributions.

To Professor Emily A. Smith, I am thankful for the opportunity to be a member of her research group. Her guidance helped me developed into an independent scientific researcher. The lessons I learned from her will always be with me as I continue my journey through life. Also, I would like to thank my committee members for their guidance and support throughout the course of my graduate career.

In addition, I would like to thank the Smith group members I had the privilege of knowing: Matt, Mike, Neha, Dipak, Vy, Aleem, Danny, Qiaochu, Deyny, Charles, Chamari, Brett, Jingzhe, Sadie, Nicole, and Avinash. Thank you for all the wonderful memories, and it has been an honor working with all of you. I am especially thankful to Deyny for her contributions to the work presented in Chapter 3, and for her kindness and friendship over the years.

Lastly, I am thankful to my brothers, Justin and Chris, for their support and constant comedic relief. To my parents, Donald and Susan, words cannot express my gratitude for all your sacrifices through the years. You taught me to follow my dreams and to never give up. I want to thank you for all your love and support throughout my academic and athletic careers. You two will always be my number one fans. Finally, to my caring, loving, and supportive wife, Nour: my deepest gratitude. You are truly

للاستشارات المنارة
www.manaraa.com

wonderful person, and my greatest inspiration. Your love and encouragement over the years is much appreciated and noted. I look forward to our many adventures yet to come. Additional thanks to anyone that is due thanks, but is not mentioned above.

This research was supported by the U.S. Department of Energy, Office of Science, Basic Energy Sciences, Chemical Sciences, Geosciences, and Biosciences Division. The research was performed at the Ames Laboratory, which is operated for the U.S. DOE by Iowa State University under contract # DE-AC02-07CH11358. The document number assigned to this dissertation is IS-T 3213.

المنارة للاستشارات

www.manaraa.com

ABSTRACT

Non-destructive optical-based spectroscopic methods are needed for analyzing "real world" devices that consist of thin polymer waveguide films. Many applications (*e.g.,* sensors, microelectronics, optics, and biomedical applications, etc.) utilize thin polymer waveguide films, and non-destructive characterization methods based on Fourier transform (FT)-plasmon waveguide spectroscopy (PWR) and scanning angle (SA) Raman spectroscopy are used to extract optical, physical, and chemical properties simultaneously.

The FT-PWR method measures reflected light at polymer waveguide interface as both the incident frequency (wavelength) and incident angle are scanned. This method uses p- and s-polarized light to simultaneously extract the polymer waveguide thickness and apparent anisotropic indices of refraction. Polystyrene waveguide films ranging from 360 to 800 nm are used to demonstrate the method and it has an average 0.4% relative error when compared to profilometry and atomic force microscopy measurements.

SA Raman spectroscopy is used to measure mixed waveguide polymer films consisting of polystyrene-block-poly(methyl methacrylate) and homopolymer poly(methyl methacrylate) (PS-b-PMMA:PMMA), and poly(2-vinylnapthalene)-block-poly(methyl methacrylate) (P2VN-b-PMMA). PMMA homopolymer is added to the PS-b-PMMA solutions to vary the chemical composition. The chemical composition of each mixed film is quantified (SA Raman peak amplitude ratios) and averaged over all incident angles and is termed the Raman amplitude ratio (r_{ps}). This parameter is used to calculate the refractive index of each mixed waveguide polymer film. The refractive

المنارة للاستشارات

www.manaraa.com

index is an input parameter for sum square electric field (SSEF) calculations, which are used to model SA Raman spectra as a function of incident angle to extract the film thickness. The mixed polymer waveguide film thicknesses ranged from 495 to 971 nm, and the SA Raman spectroscopy method has an average 5% difference between the values determined by profilometry.

The SA Raman spectroscopy method developed for mixed polymer waveguide films is used to measure the chemical composition and extract interface locations in bilayer and trilayer films consisting of PMMA/PS or PMMA/PS/PMMA, respectively. The r_{ps} value is averaged over angle ranges corresponding to waveguide mode 0 and waveguide mode 1 for the bilayer and trilayer films, respectively. Six multilayer films are analyzed and their total thicknesses range from 330 to 1260 nm. Iterative SSEF calculations are used to model the SA Raman spectra as a function of incident angle, and the best fit to the experimental data is used to extract the total thickness and interface location(s). The method has an axial spatial resolution of 7 to 80 nm and provides comparable values to films measured by profilometry with an average 8% and 7% difference for the bilayer and trilayer films, respectively.

المنارة للاستشارات

www.manaraa.com

DISSERTAION OVERVIEW

This dissertation is organized into 5 chapters and 3 appendixes. A brief introduction to thin polymer films and the available destructive and nondestructive techniques used to characterize them, as well as a brief introduction of the theory and instrumentation of the optical-based techniques included in this dissertation are discussed in Chapter 1. Presented within Chapter 2 is a multi-frequency plasmon waveguide resonance method capable of simultaneously determining the anisotropic indices of refraction and thicknesses of thin polystyrene waveguide films on a 50-nm gold substrate. Discussed within Chapter 3 is a scanning angle Raman spectroscopy method for simultaneously determining the chemical composition, refractive index, and thickness of mixed polystyrene-block-poly(methyl methacrylate):poly(methyl methacrylate) waveguide films with varying compositions. In Chapter 4, the above method is modified and used along with iterative electric field intensity calculations to measure the chemical composition and extract the location of buried interfaces for bilayer poly(methyl methacrylate)/polystyrene and multilayer poly(methyl methacrylate)/polystyrene/poly(methyl methacrylate) thin waveguide films with 7–80-nm axial spatial resolution. General conclusions and potential future directions for the methods presented are summarized in Chapter 5. The work described in Appendix A is the development of an automated visible-wavelength scanning angle Raman microscope. The angular spread and uncertainty are determined by measuring the reflectivity of various salt solutions. Scanning angle Raman spectra of a thin copolymer film and a polystyrene waveguide film are used to show the benefits of a visible excitation source.

المنارة للاستشارات

www.manaraa.com

In Appendix B, the photostability of three polymers used in bulk heterojunction devices under visible laser illumination is measured, demonstrating power densities suitable for producing reliable Raman spectroscopy measurements of the polymer order in these devices. Finally, in Appendix C fluorescence anisotropy and polarized Raman spectroscopy measurements are used to study poly(3-hexylthiophene) films prepared in the presence of an external electric field. By varying the polarization angle, one can elucidate the preferential orientation of the polymer chain within the thin films.

المنارة للاستشارات

www.manaraa.com

CHAPTER 1

GENERAL INTRODUCTION

Introduction to Thin Polymer Films

Polymers are synthetic or natural macromolecules consisting of repeating monomer subunits with an extensive range of properties making them indispensable for everyday use in a variety of consumer-based applications.[1] Research into consumer applications (*e.g.,* coatings, rubbers, and plastics, etc.) created a foundation for polymer science and generated a need to develop tools for analyzing new products.[2] Due to the versatile properties of polymers, a great deal of research focuses on measuring and characterizing polymer mechanical properties,[3-8] optical properties.[9-14] and chemical content and morphology.[15-20] A deeper understanding of polymer properties has enabled thin polymer films to be used in a number of important applications spanning from consumer products, to medical devices, to energy capture and communication equipment.

In the past 20 years thin polymer film research has increased significantly. Within this thesis, thin polymer films refer to those with a thickness in the range from a monolayer to several microns in thickness. Many important applications utilize thin polymer films, including energy capture and conversion devices,[21,22] thin polymer waveguides (*e.g.,* optical fibers and sensors),[23,24] coatings and optics,[25-28] packaging,[29-31] and biomedical applications.[32,33] Thin polymer film fabrication is crucial to the above applications, and an entire field of study is dedicated to the art and science of thin

المنارة للاستشارات
www.manaraa.com

polymer film preparation. Solution-based fabrication methods are easy to implement and desirable due to their low production cost. Several recent review articles provide excellent detail about the different solution-based methods for thin polymer film preparation, but in short the most common techniques are dip coating,[34] drop coating,[35,36] and spin coating.[37,38] Among these methods, spin coating is used extensively due to its ability to uniformly cover large substrates with reproducible film thicknesses. Optical and physical properties (*e.g.,* refractive index and thickness) are important for modeling and developing new thin polymer films during and after the fabrication process. New characterization techniques and methods help drive the development of thin polymer films, and these can be classified into two categories: destructive and nondestructive techniques.

Electron microscopy, secondary ion mass spectrometry (SIMS), and scanning probe microscopy (*e.g.,* atomic force microscopy (AFM) and profilometry) are destructive techniques that provide information on a thin polymer film's local structure and thickness. Scanning electron microscopy (SEM) and transmission electron microscopy (TEM) are high spatial resolution imaging techniques, and when combined with heavy metal staining provide structural images on thin polymer films.[39-42] SEM is used to provide structural information from the surface of the thin polymer film, while TEM requires the film to be removed from the substrate and then sectioned into thin layers. The thin sections are used to provide information on the internal structure, as well as to measure the thickness of the films. SIMS operated in depth profiling mode is a powerful technique that also provides chemical content information on the internal thin polymer film structure as well as the thickness.[43,44] AFM and profilometry are other

المنارة للاستشارات
www.manaraa.com

methods for measuring thin polymer film thickness;[45] however, they require the probe to be in contact with the surface and for the film to be scratched in order to measure the thickness. All the above techniques provide high resolution information, but are sample destructive and are generally not suitable for *in situ* thin polymer film characterization.

There is an increasing demand for optical-based nondestructive *in situ* spectroscopies capable of providing refractive index, thickness, and chemical content information, but there are few characterization techniques that provide all the above information simultaneously. Surface plasmon resonance (SPR) and ellipsometry are two optical-base spectroscopies that measure changes in the reflected light intensity or changes in the elliptical polarization of the light, respectively. SPR requires a metal film, capable of generating a surface plasmon,[46] which is susceptible to changes in the adjacent layer's refractive index or thickness.[11,47] Due to the inherent limitation of the technique only refractive index or thickness is measured in a traditional SPR experiment, but there are advanced SPR-based techniques that work around this limitation.[45,48,49] On the other hand, ellipsometry is capable of simultaneously providing a thin polymer film's refractive index and thickness.[50-52] In an ellipsometry measurement the change in polarization and the phase difference are measured independently, and both are modeled to extract the refractive index and thickness.[53] SPR and ellipsometry are nondestructive techniques, but they do not provide chemical content information, a significant limitation when the film composition is not known.

Vibrational spectroscopy (*e.g.*, Infrared (IR) and Raman spectroscopy) are well suited for measuring the chemical content information from thin polymer films. A combined ellipsometry and IR technique (IR-variable angle spectroscopic ellipsometry)

المنارة للاستشارات
www.manaraa.com

termed IR-VASE has the benefits of both techniques. It can provide chemical content, refractive index, and thickness information, but it takes 8 to 12 hours for a single thin film measurement.[54] Similarly, attenuated total reflection (ATR)-IR is capable of simultaneously providing chemical content from various depths within the film.[55-58] ATR-IR thickness analysis is problematic due to the variation in the evanescent wave penetration depths across the spectrum. Therefore, techniques based on Raman spectroscopy are needed since they require little to no sample preparation, provide fast acquisition times, and utilize a monochromatic source that will have a single penetration depth in an ATR-based format. The remaining chapters in the dissertation describe optical-based techniques that employ SPR and Raman spectroscopy. The techniques simultaneously provide chemical content, refractive index, and thickness for thin polymer waveguide films.

Thin Polymer Waveguide Films

Thin polymer films will act as waveguides when their thickness is greater than $\frac{\lambda}{2\eta}$, where λ is the excitation wavelength and η is the refractive index of the polymer film. Thin polymer waveguides are finding extensive use in the telecom and Datacom industry due to their low cost and ability to be mass produced, when compared to traditional glass-based fiber optics that are fragile and expensive.[59] Other polymer waveguide applications include biological[60,61] and environmental[62,63] sensors, as well as non-plasmonic devices for Raman scattering enhancement (*e.g.,* waveguide Raman spectroscopy).[64,65]

The theory underlying optical waveguides, both irradiative and leaky, has been presented in several papers.[66-68] Briefly, when incident light traverses a high refractive

المنارة للاستشارات

www.manaraa.com

index prism (η_1, prism refractive index) it can be coupled into the adjacent polymer layer (η_2, polymer refractive index). If $\eta_1 > \eta_2$ then the incident light can be optically confined within the polymer film, and with sufficient polymer thickness (as stated above) the waveguide modes are localized and propagate in the polymer film.[68] The guided light will "leak" (decay exponentially) from the polymer interface into the adjacent layer when $\eta_2 > \eta_3$ (refractive index of air or an analyte layer)and can be used to generate Raman scattering (waveguide Raman spectroscopy) in the layer adjacent to the thin polymer waveguide. Similarly, when the incident angle matches the waveguide mode maximum angle, constructive interference occurs generating an enhancement in the Raman scattering originating from the polymer waveguide. Both phenomena can be modeled with electric field intensity calculations to extract information on refractive index and thickness of the thin polymer waveguide film, and this is the central theme behind the methods discussed in Chapters 2-4.

Surface Plasmon Resonance

SPR is an optical spectroscopic technique that measures the intensity of reflected light from a noble metal at an interface with suitable indices of refraction. Within the noble metal film (*e.g.,* gold or silver) are non-radiative electromagnetic surface waves (surface plasmon polaritons) that propagate parallel to the metal/air or analyte layer. These oscillating waves are sensitive to changes in the adjacent layer's refractive index or thickness, which makes SPR a useful analytical tool for measuring the adsorption of molecules. In a traditional SPR experiment the reflected light from a monochromatic source is measured from a prism/noble metal film interface. There are two main prism

المنارة للاستشارات

www.manaraa.com

coupling options proposed by Otto and Kretschmann, and these are illustrated in Figure 1A and B.

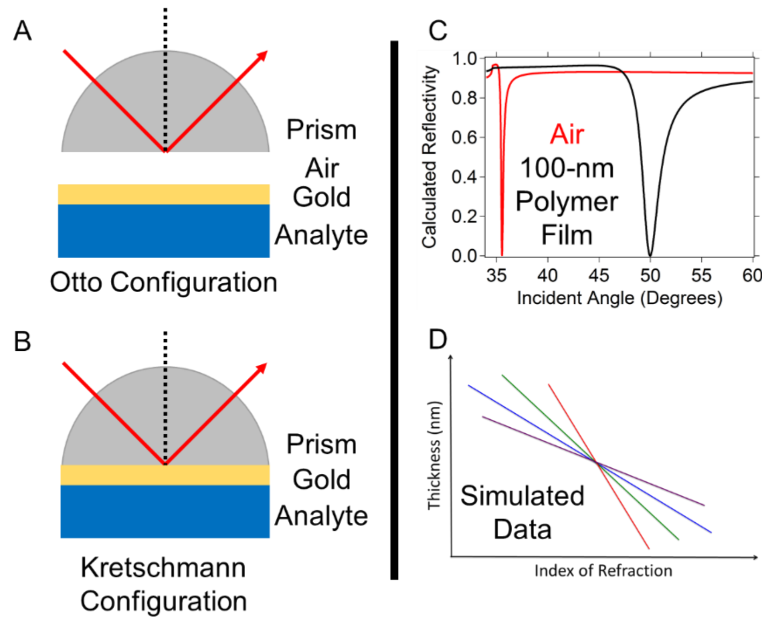

Figure 1: The different prism coupling configurations are shown with (A) being the Otto and (B) being the Kretschmann configuration. (C) A calculated SPR reflectivity curve for sapphire prism/50-nm gold film/air (red curve) and a sapphire prism/50-nm gold film/100-nm polymer film (black curve). The SPR curve shifts to higher angles and the width increases with the addition of a 100-nm polymer film. Fitting the black curve using Fresnel equations will not allow the refractive index and thickness of the polymer film to be determined simultaneously. (D) A simulated graph of thickness as a function of refractive index curves with the colors representing different frequencies. The intersection point is used to simultaneously determine the index of refraction and thickness from a multi-frequency SPR measurement.

www.manaraa.com

For the Otto coupling configuration the air layer needs to be no greater than 200 nm away from the prism.[69] Due to the technical challenge of the Otto configuration, the Kretschmann configuration is used more frequently. Under conditions of total internal reflection, the reflected light is attenuated and a dip in the reflectivity curve is observed when the incident angle is scanned across an appropriate range. A calculated SPR reflectivity curve (modeled using Fresnel calculations)[70] is shown in Figure 1B using a 785-nm excitation source, a 50-nm gold film, and a bulk air layer. A shift in the SPR reflectivity curve is observed when a 100-nm polymer film is adsorbed to the gold film's surface. This shift is represented by equation 1, where k is the plasmon wave vector, η is the refractive index of the analyte (*e.g.,* polymer film), and d is the thickness of the analyte layer. The variables k and η depend on the excitation wavelength. A full detailed derivation and theoretical description of SPR can be found elsewhere.[71]

$$\boldsymbol{k(\lambda) = \eta(\lambda) \times d} \quad (\mathbf{1})$$

For a single excitation source experiment, only the refractive index or the thickness of the analyte can be determined as observed from equation 1. As mentioned above, SPR-based techniques exist that allow for both parameters to be determined by solving the continuum solution to equation 1 at two different wavelengths.[48] Figure 1C is a graphical representation of a multi-frequency method (*i.e.,* multi-wavelength) with each colored line representing a different frequency. The intersection point will provide the refractive index and thickness from a single measurement.

www.manaraa.com

Spontaneous Raman Spectroscopy and Instrumentation

When light is scattered by molecules a small fraction of the photons will have a shift in the wavelength, this is known as the *Raman effect*.[72] Krishnan and Raman first reported this inelastic scattering process in 1928; this work was the basis for Raman's 1930 Nobel Prize in physics. Early work in Raman spectroscopy was limited due to technical challenges (*i.e.*, low flux sources, inefficient light collection and detection)[73], but had a surge of popularity starting in the late 1980s with the rise of laser sources and modern computing technology. Since then, over 97,000 journal articles containing Raman spectroscopy have been written and it is now a standard instrument found in most analytical instrumentation labs. Several sources exist that provide a detailed description of the classical and quantum mechanical description of Raman spectroscopy and the most common applications.[73-81] A complete description can be found in this literature, but a brief introduction to the theory of Raman spectroscopy is provided to emphasize the differences between Raman spectroscopy and other vibrational spectroscopies (*e.g.,* infrared (IR) spectroscopy).

The scattered light from a molecule irradiated with monochromatic light will result in the elastic ($Energy = h\nu_0$) and inelastic ($Energy = h\nu_0 \pm h\nu_1$) scattering of photons where h is Planck's constant, ν_0 is the monochromatic light frequency, and ν_1 is the frequency of the scattered photons. The basic classical description of Raman scattering shows that an oscillating electric field induces polarization within a molecule that will radiate scattered light with no net change (Rayleigh scattering), or with either a gain or loss (anti-stokes and stokes scattering) in energy equivalent to vibrational modes within the molecule. Figure 2A shows the energy diagram for Rayleigh and Raman

المنارة للاستشارات
www.manaraa.com

scattering spectroscopic transitions. It should be noted that the "virtual states" are not true quantum states, but can be considered short lived distortions of the electron cloud caused by the incident light.[73] Anti-stokes scattering, shown in Figure 2A, gains energy ($h\nu_0 + h\nu_1$); however, it originates from a higher vibrational level within the electronic ground state. At room temperature, the population of the excited state is significantly lower than the ground state, as described by the Boltzmann distribution, therefore anti-stokes is a less intense scattering process. Equation 2 below shows that the induced polarization within the molecule (P) scales with the polarizability (α) and the incident electric field (E).

$$\boldsymbol{P} = \boldsymbol{\alpha} \times \boldsymbol{E} \quad (\mathbf{2})$$

From this classical equation two important insights into Raman scattering are obtained. First, Raman and Rayleigh intensities are linear with the incident electric field and thus enhanced signal is realized when using more intense sources (*i.e.,* laser). Second, only vibrations that cause a change in the polarizability of a molecule ($\alpha \neq 0$) will yield Raman bands.

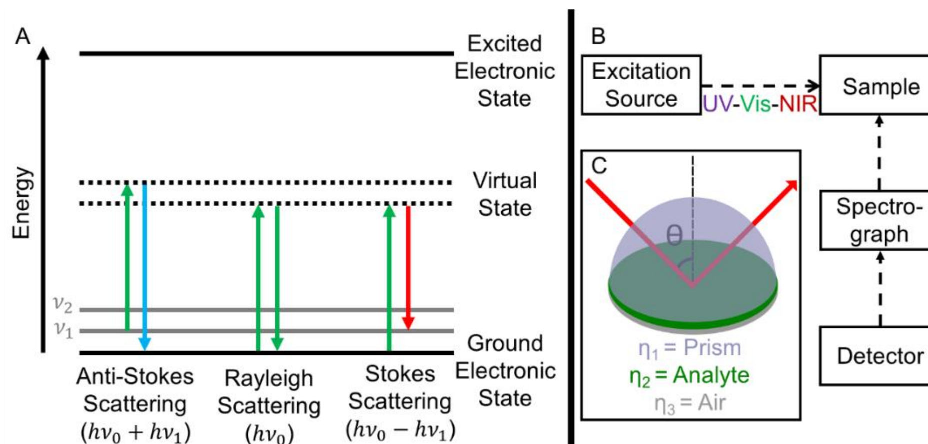

www.manaraa.com

Figure 2: (A) Shows the energy diagram for the spectroscopic transitions associated with Rayleigh (elastic) and Raman scattering (inelastic). Raman scattering consists of anti-stokes and stokes scattering that is shifted in energy by $h\nu_0 \pm h\nu_1$. (B) Depicts a box diagram of a dispersive Raman spectrometer operated in a 90° collection angle. Raman spectroscopy can be used with a variety of lasers ranging from ultraviolet (UV), visible (Vis), and near-infrared (NIR) light. (C) A scanning angle Raman spectroscopy sample schematic depicting the incident light passing through a high refractive index prism onto an analyte of interest. The incident light is scanned over a range of angles (θ) and angle dependent spectra are collected.

Two fundamental differences between Raman and IR spectroscopy govern when to use the two complementary techniques. The first difference between the two vibrational spectroscopies deals with the vibrational modes probed by each technique. Symmetric bond vibrational modes have greater changes in the polarizability, effectively making them strong Raman scattering bonds. Inversely, IR spectroscopy requires a change in the dipole for a given bond vibration to be IR active, so asymmetric bonds are strong IR absorbers. The second difference is the probability of each event occurring. IR is an absorption technique, and the molar absorptivity is a measure of the probability of the transition occurring. The Raman cross section (analogous to molar absorptivity) is proportional to the probability of an incident photon being scattered as a Raman-shifted photon with a given change in wavelength.[73] Raman cross sections of typical functional groups are 10 orders of magnitude smaller than IR molar absorptivity, which makes IR absorption a more probable phenomenon.[82] Despite lower signals, advances in Raman

المنارة للاستشارات
www.manaraa.com

instrumentation as well as emerging research and industrial applications have made it a quantitative and qualitative technique that is complementary to IR spectroscopy.

A dispersive Raman spectrometer consists of several elements which are shown as a box diagram in Figure 2B. A typical dispersive instrument will include a monochromatic excitation source (*e.g.,* laser) featuring wavelengths ranging from the UV to the NIR. A 90° collection angle is a common setup, which avoids direct exposure of the excitation source on the detector. After the sample, a spectrograph (*e.g.,* monochromator or spectrometer) is used to disperse the inelastic scattered photons onto the detector. Many modern dispersive Raman spectrometers use multichannel detectors, such as charge-coupled devices (CCD), since multiwavelength detection is advantageous due to an increase in signal-to-noise ratios and faster acquisition times.[73] For photon counting detectors (*i.e.,* CCD detectors) equation 2 can be rewritten in the form of equation 3 below, which is more consistent with a quantum mechanical approach to Raman spectroscopy. The variable P_R is the collected Raman scattered photons per second, P_0 is the incident photons per second, σ_1 is the Raman cross section (centimeters to the sixth power per molecule), $\bar{\nu}_0$ is the incident frequency (in wavenumbers), $\bar{\nu}_0 - \bar{\nu}_1$ is the frequency of the Raman shift (in wavenumbers), D is the number density of scatters (molecules per cubic centimeter), and dz the laser path length in the sample (centimeters).

$$\mathbf{P_R = P_0 \sigma_1 \bar{\nu}_0 (\bar{\nu}_0 - \bar{\nu}_1)^3 Ddz} \quad \mathbf{(3)}$$

Equation 3 shows the frequency dependence ($\bar{\nu}_0(\bar{\nu}_0 - \bar{\nu}_1)^3$) of the Raman scattering, and gives insights into what excitation source to use. Shorter wavelengths will

المنارة للاستشارات
www.manaraa.com

generate more Raman scattering, while longer wavelengths will generate less. It is important to note that the type of samples being analyzed will also guide the choice of the excitation source. Highly fluorescent samples are problematic with UV and Vis excitation, but auto luminescence can be avoided with longer wavelength excitation sources

Scanning Angle Raman Spectroscopy and Instrumentation

A diagram of a sample configuration for a typical scanning angle (SA) Raman experiment is shown in Figure 2C. It consists of a high refractive index prism (η_1) optically coupled to the analyte layer (*e.g.,* thin polymer film, η_2) with $\eta_1 > \eta_2$. Under these conditions there are three angle ranges of interest, given in a, b and c below, where θ_i and θ_c are the incident and critical angle, respectively.

$$a)\ \theta_i < \theta_c$$

$$b)\ \theta_i = \theta_c$$

$$c)\ \theta_i > \theta_c$$

The critical angle is defined by Snell's law (equation 4), at angles at or above the critical angle the incident light will be under the condition of total internal reflection (TIR) inside the prism.

$$\boldsymbol{\theta_c = \sin^{-1}\left(\frac{\eta_2}{\eta_1}\right)} \quad (4)$$

No light is transmitted through the prism (η_1)/analyte (η_2) interface, but an evanescent wave is generated that decays exponentially into the analyte layer. Ikeshoji *et. al.* demonstrated TIR Raman spectroscopy as a surface sensitive technique as well as the

المنارة للاستشارات
www.manaraa.com

capability to control the penetration depth of the evanescent field.[83] When collecting Raman spectra at angles greater than the critical angle, the depth over which Raman scattering is generated (D_{RS}) is modeled by equation 5. Equation 5 is a function of the wavelength (λ), the incident angle (θ_i), and prism/analyte indices of refraction ($\eta_1$and η_2). Using the angle ranges $\theta_i = \theta_c$ and $\theta_i > \theta_c$ makes TIR Raman spectroscopy more versatile as a surface sensitive technique with depth profiling capabilities (although the latter has not been experimentally demonstrated).

$$\boldsymbol{D_{RS} = \frac{\lambda}{4\pi}\left[\left(\eta_1^2 \sin^2 \theta_i\right) - \eta_2^2\right]^{-\frac{1}{2}}} \quad (5)$$

In addition to its use in measuring polymers, TIR Raman spectroscopy has been used to follow absorption kinetics,[84-87] and characterize interfaces[87-91] and surfaces.[92-94] The theory of Raman scattering generated with evanescent wave excitation has been shown for an array of excitation and collection geometries by D'Hooge *et. al.*, and the reader can look to these articles for a more detailed description.[95,96] SA Raman spectroscopy encompasses the three angle ranges stated above (a, b, and c). SA Raman spectroscopy is no longer a surface sensitive technique when spectra are collected below the critical angle ($\theta_i < \theta_c$); however, it is useful for characterizing thin polymer waveguide films.

A home-built scanning angle Raman microscope (used to collect the data presented in Chapter 4 and Appendices A and B) is shown in Figure 3. It consists of all the parts described in detail above; however, the excitation source is coupled into the microscope for epi-illumination or into an optical fiber for scanning angle Raman illumination. A microscope allows the collection of an optical image by focusing the

المنارة للاستشارات
www.manaraa.com

observation region onto local structures or features present in samples. For scanning angle Raman instrumentation, there are variations on directing the excitation source to a prism. Two common ways use either a translational stage and a mirror on a galvanometer stage,[97] or the excitation source can be coupled to a fiber optic which is mounted on a rotational stage (as shown in Figure 3B).[98]

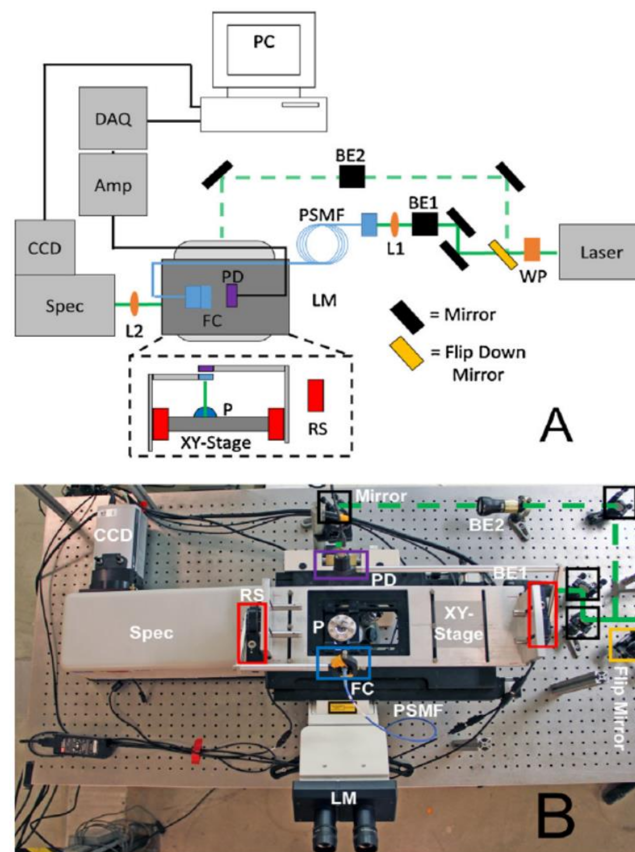

Figure 3: (A) Instrument schematic for a 532-nm SA Raman microscope: half waveplate (WP), beam expanders (BE1, BE2), Leica microscope (LM), aspheric focusing lens (L1), polarization-maintaining single-mode fiber optic (PSMF), fiber collimator (FC), high index of refraction prism (P), photo-diode (PD), rotational stages (RS), amplifier (Amp), data acquisition device (DAQ), computer (PC), collection lens (L2), spectrometer (Spec),

المنارة للاستشارات
www.manaraa.com

and charge-coupled device (CCD). The dashed view is perpendicular to the optical table. (B) Picture of 532-nm SA Raman microscope. The laser is not shown. Selected items are highlighted in the picture with color coded boxes to match the schematic. Reprinted from Analytica Chimica Acta, 848, Michael D. Lesoine *et. al.*, High angular-resolution automated visible-wavelength scanning angle Raman microscopy, 61-66, Copyright (2014), with permission from Elsevier.

References

(1) McCrum, N. G.; Buckley, C.; Bucknall, C. B. *Principles of polymer engineering*; Oxford University Press, USA, 1997.

(2) Furukawa, Y. *Inventing polymer science: Staudinger, Carothers, and the emergence of macromolecular chemistry*; Chemical Heritage Foundation, 1998.

(3) Crissman, J. M.; Sauer, J. A.; Woodward, A. E. *J. Polym. Sci.* **1964**, *2*, 5075-5091.

(4) Zhu, K. J.; Hendren, R. W.; Jensen, K.; Pitt, C. G. *Macromolecules* **1991**, *24*, 1736-1740.

(5) Bockhorn, H.; Hornung, A.; Hornung, U. *J. Anal. Appl. Pyrolysis* **1999**, *50*, 77-101.

(6) Bryant, Z.; Stone, M. D.; Gore, J.; Smith, S. B.; Cozzarelli, N. R.; Bustamante, C. *Nature (London, U. K.)* **2003**, *424*, 338-341.

(7) Cheng, X.; Canavan, H. E.; Stein, M. J.; Hull, J. R.; Kweskin, S. J.; Wagner, M. S.; Somorjai, G. A.; Castner, D. G.; Ratner, B. D. *Langmuir* **2005**, *21*, 7833-7841.

(8) Zhao, J.; Morgan, A. B.; Harris, J. D. *Polymer* **2005**, *46*, 8641-8660.

(9) Osaheni, J. A.; Jenekhe, S. A. *Chem. Mater.* **1995**, *7*, 672-682.

المنارة للاستشارات
www.manaraa.com

(10) Samoc, M.; Samoc, A.; Luther-Davies, B.; Bao, Z.; Yu, L.; Hsieh, B.; Scherf, U. *J. Opt. Soc. Am. B* **1998**, *15*, 817-825.

(11) Baba, A.; Park, M.-K.; Advincula, R. C.; Knoll, W. *Langmuir* **2002**, *18*, 4648-4652.

(12) Ravirajan, P.; Haque, S. A.; Durrant, J. R.; Bradley, D. D. C.; Nelson, J. *Adv. Funct. Mater.* **2005**, *15*, 609-618.

(13) Brown, S. J.; Schlitz, R. A.; Chabinyc, M. L.; Schuller, J. A. *Phys. Rev. B* **2016**, *94*, 165105/165101-165105/165108.

(14) Laumer, T.; Stichel, T.; Nagulin, K.; Schmidt, M. *Polym. Test.* **2016**, *56*, 207-213.

(15) Keijzers, A. E. M.; Van Aartsen, J. J.; Prins, W. *J. Amer. Chem. Soc.* **1968**, *90*, 3107-3113.

(16) Kline, R. J.; McGehee, M. D.; Kadnikova, E. N.; Liu, J.; Frechet, J. M. J.; Toney, M. F. *Macromolecules* **2005**, *38*, 3312-3319.

(17) Coffey, D. C.; Ginger, D. S. *Nat. Mater.* **2006**, *5*, 735-740.

(18) Kang, H.; Uddin, M. A.; Lee, C.; Kim, K.-H.; Nguyen, T. L.; Lee, W.; Li, Y.; Wang, C.; Woo, H. Y.; Kim, B. J. *J. Am. Chem. Soc.* **2015**, *137*, 2359-2365.

(19) Jovanov, V.; Yumnam, N.; Mueller, A.; Gruber, M.; Wagner, V. *J. Phys. Chem. C* **2017**, Ahead of Print.

(20) Root, S. E.; Alkhadra, M. A.; Rodriquez, D.; Printz, A. D.; Lipomi, D. J. *Chem. Mater.* **2017**, *29*, 2646-2654.

(21) Facchetti, A. *Chem. Mater.* **2011**, *23*, 733-758.

(22) Wang, Q.; Xie, Y.; Soltani-Kordshuli, F.; Eslamian, M. *Renewable Sustainable Energy Rev.* **2016**, *56*, 347-361.

المنارة للاستشارات
www.manaraa.com

(23) Frolov, S. V.; Shkunov, M.; Fujii, A.; Yoshino, K.; Vardeny, Z. V. *IEEE J. Quantum Electron.* **2000**, *36*, 2-11.

(24) Chiang, K. S. *Proc. SPIE* **2010**, *7605*, 760507/760501-760507/760518.

(25) Chen, C.-T.; Tsai, T.-W. *Sensors and Actuators A: Physical* **2016**, *244*, 252-260.

(26) Komikado, T.; Inoue, A.; Masuda, K.; Ando, T.; Umegaki, S. *Thin Solid Films* **2007**, *515*, 3887-3892.

(27) Lee, H.; Alcaraz, M. L.; Rubner, M. F.; Cohen, R. E. *ACS Nano* **2013**, *7*, 2172-2185.

(28) Wu, Z.; Walish, J.; Nolte, A.; Zhai, L.; Cohen, R. E.; Rubner, M. F. *Advanced Materials* **2006**, *18*, 2699-2702.

(29) Alix, S.; Mahieu, A.; Terrie, C.; Soulestin, J.; Gerault, E.; Feuilloley, M. G. J.; Gattin, R.; Edon, V.; Ait-Younes, T.; Leblanc, N. *European Polymer Journal* **2013**, *49*, 1234-1242.

(30) Canellas, E.; Aznar, M.; Nerin, C.; Mercea, P. *Journal of Materials Chemistry* **2010**, *20*, 5100-5109.

(31) Siracusa, V.; Ingrao, C.; Lo Giudice, A.; Mbohwa, C.; Dalla Rosa, M. *Food Research International* **2014**, *62*, 151-161.

(32) Krishnan, S.; Weinman, C. J.; Ober, C. K. *J. Mater. Chem.* **2008**, *18*, 3405-3413.

(33) Such, G. K.; Johnston, A. P. R.; Caruso, F. *Chemical Society Reviews* **2011**, *40*, 19-29.

(34) Boysen, R. I.; Schwarz, L. J.; Nicolau, D. V.; Hearn, M. T. W. *J. Sep. Sci.* **2017**, *40*, 314-335.

(35) Ghosh, K.; Balog, E. R. M.; Kahn, J. L.; Shepherd, D. P.; Martinez, J. S.; Rocha, R. C. *Macromol. Chem. Phys.* **2015**, *216*, 1856-1861.

المنارة للاستشارات

www.manaraa.com

(36) Chaudhari, S. R.; Griffin, J. M.; Broch, K.; Lesage, A.; Lemaur, V.; Dudenko, D.; Olivier, Y.; Sirringhaus, H.; Emsley, L.; Grey, C. P. *Chem. Sci.* **2017**, *8*, 3126-3136.

(37) Norrman, K.; Ghanbari-Siahkali, A.; Larsen, N. B. *Annu. Rep. Prog. Chem., Sect. C: Phys. Chem.* **2005**, *101*, 174-201.

(38) Rodriguez, D. N.; John Wiley & Sons, Inc., 2013, pp 473-491.

(39) Lindqvist, C.; Sanz-Velasco, A.; Wang, E.; Bäcke, O.; Gustafsson, S.; Olsson, E.; Andersson, M. R.; Müller, C. *Journal of Materials Chemistry A* **2013**, *1*, 7174-7180.

(40) Cha, K. J.; Lih, E.; Choi, J.; Joung, Y. K.; Ahn, D. J.; Han, D. K. *Macromolecular bioscience* **2014**, *14*, 667-678.

(41) Rohini, R.; Bose, S. *ACS applied materials & interfaces* **2014**, *6*, 11302-11310.

(42) Zhong, Y.; Suzuki, K.; Inoue, D.; Hashizume, D.; Izawa, S.; Hashimoto, K.; Koganezawa, T.; Tajima, K. *Journal of Materials Chemistry A* **2016**, *4*, 3335-3341.

(43) Lee, Y.; Lee, J.; Lim, W. C.; Shin, K.; Kim, K.-J. *Surface and Interface Analysis* **2011**, *43*, 277-280.

(44) Lee, J.; Kang, M. H.; Lim, W. C.; Shin, K.; Lee, Y. *Surface and Interface Analysis* **2013**, *45*, 498-502.

(45) Bobbitt, J. M.; Weibel, S. C.; Elshobaki, M.; Chaudhary, S.; Smith, E. A. *Anal. Chem. (Washington, DC, U. S.)* **2014**, *86*, 11957-11961.

(46) Raether, H. *Surface Science* **1983**, *125*, 624-634.

(47) Ji, L.; Sun, X.; He, G.; Liu, Y.; Wang, X.; Yi, Y.; Chen, C.; Wang, F.; Zhang, D. *Sens. Actuators, B* **2017**, *244*, 373-379.

(48) Peterlinz, K. A.; Georgiadis, R. *Optics Communications* **1996**, *130*, 260-266.

المنارة للاستشارات

www.manaraa.com

(49) Granqvist, N.; Liang, H.; Laurila, T.; Sadowski, J.; Yliperttula, M.; Viitala, T. *Langmuir* **2013**, *29*, 8561-8571.

(50) Hilfiker, J. N.; Synowicki, R. A.; Bungay, C. L.; Carpio, R. *Solid State Technol.* **1998**, *41*, 101-102, 104, 106, 108, 110.

(51) Campoy-Quiles, M.; Heliotis, G.; Xia, R.; Ariu, M.; Pintani, M.; Etchegoin, P.; Bradley, D. D. C. *Adv. Funct. Mater.* **2005**, *15*, 925-933.

(52) Huang, Y.; Paul, D. R. *Macromolecules* **2006**, *39*, 1554-1559.

(53) Polgár, O.; Petrik, P.; Lohner, T.; Fried, M. *Applied Surface Science* **2006**, *253*, 57-64.

(54) Kang, S.; Prabhu, V. M.; Soles, C. L.; Lin, E. K.; Wu, W.-l. *Macromolecules* **2009**, *42*, 5296-5302.

(55) Chan, K. L. A.; Kazarian, S. G. *Applied Spectroscopy* **2003**, *57*, 381-389.

(56) Yang, P.; Meng, X.; Zhang, Z.; Jing, B.; Yuan, J.; Yang, W. *Analytical chemistry* **2005**, *77*, 1068-1074.

(57) Nikonenko, N.; Tretinnikov, O. *Journal of Applied Spectroscopy* **2008**, *75*, 878-882.

(58) Tran, W.; Tisinger, L. G.; Lavalle, L. E.; Sommer, A. J. *Applied Spectroscopy* **2015**, *69*, 230-238.

(59) Eldada, L.; Shacklette, L. W. *IEEE J. Sel. Top. Quantum Electron.* **2000**, *6*, 54-68.

(60) Gizeli, E. *Smart Mater. Struct.* **1997**, *6*, 700-706.

(61) Irawan, R.; Cheng, Y. H.; Ng, W. M.; Aung, M. M.; Lao, I. K.; Thaveeprungsriporn, V. *Biosens. Bioelectron.* **2011**, *26*, 3666-3669.

(62) Ren, Y.; Mormile, P.; Petti, L.; Cross, G. H. *Sens. Actuators, B* **2001**, *75*, 76-82.

المنارة للاستشارات
www.manaraa.com

(63) Cordero, S. R.; Low, A.; Ruiz, D.; Lieberman, R. A. *Proc. SPIE-Int. Soc. Opt. Eng.* **2007**, *6755*, 675503/675501-675503/675511.

(64) Kanger, J. S.; Otto, C.; Slotboom, M.; Greve, J. *J. Phys. Chem.* **1996**, *100*, 3288-3292.

(65) Hu, D.-B.; Qi, Z.-M. *J. Phys. Chem. C* **2013**, *117*, 16175-16181.

(66) Zimba, C.; Turrell, S.; Swalen, J.; Hallmark, V.; Rabolt, J. *Journal of Physical Chemistry* **1990**, *94*, 939-943.

(67) Syms, R. R.; Cozens, J. R. *Optical guided waves and devices*; McGraw-Hill, 1992.

(68) Khomchenko, A. V. e. *Waveguide spectroscopy of thin films*; Academic Press, 2005; Vol. 33.

(69) Otto, A. *Zeitschrift für Physik* **1968**, *216*, 398-410.

(70) Hansen, W. N. *Journal of The Optical Society of America.* **1968**, *58*, 380-390.

(71) Knoll, W. *Annual Review of Physical Chemistry* **1998**, *49*, 569-638.

(72) Raman, C. V.; Krishnan, K. *Nature* **1928**, *121*, 619.

(73) McCreery, R. L. *Raman spectroscopy for chemical analysis*; John Wiley & Sons, 2005; Vol. 225.

(74) Evans, J. C. *Advan. Anal. Chem. Instrum.* **1968**, *7*, 41-66.

(75) Li-Chan, E. C. Y. *Trends Food Sci. Technol.* **1996**, *7*, 361-370.

(76) Nafie, L. A. *Pract. Spectrosc.* **2001**, *28*, 1-10.

(77) Vankeirsbilck, T.; Vercauteren, A.; Baeyens, W.; Van der Weken, G.; Verpoort, F.; Vergote, G.; Remon, J. P. *TrAC, Trends Anal. Chem.* **2002**, *21*, 869-877.

(78) Tuma, R. *J. Raman Spectrosc.* **2005**, *36*, 307-319.

(79) Das, R. S.; Agrawal, Y. K. *Vib. Spectrosc.* **2011**, *57*, 163-176.

المنارة للاستشارات
www.manaraa.com

(80) Pence, I.; Mahadevan-Jansen, A. *Chem Soc Rev* **2016**, *45*, 1958-1979.

(81) Esmonde-White, K. A.; Cuellar, M.; Uerpmann, C.; Lenain, B.; Lewis, I. R. *Anal. Bioanal. Chem.* **2017**, *409*, 637-649.

(82) Sasic, S.; Ozaki, Y. *Raman, infrared, and near-infrared chemical imaging*; John Wiley & Sons, 2011.

(83) Ikeshoji, T.; Ono, Y.; Mizuno, T. *Applied optics* **1973**, *12*, 2236-2237.

(84) Beattie, D. A.; Larsson, M. L.; Holmgren, A. R. *Vib. Spectrosc.* **2006**, *41*, 198-204.

(85) Woods, D. A.; Petkov, J.; Bain, C. D. *Colloids Surf., A* **2011**, *391*, 10-18.

(86) Grenoble, Z.; Baldelli, S. *J. Phys. Chem. B* **2013**, *117*, 9882-9894.

(87) Liljeblad, J. F. D.; Furo, I.; Tyrode, E. C. *Phys Chem Chem Phys* **2016**, *19*, 305-317.

(88) Nickolov, Z. S.; Earnshaw, J. C.; McGarvey, J. J. *Colloids Surf., A* **1993**, *76*, 41-49.

(89) Fujiwara, K.; Watarai, H. *Langmuir* **2003**, *19*, 2658-2664.

(90) Jubb, A. M.; Verreault, D.; Posner, R.; Criscenti, L. J.; Katz, L. E.; Allen, H. C. *J. Colloid Interface Sci.* **2013**, *400*, 140-146.

(91) Liljeblad, J. F. D.; Furo, I.; Tyrode, E. C. *Phys. Chem. Chem. Phys.* **2017**, *19*, 305-317.

(92) Itoh, T.; Mutsukura, N. *Vacuum* **2004**, *77*, 11-18.

(93) Lee, C.; Wacklin, H.; Bain, C. D. *Soft Matter* **2009**, *5*, 568-575.

(94) Liu, C.; Thormann, E.; Claesson, P. M.; Tyrode, E. *Langmuir* **2014**, *30*, 8866-8877.

(95) D'Hooge, L.; Vigoureux, J. M. *Chemical Physics Letters* **1979**, *65*, 500-506.

(96) D'Hooge, L.; Vigoureux, J. M.; Menu, C. *The Journal of Chemical Physics* **1981**, *74*, 3639-3659.

المنارة للاستشارات

www.manaraa.com

(97) McKee, K. J.; Smith, E. A. *Rev. Sci. Instrum.* **2010**, *81*, 043106/043101-043106/043106.

(98) Lesoine, M. D.; Bobbitt, J. M.; Zhu, S.; Fang, N.; Smith, E. A. *Anal. Chim. Acta* **2014**, *848*, 61-66.

المنارة للاستشارات

www.manaraa.com

CHAPTER 2

FOURIER TRANSFORM-PLASMON WAVEGUIDE SPECTROSCOPY: A NON-DESTRUCTIVE MULTI-FREQUENCY METHOD FOR SIMULTANEOUSLY DETERMINING POLYMER THICKNESS AND APPARENT INDEX OF REFRACTION

Reprinted with permission from Bobbitt, J. M.; Weibel, S. C.; Elshobaki, M.; Chaudhary, S.; Smith, E. A., Fourier Transform-Plasmon Waveguide Spectroscopy: A Nondestructive Multifrequency Method for Simultaneously Determining Polymer Thickness and Apparent Index of Refraction. *Anal. Chem.* **2014,** *86* (24), 11957-11961. Copyright 2014 American Chemical Society.

Jonathan M. Bobbitt[1, 2], Stephen C. Weibel[3], Moneim Elshobaki[5, 6], Sumit Chaudhary[4, 5], and Emily A. Smith[1, 2]

[1]The Ames Laboratory, U.S. Department of Energy, Ames, Iowa, 50011, United States

[2]Department of Chemistry, Iowa State University, Ames, Iowa 50011, United States

[3]GWC Technologies Inc., Madison, Wisconsin 53719, United States

[4]Department of Electrical and Computer Engineering, Iowa State University, Ames, Iowa 50011, United States

[5]Department of Materials Science and Engineering, Iowa State University, Ames, Iowa 50011, United States

المنارة للاستشارات

www.manaraa.com

[6]Department of Physics, Mansoura University, Mansoura, 35516, Egypt

Abstract

Fourier transform (FT)-plasmon waveguide resonance (PWR) spectroscopy measures light reflectivity at a waveguide interface as the incident frequency and angle are scanned. Under conditions of total internal reflection, the reflected light intensity is attenuated when the incident frequency and angle satisfy conditions for exciting surface plasmon modes in the metal as well as guided modes within the waveguide. Expanding upon the concept of two-frequency surface plasmon resonance developed by Georgiadis et al., the apparent index of refraction and the thickness of a waveguide can be measured precisely and simultaneously by FT-PWR with an average percent relative error of 0.4%. Measuring reflectivity for a range of frequencies extends the analysis to a wide variety of sample compositions and thicknesses since frequencies with the maximum attenuation can be selected to optimize the analysis. Additionally, the ability to measure reflectivity curves with both p and s-polarized light provides anisotropic indices of refraction. FT-PWR is demonstrated using polystyrene waveguides of varying thickness, and the validity of FT-PWR measurements are verified by comparing the results to data from profilometry and atomic force microscopy (AFM).

Introduction

Spectroscopies based on reflection from an interface, such as surface plasmon resonance (SPR) and plasmon waveguide resonance (PWR), have many applications including monitoring biomolecule interactions and materials characterization.[1-4] In a typical SPR experiment, the reflected light intensity is measured from a prism/thin noble

المنارة للاستشارات

www.manaraa.com

metal film interface. Under conditions of total internal reflection, the reflected light intensity is attenuated when surface plasmons are excited in the smooth metal film. The resonant conditions are susceptible to slight changes in the index of refraction of the layer adjacent to the metallic film, making SPR quite sensitive.[5,6] In a PWR experiment, the reflected light intensity is recorded at a prism/noble metal film/waveguide interface (Figure 1).

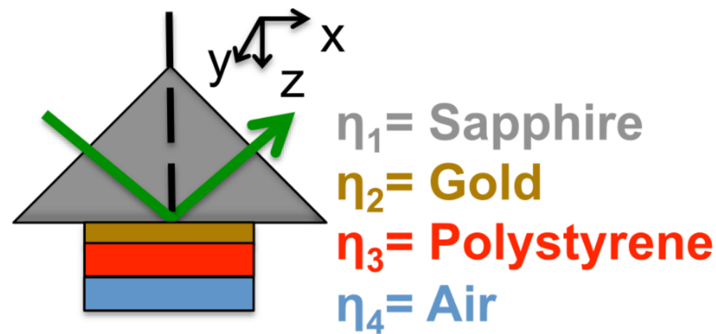

Figure 1: Representative sample setup for a FT-PWR experiment.

A dielectric material will function as a waveguide when its thickness is greater than ~ $\frac{\lambda}{2\eta}$ where λ is the wavelength of light and η is the dielectric's index of refraction. Under total internal reflection, surface plasmons in the noble metal film as well as the guided modes in the dielectric material can be excited at certain angles. PWR reflectivity curves are narrower than SPR reflectivity curves due to the electromagnetic field within the dielectric material having a greater propagation distance. This leads to better sensitivity for PWR than SPR.[7] Both p and s-polarized light can be used to excite guided modes in PWR, which enables anisotropic properties to be measured.[8,9]

المنارة للاستشارات
www.manaraa.com

SPR measurements with a single excitation frequency can determine adsorbate thickness or the dielectric constant, but not both parameters simultaneously. Peterlinz et al. developed a method using two frequencies of light to determine both parameters concurrently without the need to change solvents.[10] The method works by determining the continuum solution to equation 1 at two incident frequencies, where k is the plasmon wave vector, η is the index of refraction for the analyte layer, and d is the thickness of the analyte layer.

$$\boldsymbol{k} = \boldsymbol{\eta} \times \boldsymbol{d} \quad (\mathbf{1})$$

Peterlinz et. al. termed the continuum solutions trial curves.[10] In theory using more than two frequencies provides a more accurate determination of the intersection point of the trial curves, thus providing a more accurate apparent index of refraction and thickness of the analyte layer. A three frequency analysis has been reported for thin films as well as waveguides.[11]

A white light source can be used to scan through a range of frequencies at a fixed incident angle to generate reflectivity curves. This has been demonstrated for SPR.[12-14] However, to the best of our knowledge no frequency scanning technique has been used with a PWR substrate to measure adsorbate thickness and dielectric constant. The sensitivity of a frequency scanning SPR technique increases as lower frequencies are used.[14] Frutos et al. demonstrated the advantages of using frequencies in the infrared region below 3.3×10^{14} Hz with a Fourier transform (FT)-SPR spectrometer.[15] More recently FT-SPR has been used in biological studies, to monitor polyelectrolyte multilayer assembly, non-specific and specific interactions on functionalized polymer surfaces, and to study sputtered indium tin oxide film deposition characteristics.[16-24]

المنارة للاستشارات
www.manaraa.com

Herein we describe the technique FT-PWR for simultaneous measurements of apparent index of refraction and thickness using narrow reflectivity curves. This work combines the multiplexing capabilities of FT to perform a multi-frequency analyses. FT-PWR offers the flexibility of selecting frequencies of interest to the user or frequencies that produce the greatest attenuation of the reflectivity for a given sample, and is less costly with respect to time and money compared to an instrument with multiple, single-frequency sources. There is an increasing demand for non-destructive techniques to measure optical properties of thin films, such as those found in sensors, organic solar cells, catalytic films, lithographically-produced electronics, and coatings for biomedical applications. FT-PWR is a non-destructive technique capable of determining this information.

Materials and Methods

Sample preparation

The gold films were supplied by GWC Technologies Inc., Madison, WI, or fabricated at Oak Ridge National Laboratory's Center for Nanophase Materials Sciences, Oak Ridge, TN. A Ti adhesion layer (2 nm) and Au layer (50 nm ± 5) were deposited onto a 25.4 mm diameter sapphire disk (Meller Optics, Providence, RI). After the deposition, the slides were washed with 2-propanol (Fisher Scientific, Waltham, MA) and dried with nitrogen gas. An 8.48, 8.27, 6.48 and 5.47 wt.% polystyrene (Sigma-Aldrich, St. Louis, MO) in toluene (Fisher Scientific, Waltham, MA) solution was prepared. The films were prepared by spin coating 200 µL of polystyrene solution onto the gold films using a KW-4A spin coater (Chemat Technology, Northridge, CA) at 3000 RPM for 60 seconds.[25] The polystyrene solutions were also spin coated onto 25-mm square glass

المنارة للاستشارات
www.manaraa.com

cover slips (Corning Inc., Corning, NY) to determine an average thickness by the NewView™ 7100 Profilometer (Zygo, Middlefield, CT). A Veeco Digital Instruments AFM was used to measure the thickness of the FT-PWR films. The films were scratched using a sharp needle, and the resulting profile was scanned at scan rate and size of 0.1 Hz (170 μm × 5 μm), respectively.

Instrumentation and FT-PWR measurements

FT-PWR data were collected on the SPR100, which is an integrated system developed by GWC Technologies, Inc. A Thermo Nexus FT-IR (Thermo Fisher Scientific Inc., Waltham, Ma) consisting of a tungsten lamp, a calcium fluoride beamsplitter, and an external collimated beam was coupled to a FT-SPR module (GWC Technologies, Inc.). The module has beam shaping optics (telescope design), a silicon detector, and a motorized rotation stage. Reflectivity was measured from 18,000 to 8800 cm^{-1} while the incident angle was scanned from 36 to 60°. The FT- PWR measurements were an average of 32 scans with a 32 cm^{-1} resolution and an incident angle resolution of 0.25°. Reported incident angles were corrected for the refraction within the prism using Snell's law, and experimental reflectivity curves were shifted by 0.95° to match the calculated reflectivity curves.

Calculated reflectivity curves

The reflected light was modeled by Fresnel calculations as outlined by Hansen using in-house developed programs.[26] All calculations were performed over an angular range of 0.00 to 90.00° with a resolution of 0.01°. Indices of refraction from the literature at specified frequencies were used to develop a fit equation to extrapolate to values at

www.manaraa.com

other frequencies for sapphire,[27] water,[28] and polystyrene.[29] The complex indices of refraction for the gold films used in this study were determined by fitting experimental data shown in Figure S1. The real (η_{Au}) and imaginary (k_{Au}) indices of refraction at 6 wavenumbers were fit to a polynomial or linear function, respectively (Figure S2). The equations for η_{Au} and k_{Au} are presented in equations 2 and 3, where $\tilde{\nu}$ represents the wavenumber of light.

$$\eta_{Au} = 1.259 \times 10^{-8} \cdot \tilde{\nu}^2 - 3.270 \times 10^{-4} \cdot \tilde{\nu} + 2.248 \quad (2)$$

$$k_{Au} = 17.32 - 9.292 \times 10^{-4} \cdot \tilde{\nu} \quad (3)$$

Equations 2 and 3 were used to calculate values at other frequencies above 14924 cm^{-1}. These fit functions qualitatively agree with values found in literature over the range 14286 to 9091 cm^{-1}.[30] The index of refraction used for air was 1.00 over the entire frequency range.[31]

Data Analysis

The FT-PWR data consists of reflectivity values at a range of incident frequencies and angles. To determine the angle of maximum attenuation at a selected wavenumber, a 2.55° region of the experimental FT- PWR reflectivity curve was fit to a Voigt profile using the “Multipeak fitting 2” algorithm in IGOR Pro 6.34A. The Voigt function, a combination of Gaussian and Lorentzian, produced the smallest residual.

The polystyrene thickness (d) versus index of refraction (η) curves, hereafter trial curves, were constructed by fitting the reflectivity as a function of incident angle and fixed frequency using Fresnel reflectivity coefficients. The index of refraction was varied from 1.55 to 1.80 in 0.05 increments (unless otherwise noted) and the thickness was

المنارة للاستشارات
www.manaraa.com

optimized until the experimental and calculated maximum attenuation were within ± 0.001°. The goal of the analysis was to determine the intersection point(s) from among all the trial curves generated for selected wavenumbers. Since the index of refraction is wavenumber dependent, trial curves must be adjusted for dispersion and compared to a single reference wavenumber. The *wavelength* dependence of a transparent material's index of refraction in the visible and near infrared regions follows Cauchy's equation.[29] Equation 4 represents the fit to Cauchy's equation in units of wavenumbers for polystyrene's index of refraction. The dispersion was calculated by taking the derivative of equation 4 as shown in equation 5. The dispersion adjustment for the non-reference wavenumbers were calculated using equation 6. In equation 6, $\tilde{\nu}_2$ represents the reference wavenumber and $\tilde{\nu}_1$ represents the wavenumber for the trial curve being adjusted for dispersion.

$$\eta(\tilde{\nu}) = 1.563 + 1.000 \times 10^{-10} \cdot \tilde{\nu}^2 - 6.471 \times 10^{-21} \cdot \tilde{\nu}^4 \quad (4)$$

$$\frac{d\eta}{d\tilde{\nu}} = 2.000 \times 10^{-10} \cdot \tilde{\nu} - 2.588 \times 10^{-20} \cdot \tilde{\nu}^3 \quad (5)$$

$$\eta(\tilde{\nu}_2) = \eta(\tilde{\nu}_1) + \frac{d\eta}{d\tilde{\nu}} \times (\tilde{\nu}_2 - \tilde{\nu}_1) \quad (6)$$

Once adjusted for dispersion, all trial curves were fit to an offset exponential function unless otherwise stated. The intersection point of the fit functions was found using the fsolve function in MATLAB R2014a (The MathWorks, Inc., Natick, MA).

Results and Discussion

FT-PWR measurements of polystyrene waveguides

The purpose of this work is to demonstrate the FT-PWR technique and its use to accurately measure both the thickness and an apparent index of refraction of polymer

المنارة للاستشارات
www.manaraa.com

waveguides. A polymer film of sufficient thickness will act as a waveguide. The minimum polystyrene thickness required to form a waveguide is ~360 nm for 8803 cm^{-1} incident light and ~175 nm for 17989 cm^{-1}. The frequency and angle where the reflected light intensity is attenuated when a waveguide-supporting film is coated on a plasmon-supporting film depends on the waveguide thickness. More than one waveguide mode may be excited, and attenuation of the reflected light may occur at multiple frequencies and angles. Figure 2A and B show the p-polarized light reflectivity plots for two polystyrene films coated on a 50-nm gold film. The polystyrene films were prepared by spin coating an 8.27 (Figure 2A) or 6.48 (Figure 2B) wt.% polystyrene solution onto the gold film. As measured by profilometry the thicknesses are 690 ± 40 nm and 450 ± 20 nm for the 8.27 and 6.48 wt.% films, respectively. The 690 ± 40 nm polystyrene waveguide has two distinct FT-PWR peaks represented by the blue areas of the plot. These correspond to two waveguide modes. The 450 ± 20 nm polystyrene waveguide has one distinct FT-PWR peak. The surface plasmon mode is not measured for any of the films due to the angle range of the instrument (36 to 60°). The SPR angle at 14000 cm^{-1} is calculated to be 72.30° and 73.13° for polystyrene films with thicknesses of 450 and 690 nm, respectively. The FT-PWR plots provide more information than measurements collected with a fixed frequency or incident angle. For example, at certain incident frequencies, no attenuation of the reflected light is measured at this incident angle range. If using a fixed frequency source, there is a limited range of waveguide thicknesses that can be measured.

المنارة للاستشارات

www.manaraa.com

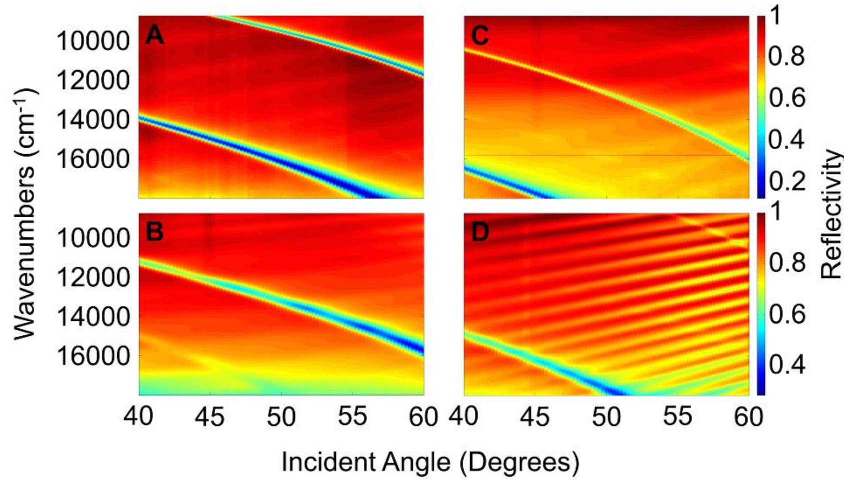

Figure 2: Experimental FT-PWR reflectivity plots of a (A, C) 8.27 wt.% and (B, D) 6.48 wt.% polystyrene waveguide. A and B were collected with p-polarized light and C and D with s-polarized light.

FT-PWR can be used to measure reflectivity of both p and s-polarized light. Figure 2C and D show the s-polarized FT-PWR plots for the 690 ± 40 nm and 450 ± 20 nm polystyrene films, respectively. The s-polarized FT-PWR peaks in Figure 2C and D have a full width at half maximum (FWHM) of 0.39 ± 0.03° (13585 cm^{-1}) and 0.65 ± 0.03° (15828 cm^{-1}). These are generally smaller than the FWHM values for similar waveguide modes generated with p-polarized light, 0.70 ± 0.03° (13585 cm^{-1}) and 1.05 ± 0.05° (15828 cm^{-1}), respectively. Fresnel reflectivity calculations for the above frequencies (13585 and 15828 cm^{-1}) using a 0.001° angle resolution follow the same trend as the experimental results. For 13585 cm^{-1} and 15828 cm^{-1} the calculated difference in the FWHM for the p and s-polarized FT-PWR peak is 0.310°, and 0.400°, respectively. Smaller FWHM can lead to better detection limits and higher precision with sufficient experimental angular and/or spectral resolution.

المنارة للاستشارات
www.manaraa.com

The faint peak starting at 15020 cm^{-1} and 40° in the bottom of Figure 2B has the same characteristics as the more prominent peak in Figure 2D, and is the result of the polarizer leaking s-polarized light when set to p-polarization. The data collected with s-polarized light occasionally had a fringe pattern throughout the plot (Figure 2D), which requires further exploration to explain.

FT-PWR multi-frequency analysis to measure waveguide thickness and apparent index of refraction

In order to use FT-PWR to measure the thickness and apparent index of refraction of the waveguide layer, accurate optical properties at a range of frequencies for all other interfacial layers must be known. A thin gold films' optical properties may vary depending on preparation conditions. To minimize error in the analysis, the index of refraction was experimentally measured as reported in the supplemental information for a gold film prepared at the same time as the films used in subsequent studies.

FT-PWR measurements of waveguide thickness and apparent index of refraction starts with the construction of trial curves. One trial curve is constructed for each wavenumber. FT-PWR makes it possible to construct trial curves for many wavenumbers or at selected optimal wavenumbers of maximum attenuation, which may increase precision compared to the use of two or three fixed frequency sources that may not be ideal for a given sample. Trial curves are constructed for three polystyrene waveguides at three selected wavenumbers with the greatest attenuation across the range 8803 to 17989 cm^{-1}. Figure 3 shows the trial curves for 6.48 (A), 8.27 (B), and 8.48 (C) wt.% polystyrene waveguides. The solid lines indicate trial curves for p-polarized light and the dashed lines in A and B are the trial curves from s-polarized light. The trial curves were

www.manaraa.com

constructed using 6 indices of refraction ranging from 1.5 to 1.8 and a best-fit offset exponential function defined from these points. The intersection of the trial curves represents the solution for the waveguide thickness and apparent index of refraction. The thicknesses are 495 ± 3 and 720.4 ± 0.3 for the polystyrene waveguides in Figure 3A-B, respectively.

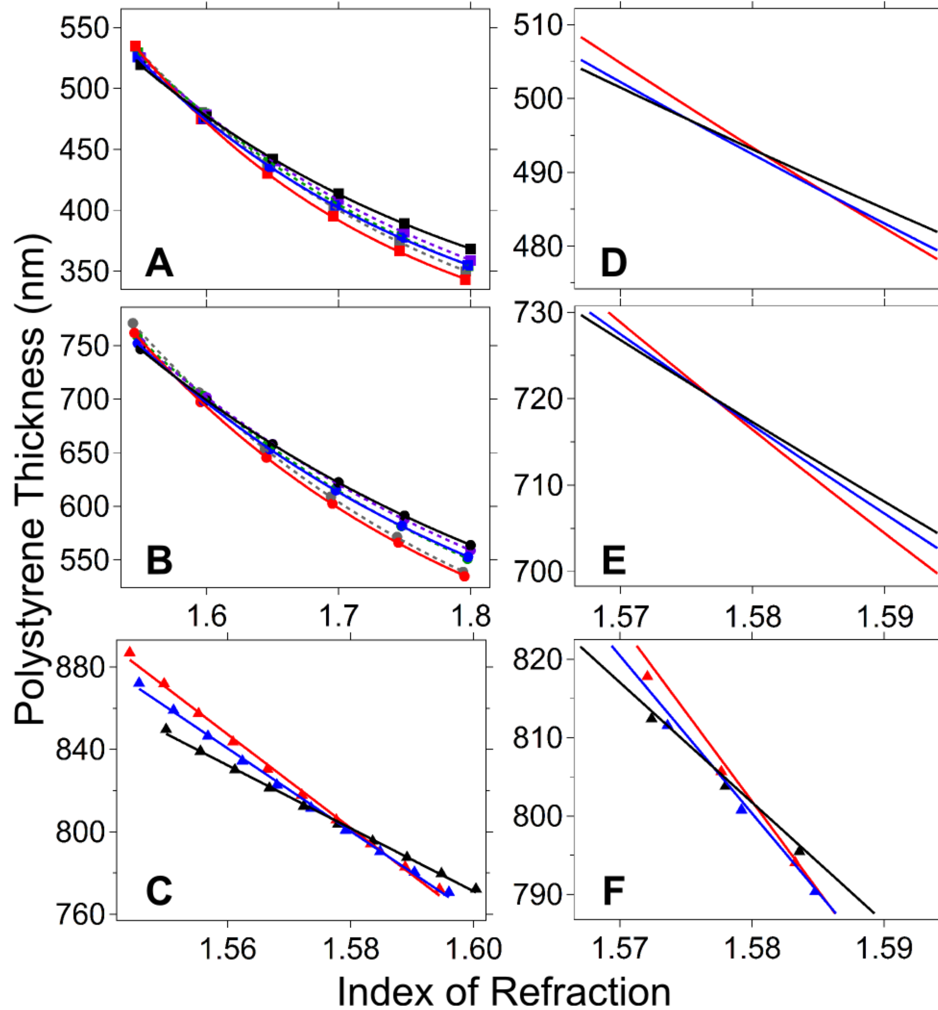

Figure 3: Trial curves for (A) 6.48, (B) 8.27, and (C) 8.48 wt.% polystyrene waveguides where the lines represent the offset exponential fits in (A) and (B) and linear fits in (C) for p- (solid) and s- (dashed) polarized light. (A) 17419 (gray), 16832 (green), 16316 (purple), 14571 (red), 13622 (blue), and 12590 (black) cm^{-1}. (B) 17665 (gray), 16524

www.manaraa.com

(green), 15828 (purple), 15606 (red), 14395 (blue), and 13585 (black) cm^{-1}. (C) 17094 (red), 16399 (blue), and 14680 (black) cm^{-1}. D, E, and F are an expanded view of A, B, and C that show the intersection points for p-polarized light trial curves.

Precision in the determination of polymer thickness using 10 points to construct the trial curves was tested over a 1.55 to 1.60 range of indices of refraction (Figure 3C). The thickness determined over the larger 1.5 to 1.8 range of indices of refraction for the 8.48 wt.% polystyrene waveguide was 803 ± 3 nm. The thickness was 804 ± 3 nm using the narrower 1.55 to 1.60 range of indices of refraction, indicating the precision is not improved compared to the analysis with a larger range of indices of refraction.

The addition of a 4th or 5th trial curve has no significant effect on the precision of the analysis. For the 6.48 wt.% polystyrene waveguide the thickness measured using 3 trial curves is 521 ± 6 nm. Adding a 4th trial curve corresponding to 13560 cm^{-1} gave a thickness of 524 ± 6 nm, and a 5th trial curve corresponding to 12621 cm^{-1} gave a thickness that is not statistically different than the value obtained using 3 or 4 trial curves (525 ± 5 nm). The same result was found for the 8.48 wt.% polystyrene waveguide.

Another consideration that will affect the analysis is determining the appropriate frequencies to construct the trial curves. Trial curves should be constructed using frequencies that produce the maximum attenuation in the reflected light intensity. This is demonstrated with trial curves constructed using three wavenumbers (12612, 13000, and 13530 cm^{-1}) that did not show significant attenuation (i.e., reflectivity in the range 0.6 to 0.8) for the 8.48 wt.% polystyrene waveguide. The thickness measured with these trial curves is 810 ± 10 nm. This is statistically similar to the thickness measured using curves

المنارة للاستشارات
www.manaraa.com

generated at wavenumbers where the reflectivity was between 0.1 and 0.3 (Table 1), yet the uncertainty increased over three times when the trial curves are not constructed using wavenumbers with maximum attenuation. If the frequencies selected to construct the trial curves have an angle of maximum attenuation that is separated by less than 1.5°, the trial curves do not intersect. Compared to reflectivity measurements with fixed-frequency sources, the main benefit of FT-PWR is the ability to select optimal frequencies, which is a sample dependent property.

Table 1: Thickness measured by FT-PWR and profilometry and the percent difference between the two techniques for the indicated polystyrene waveguide.

<table>
<tr><th>wt.% PS</th><th>FT-PWR Thickness (nm)</th><th>Profilometry Thickness (nm)</th><th>% Difference FT-PWR and Profilometry</th></tr>
<tr><td>5.47% PS P-pol Light</td><td>361 ± 2</td><td>330 ± 20</td><td>9</td></tr>
<tr><td>6.48%* PS P-pol Light</td><td>495 ± 3</td><td rowspan="2">450 ± 20</td><td>9</td></tr>
<tr><td>6.48% PS S-pol Light</td><td>489.4 ± 0.9</td><td>9</td></tr>
<tr><td>6.48%* PS P-pol Light</td><td>521 ± 6</td><td>470 ± 40</td><td>10</td></tr>
<tr><td>8.27% PS P-pol Light</td><td>720.4 ± 0.3</td><td rowspan="2">690 ± 40</td><td>4</td></tr>
<tr><td>8.27% PS S-pol Light</td><td>711 ± 2</td><td>3</td></tr>
<tr><td>8.48% PS P-pol Light</td><td>803 ± 3</td><td>780 ± 60</td><td>3</td></tr>
</table>

*Different polystyrene waveguides prepared using the same conditions

Table 1 reports the thicknesses obtained from FT-PWR and profilometry for 5 polystyrene waveguides. The average percent difference between the two measurements is 7%, and the greatest difference is with the thinner films. For the same sample and FT-

المنارة للاستشارات
www.manaraa.com

PWR measurements, the percent relative error is smaller using s-polarized excitation compared to p-polarized excitation. Furthermore, the profilometer consistently measured thicknesses that are less than the FT-PWR method. The thicknesses obtained by FT-PWR and profilometry are not performed on the same samples since the gold film affected the profilometry measurements. Selected polystyrene waveguides measured by FT-PWR were also measured by AFM; the AFM thickness values are statistically similar to the values determined by profilometry for samples prepared on a glass slide but otherwise identical sample preparation methods. Reproducibility of the spin coater and different substrate compositions did not contribute to the percent differences measured by FT-PWR and profilometry. In order to obtain thicknesses using profilometry or AFM the polystyrene film must be scratched away. The lower thicknesses measured by profilometry and AFM could be the result of polymer remaining on the substrate after scratching the surface. The ability to obtain thicknesses from the FT-PWR analysis depends on the accuracy of the index of refraction values used to model the data as already explained.

Comparing the apparent index of refraction at the same frequency for p versus s-polarized light provides information on anisotropic properties. For the 8.27 wt.% polystyrene waveguide, the p and s-polarized light provide statistically different indices of refraction at 15828 cm^{-1}: 1.580 ± 0.002 for p-polarized light and 1.591 ± 0.003 for s-polarized light. Similarly, 13585 cm^{-1} gave values of 1.5767 ± 0.0004 for p-polarized light and 1.5848 ± 0.0009 for s-polarized light. The differences between indices of refraction for p and s-polarized light indicate the polystyrene film is anisotropic. Stress birefringence as a result of film preparation conditions may explain this.[32] The thinner

www.manaraa.com

6.48 wt.% polystyrene waveguide had statistically similar indices of refraction for p and s-polarized light indicating the anisotropy is thickness dependent.

Conclusions

FT-PWR is a non-destructive technique capable of providing the apparent anisotropic indices of refraction and thicknesses for a dielectric waveguide layer suitable for total internal reflection. This technique provides better precision in determining polystyrene thickness compared to techniques like profilometry, while still maintaining the integrity of the polystyrene waveguide. FT-PWR analyses are not limited to polymer films. For example, the polystyrene layer can be replaced with a silica waveguide layer. Monitoring adsorption to the silica surface, or a modified silica surface, should be possible using FT-PWR. It is expected that FT-PWR can be used to quantify and detect anisotropic analytes at low concentrations when adsorbed to a waveguide interface and will be useful as a label free sensor for many applications.

Acknowledgements

This research is supported by the U.S. Department of Energy, Office of Basic Energy Sciences, Division of Chemical Sciences, Geosciences, and Biosciences through the Ames Laboratory. The Ames Laboratory is operated for the U.S. Department of Energy by Iowa State University under Contract No. DE-AC02-07CH11358. Gold film fabrication was conducted at the Center for Nanophase Materials Sciences, which is a DOE Office of Science User Facility. The authors thank Mr. Wyman Martinek (Iowa State University, College of Engineering) for allowing the use of the NewView™ 7100 Profilometer for thickness measurements.

www.manaraa.com

References

(1) Campbell, J. S. S.-P. a. C. T. *Analytical chemistry* **2004**, *76*, 907-917.

(2) I.D. Alves, C. K. P., and V.J. Hruby. *Current Protein and Peptide Science* **2005**, *6*, 293-312.

(3) Huang, H.; Chen, Y. *Biosensors & bioelectronics* **2006**, *22*, 644-648.

(4) Beusink, J. B.; Lokate, A. M.; Besselink, G. A.; Pruijn, G. J.; Schasfoort, R. B. *Biosensors & bioelectronics* **2008**, *23*, 839-844.

(5) Karl D. Pavey, C. J. O. *Biomaterials* **1999**, *20*, 885-890.

(6) Rothenhausler, B.; Knoll, W. *Nature* **1988**, *332*, 615-617.

(7) Byard, C. L.; Han, X.; Mendes, S. B. *Analytical chemistry* **2012**, *84*, 9762-9767.

(8) Hruby, V. J.; Alves, I.; Cowell, S.; Salamon, Z.; Tollin, G. *Life Sciences* **2010**, *86*, 569-574.

(9) Harte, E.; Maalouli, N.; Shalabney, A.; Texier, E.; Berthelot, K.; Lecomte, S.; Alves, I. D. *Chemical communications* **2014**, *50*, 4168-4171.

(10) Peterlinz, K. A.; Georgiadis, R. *Optics Communications* **1996**, *130*, 260-266.

(11) Granqvist, N.; Liang, H.; Laurila, T.; Sadowski, J.; Yliperttula, M.; Viitala, T. *Langmuir* **2013**, *29*, 8561-8571.

(12) Aldinger, U.; Pfeifer, P.; Schwotzer, G.; Steinrücke, P. *Sensors and Actuators B: Chemical* **1998**, *51*, 298-304.

المنارة للاستشارات
www.manaraa.com

(13) Johnston, K. S.; Mar, M.; Yee, S. S. *Sensors and Actuators B: Chemical* **1999**, *54*, 57-65.

(14) Homola, J. *Sensors and Actuators B: Chemical* **1997**, *41*, 207-211.

(15) Anthony, G. F.; Stephen, C. W.; Robert, M. C. *Analytical chemistry* **1999**, *71*.

(16) Arena, G.; Contino, A.; D'Agata, R.; Sgarlata, C.; Spoto, G. *New Journal of Chemistry* **2005**, *29*, 1393.

(17) Ziblat, R.; Lirtsman, V.; Davidov, D.; Aroeti, B. *Biophysical journal* **2006**, *90*, 2592-2599.

(18) Lee, H. J.; Wark, A. W.; Corn, R. M. *Journal of Physics: Condensed Matter* **2007**, *19*, 375107.

(19) Lirtsman, V.; Golosovsky, M.; Davidov, D. *Journal of Applied Physics* **2008**, *103*, 014702.

(20) Soheil Boddohi, C. E. K., and Matt J. Kipper. *Biomacromolecules* **2008**, *9*, 2021-2028.

(21) Boujday, S.; Methivier, C.; Beccard, B.; Pradier, C. M. *Analytical biochemistry* **2009**, *387*, 194-201.

(22) Almodovar, J.; Place, L. W.; Gogolski, J.; Erickson, K.; Kipper, M. J. *Biomacromolecules* **2011**, *12*, 2755-2765.

(23) Wei, J.; Yan, L.; Hu, X.; Chen, X.; Huang, Y.; Jing, X. *Colloids Surf B Biointerfaces* **2011**, *83*, 220-228.

المنارة للاستشارات

www.manaraa.com

(24) Losego, M. D.; Efremenko, A. Y.; Rhodes, C. L.; Cerruti, M. G.; Franzen, S.; Maria, J.-P. *Journal of Applied Physics* **2009**, *106*, 024903.

(25) Matthew, W. M.; Kristopher, J. M.; Vy, H. T. N.; Emily, A. S. *The Journal of Physical Chemistry C* **2012**, *116*.

(26) Hansen, W. N. *Journal of The Optical Society of America.* **1968**, *58*, 380-390.

(27) Bass, M.; DeCusatis, C.; Enoch, J.; Lakshminarayanan, V.; Li, G.; MacDonald, C.; Mahajan, V.; Van Stryland, E. *Handbook of Optics, Third Edition Volume IV: Optical Properties of Materials, Nonlinear Optics, Quantum Optics (set)*; Mcgraw-hill, 2009.

(28) Daimon, M.; Masumura, A. *Applied Optics* **2007**, *46*, 3811-3820.

(29) Kasarova, S. N.; Sultanova, N. G.; Ivanov, C. D.; Nikolov, I. D. *Optical Materials* **2007**, *29*, 1481-1490.

(30) Johnson, P. B.; Christy, R. W. *Physical Review B* **1972**, *6*, 4370-4379.

(31) Ciddor, P. E. *Applied optics* **1996**, *35*, 1566-1573.

(32) Mark, H. F.; Bikales, N.; Kroschwitz, J. I. *Encyclopedia of Polymer Science and Engineering, Styrene Polymers to Toys*; Wiley, 1989.

المنارة للاستشارات

www.manaraa.com

Supporting Information

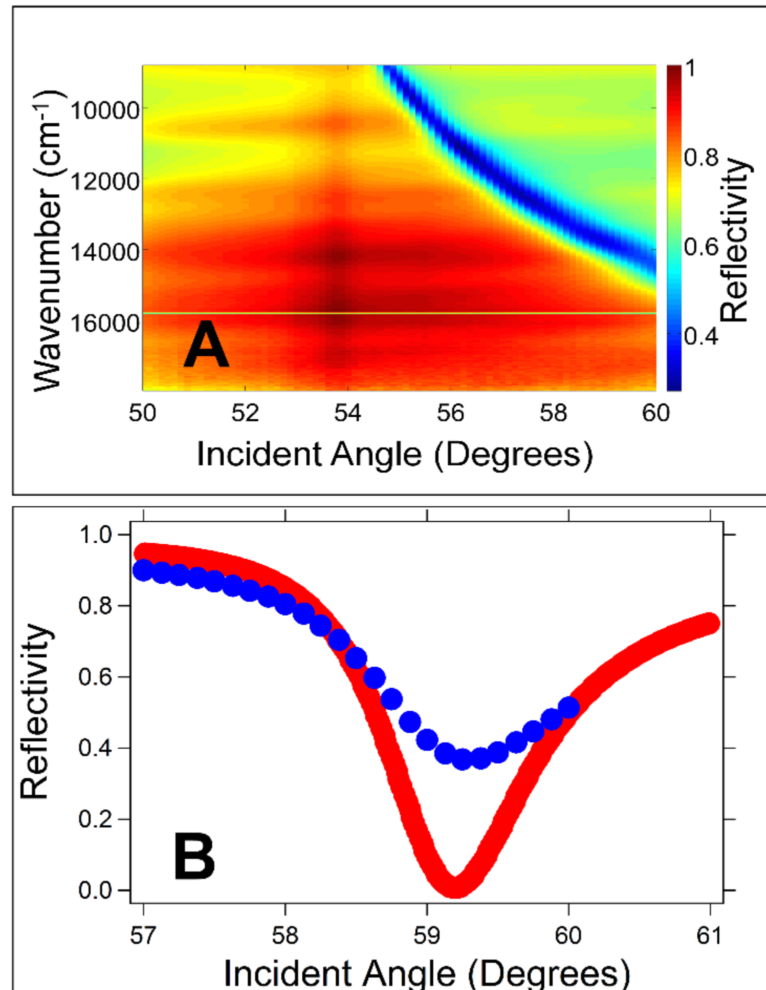

Figure S1: (A) Fourier transform (FT)-surface plasmon resonance (SPR) reflectivity plot of a 50-nm gold film. The data were used to determine the index of refraction at selected wavenumbers by fitting the reflectivity as a function of incident angle at a fixed wavenumber. The critical angle is 53.88° at 8803 cm^{-1} and 53.63° at 17980 cm^{-1}. Due to the angular resolution used in this work, the critical angle appears as a vertical line. The green horizontal line is the wavenumber of the reference laser. (B) Representative reflectivity curve at 14002 cm^{-1} from the data shown in A with experimental data (blue

المنارة للاستشارات

www.manaraa.com

circles) and the calculated fit (red circles). The discrepancy in the attenuation between the experimental data and the calculated fit may be the result of imperfect gold films, for example the possible incorporation of a contaminant.

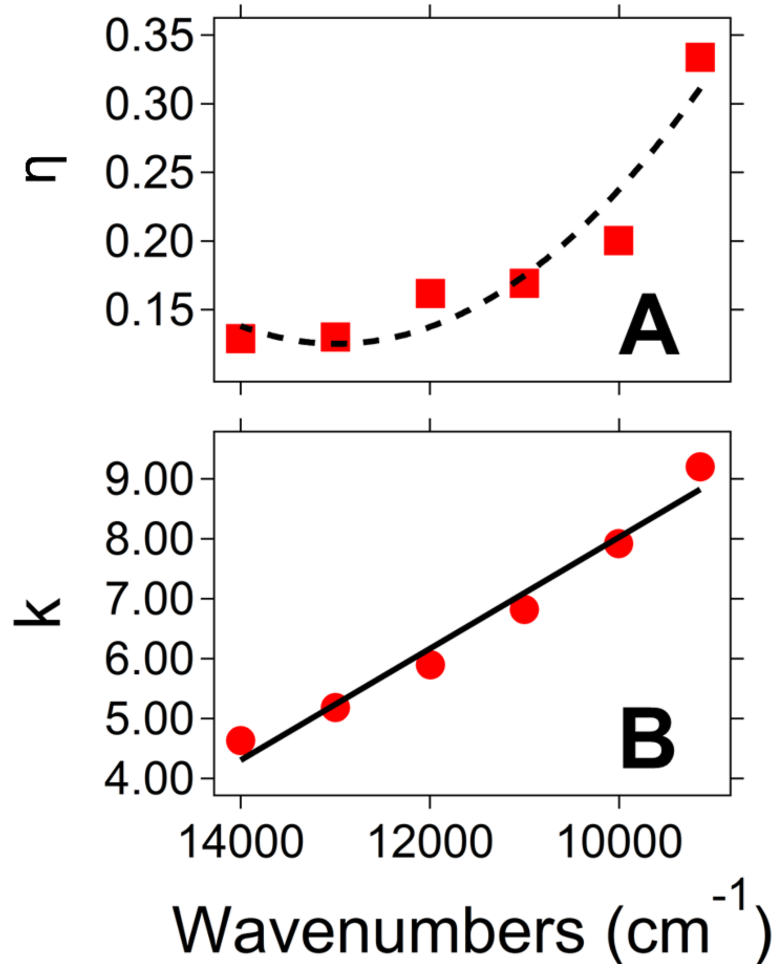

Figure S2: The index of refraction for a 50-nm gold film was determined by fitting SPR curves from 6 different wavenumbers ranging from 14002 to 9141 cm^{-1} (red symbols). Graphs A and B show the offset polynomial regression (dashed black line) for the real part (72.30°) and a linear regression (solid black line) for the imaginary part (k) of the index of refraction.

www.manaraa.com

CHAPTER 3

SCANNING ANGLE RAMAN SPECTROSCOPY: A NONDESTRUCTIVE METHOD FOR SIMULTANEOUSLY DETERMINING MIXED POLYMER FRACTIONAL COMPOSITION AND FILM THICKNESS

Reprinted from Polymer, 107, Bobbitt, J. M.; Mendivelso-Pérez, D.; Smith, E. A., scanning angle Raman spectroscopy: a nondestructive method for simultaneously determining mixed polymer fractional composition and film thickness, 82-88, Copyright (2016), with permission from Elsevier.

Jonathan M. Bobbitt, Deyny Mendivelso-Pérez, Emily A. Smith

The Ames Laboratory, U.S. Department of Energy, and Department of Chemistry, Iowa State University, Ames, Iowa 50011, United States

Abstract

A scanning angle (SA) Raman spectroscopy method was developed to simultaneously measure the chemical composition and thickness of waveguide mixed polymer films with varying fractional compositions. In order to test the method, six films of polystyrene-block-poly(methyl methacrylate), some mixed with poly(methyl methacrylate) homopolymer (PS-b-PMMA:PMMA), and two films of poly(2-vinylnapthalene)-block-poly(methyl methacrylate) (P2VN-b-PMMA) were prepared. The

www.manaraa.com

film thickness ranged from 495 to 971 nm. The chemical composition and thickness of PS-b-PMMA:PMMA films was varied by the addition of the PMMA homopolymer and annealing the films in acetone. SA Raman peak amplitude ratios (1001 cm^{-1} for PS, 812 cm^{-1} for PMMA, and 1388 cm^{-1} for P2VN) were used to calculate the refractive index of the polymer film, an input parameter in calculations of the sum square electric field (SSEF). The film thickness was determined by SSEF models of the experimental Raman amplitudes versus the incident angle of light. The average film thickness determined by the developed SA Raman spectroscopy method was within 5% of the value determined by optical profilometry. SA Raman spectroscopy will be useful for *in situ* label-free analyses of mixed polymer waveguide films.

Introduction

Analysis and characterization of polymer and mixed polymer films is important due to their increasing use in energy storage and capture devices,[1-3] microelectronics,[4-6] optics,[7,8] and biomedical applications.[9,10] The chemical composition and thickness of the films are important to device performance, and for accurately modeling and optimizing new devices before fabrication. Ellipsometry is a common noninvasive optical-based technique that measures the thickness of polymer films, but the technique does not provide chemical content information.[11,12] Other methods for measuring polymer film thicknesses are profilometry and atomic force microscopy (AFM).[13] Profilometry and AFM require a probe to be in contact with the sample surface and for the film to be scratched in order to measure the film thickness, respectively.

Scanning electron microscopy (SEM) and transmission electron microscopy (TEM) can produce high spatial resolution images of polymer and mixed polymer films,

المنارة للاستشارات
www.manaraa.com

and with the use of heavy metal staining different chemical components can be distinguished.[14-17] SEM provides information on the film surface, but does not provide information from the bulk of the film. TEM provides higher resolution images compared to SEM, but requires more rigorous sample preparation. TEM is used to study the internal structure of a sample by showing regions of high or low electron density due to the number of electrons transmitted through the sample. Secondary ion mass spectrometry can also provide information on the internal structure and thickness of the film when operated in a depth profiling mode.[18,19] All the above characterization techniques provide high resolution information; however, the techniques are sample destructive and are not well suited for *in situ* measurements.

Vibrational spectroscopy is nondestructive and provides information on chemical structure. Attenuated total reflection infrared spectroscopy is capable of measuring polymer film thicknesses with a spatial resolution of 10 μm and providing chemical content information; however, the evanescent wave penetration depth varies across the spectrum complicating the data analysis.[20-23] Raman spectroscopy is an inelastic optical scattering effect that relies on the polarizability of a molecule. Raman spectroscopy using conventional illumination geometries (*e.g.*, epi-illumination) cannot simultaneously measure the fractional composition and film thickness, and is not well suited for films with thicknesses in the hundreds of nanometers regime. Scanning angle (SA) Raman spectroscopy is a nondestructive technique that has been used to measure thickness and buried interfaces of thin polymer films.[24-26] It can be used for polymer films of tens of nanometers to a few microns in thickness. A SA Raman dataset consist of Raman

المنارة للاستشارات
www.manaraa.com

amplitudes as a function of Raman shift and incident angle for a sample optically interfaced to a prism as shown in Figure 1.

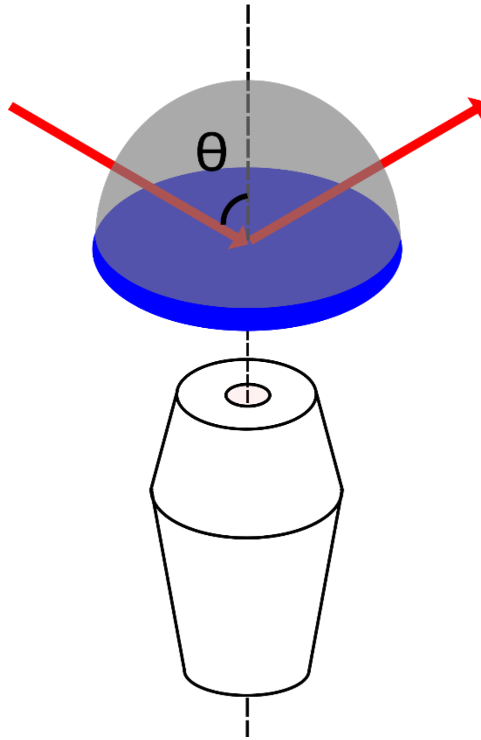

Figure 1: Schematic of the sample setup for SA Raman spectroscopy where the light (red arrow) is coupled through a prism (gray hemisphere) to generate the Raman signal as the incident angle of light is scanned. This signal is collected by a 10× microscope objective from below the sample. The blue layer represents the polymer film sample.

A dielectric material (*e.g.*, polymer film) will act as a waveguide when the film thickness is greater than $\approx \frac{\lambda}{2\eta}$, where λ is the wavelength of light and η is the refractive index for the dielectric. Light coupled into a waveguide via a prism will be confined to propagate within the film and will exhibit constructive or destructive interference at various incident angles, which are recorded in the Raman spectra collected at varying incident angles. Plots of the Raman peak amplitude versus incident angle show the

المنارة للاستشارات
www.manaraa.com

waveguide mode(s). The waveguide mode location and full width at half maximum values (fwhm) can be modeled with sum square electric field (SSEF) calculations when the refractive index or film thickness is known.

Outlined herein is a nondestructive method using SA Raman spectroscopy combined with SSEF calculations to extract the fractional composition and thickness of mixed polymer waveguide films. This work extends previous studies of homopolymer films reported by Meyer et al. that used SA Raman spectroscopy to measure film thickness when the index of refraction was known.[24] Herein, the method was demonstrated using thin polystyrene-block-poly(methyl methacrylate) (PS-b-PMMA) films, PS-b-PMMA with added PMMA homopolymer (PS-b-PMMA:PMMA) mixed films, and poly(2-vinylnapthalene)-block-poly(methyl methacrylate) (P2VN-b-PMMA) films. PS-b-PMMA and P2VN-b-PMMA are block copolymers that consist of two or more chemically dissimilar homopolymer (blocks) that are covalently attached. Block copolymers have been previously implemented in nanolithography to create masks for a variety of applications ranging from circuit and nanowire array fabrication to homogenous nanocluster arrays for surface-enhanced Raman scattering substrates.[27-31] In the present study, these block copolymers are used to make mixed polymer samples with an unknown refractive index and thickness. The demand for nondestructive techniques that measure thin film thickness is continually increasing, and SA Raman spectroscopy can provide this information plus chemical content information on complex polymer mixtures. The method has the capacity to provide real-time (dynamic) measurements during film preparation and post-processing conditions.

المنارة للاستشارات
www.manaraa.com

Materials and Methods

Sample preparation

A 120 mg/mL stock solution of PS-b-PMMA (21500-b-7900 g/mol with a polydispersity index (PDI) of 1.10, Polymer Source, Montréal, Canada) prepared in toluene (Fisher Scientific, Waltham, MA) and a stock solution of 120 mg/mL PMMA (120,000 g/mol with a PDI of 2.0, Sigma Aldrich, St. Louis, MO) in toluene were prepared. The stock solutions were used to prepare 1:2, 1:2.4, 1:2.6, 1:3, and 1:4 (v/v) PS-b-PMMA:PMMA solutions. A 120 mg/mL stock solution of P2VN-b-PMMA in toluene (53000-b-140000 g/mol with a PDI of 1.20, Polymer Source, Montréal, Canada) was used to prepare 133 and 97 mg/mL solutions. To determine the refractive index of P2VN a 120 mg/mL solution of P2VN (PDI of 2.9, Polymer Source, Montréal, Canada) was prepared in toluene. PS-b-PMMA, PS-b-PMMA:PMMA, P2VN-b-PMMA, and P2VN films were prepared by spin coating 200 μL of solution onto 25 mm^2 glass cover slips (Corning Inc., Corning, NY) at 3000 rpm for 60 seconds using a KW-4A spin coater (Chemat Technology, Northridge, CA). The polymer film was placed in a 180 cm^3 glass vessel with 500 μL of acetone added as an annealing solvent, and kept at room temperature (20 $^{\circ}$C). After annealing for 60 minutes, the films were removed from the annealing vessel to let the solvent fully evaporate from the film. The film thicknesses were measured after completing the SA Raman and fluorescence measurements with a NewView 7100 optical profilometer (Zygo, Middlefield, CT). A sharp needle was used to make three scratches in the center of each film to determine the average thickness.

The underlying substrate (*i.e.*, glass or sapphire) affects the properties of the PS-rich and PMMA-rich areas (data not shown). All polymer films were prepared on glass

www.manaraa.com

slides to enable characterizing them with several analysis methods, and the wedge transfer method was used to transfer the films to 25.4 mm diameter sapphire disks (Meller Optics, Providence, RI) for SA Raman measurements.[32] Sapphire prisms and substrates were used for the SA Raman measurements to reduce background in the spectra.[33] Figure S1 shows fluorescence images of a 1:2 PS-b-PMMA:PMMA film prepared on a glass substrate and after transferring it to a sapphire substrate. The images show no discernible changes in the polymer film after the transfer.

Raman measurements

The SA Raman spectra were collected on a home-built instrument, previously described by McKee et al.,[33] where a S-polarized 785-nm laser (Toptica Photonics, Victor, NY) was directed onto a sapphire prism using a galvanometer mirror on a translational stage. The instrument has an angle range of 25.00 to 75.00° with an angular resolution of 0.05°. A 10× objective with a 0.22 numerical aperture (Nikon, Melville, NY) was used to collect the Raman signal and direct it to the side port of the optical microscope (Nikon, Melville, NY), where the light was focused onto a f/1.8i Holospec imaging spectrometer (Kaiser Optical Systems, Ann Arbor, MI). The spectra were collected with a Pixis 400BR charged coupled device (CCD) with 1300 × 400 pixels (Princeton Instruments, Trenton, NJ) for 60 seconds. Two replicate measurements were collected at each angle from 50.0° to 60.0° using a 0.5° step size, except around the waveguide maximum where a step size of 0.2° was used.

Epi-illumination Raman spectra were collected using an XploRA Plus confocal Raman microscope (Horiba Scientific, Edison, NJ) and a 785-nm excitation source. The relative Raman cross-section ratios between PS/PMMA and P2VN/PMMA were

المنارة للاستشارات

www.manaraa.com

determined by melting solid PS, PMMA, and P2VN onto glass substrates. The film thickness was 1.8 ± 0.3, 2.7 ± 0.3, and 2.5 ± 0.2 mm for PS, PMMA, and P2VN, respectively. These thicknesses were sufficient to acquire Raman amplitudes that were independent of the optical focus. Epi-illumination spectra were collected for 5 seconds from 3 different spots on the film. The relative Raman cross-section ratio (σ_R) was calculated using equation 1, where *I* represents the indicated peak amplitude.

$$\sigma_R = \frac{I_{PS,1001cm^{-1} or\ P2VN,1388cm^{-1}}}{I_{PMMA,812cm^{-1}}} = 4.1\ (PS\ to\ PMMA)$$

$$and\ 7.0\ (P2VN\ to\ PMMA)\ (1)$$

The relative Raman cross-section ratio was used in the calculation of the Raman amplitude ratio (r) from the SA Raman data according to equations 2 and 3.

$$r_{PS} = \frac{I_{PS,1001cm^{-1}\ or\ P2VN,1388cm^{-1}}}{I_{PS,1001cm^{-1}\ or\ P2VN,1388cm^{-1}} + (I_{PMMA,812cm^{-1}} \times \sigma_R)}\ (2)$$

$$r_{PMMA} = \frac{I_{PMMA,812cm^{-1}} \times \sigma_R}{I_{PS,1001cm^{-1}\ or\ P2VN,1388cm^{-1}} + (I_{PMMA,812cm^{-1}} \times \sigma_R)}\ (3)$$

All data were processed using Igor Pro 6.37 scientific analysis and graphing software. The spectra were fit to a Gaussian function with a linear baseline using the batch-fit function to extract the peak amplitudes. Matlab 2015b was used to plot the SA Raman spectra as a function of their incident angle.

Sum square electric field calculations

Finite-difference time-domain simulations were used to calculate the SSEF (EM Explorer, San Francisco, CA) within the PS-b-PMMA, PS-b-PMMA:PMMA, and P2VN-b-PMMA films. The inputs needed for the calculations were the refractive index and the thickness for the sapphire prism and polymer film. The refractive index at 785-nm for PS

المنارة للاستشارات
www.manaraa.com

(1.579), PMMA (1.485), P2VN (1.620), and sapphire (1.753) using S-polarized light were found in the literature or measured as reported in the supplemental information (Figure S2).[34-36] An angle range of 50.00° to 60.00° was used for the calculations with a resolution of 0.05° to ensure enough data points were calculated around the waveguide maximum. The Yee cell size was set to 5 nm to provide a compromise between highest accuracy and shortest computational time.

Fluorescence microscopy measurements

A 20-nM solution of Rhodamine 6G was prepared in methanol, and 20 μL was drop cast onto the PS-b-PMMA and PS-b-PMMA:PMMA films after the SA Raman measurements were completed. The films were dried for 10 minutes before images were acquired to allow the methanol to evaporate. Fluorescence images were collected at room temperature using an inverted microscope (Nikon Eclipse, TE2000U, Melville, NY, USA) equipped with a 60× air objective (Nikon Plan Fluor, 0.95 numerical aperture) and an excitation (Chroma HQ500/40, 500 ± 40 nm) and emission (Chroma HQ620/60m, 620 ± 60 nm) filter set for Rhodamine 6G. A mercury lamp was used as an illumination source and the images were captured using a PhotonMAX 512 EMCCD camera (Princeton Instruments, Trenton, NJ, USA) with a 300-millisecond acquisition time.

Results and Discussion

Preparation and preliminary characterization of the polymer samples used to demonstrate the SA Raman method

Polymer waveguide films are made from block copolymer or block copolymer mixed with homopolymer. The amount of PMMA homopolymer added to the PS-b-PMMA:PMMA solution is varied from 1:2 to 1:4 to produce films with varying polymer

المنارة للاستشارات
www.manaraa.com

fractional composition and thickness. Fluorescence and epi-Raman imaging are used to independently verify the fractional composition of the films. There are no observable phase segregated domains in the fluorescence image of a PS-b-PMMA film (figure 2A) without added homopolymer, likely due to the domains being smaller than the diffraction limit of light. However, the addition of PMMA homopolymer increases the size of the phase segregated domains, and they are observable by fluorescence microscopy (Figure 2B-F).

The chemical identities of the phases measured by fluorescence are determined using epi-illumination Raman imaging (Figure S3). The high fluorescence intensity regions contain primarily PMMA with $8.6 \pm 0.2\%$ PS. The low fluorescence intensity regions contain primarily PS with $32.9 \pm 0.3\%$ of PMMA.

المنارة للاستشارات
www.manaraa.com

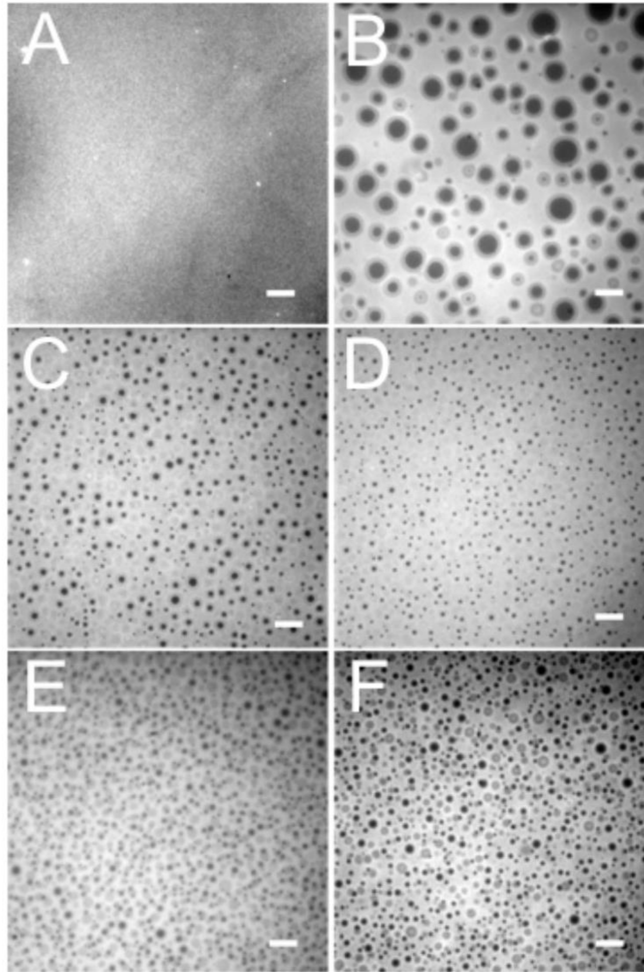

Figure 2: Fluorescence images collected with a 60× objective with the low fluorescence regions corresponding to PS-rich areas and the high fluorescence regions corresponding to PMMA-rich areas. (A) shows the PS-b-PMMA film. (B) shows the 1:2 PS-b-PMMA:PMMA film with a fluorescence area ratio of 0.27 ± 0.02. (C) shows the 1:2.4 PS-b-PMMA:PMMA film with a fluorescence area ratio of 0.21 ± 0.01. (D) shows the 1:2.6 PS-b-PMMA:PMMA film with a fluorescence area ratio of 0.181 ± 0.002. (E) shows the 1:3 PS-b-PMMA:PMMA film with a fluorescence area ratio of 0.180 ± 0.007. (F) shows the 1:4 PS-b-PMMA:PMMA film with a fluorescence area ratio of 0.170 ± 0.007. The scale bar is 9 μm for all images.

المنارة للاستشارات

www.manaraa.com

Development of a SA Raman method for determining fractional composition and film thickness

A 0.12 mm^2 area is illuminated in the SA Raman measurements. This is an area larger than the full images shown in Figure 2, so multiple PS-rich domains and a large PMMA-rich area are measured. The SA Raman data for the PS-b-PMMA film and five PS-b-PMMA:PMMA films with varying amounts of added homopolymer are plotted in the left column of Figure 3 as their Raman shift versus the incident angle with the color scale representing the Raman amplitudes. All the polymer films are plotted on the same color scale ranging from 500 to 8000 counts.

www.manaraa.com

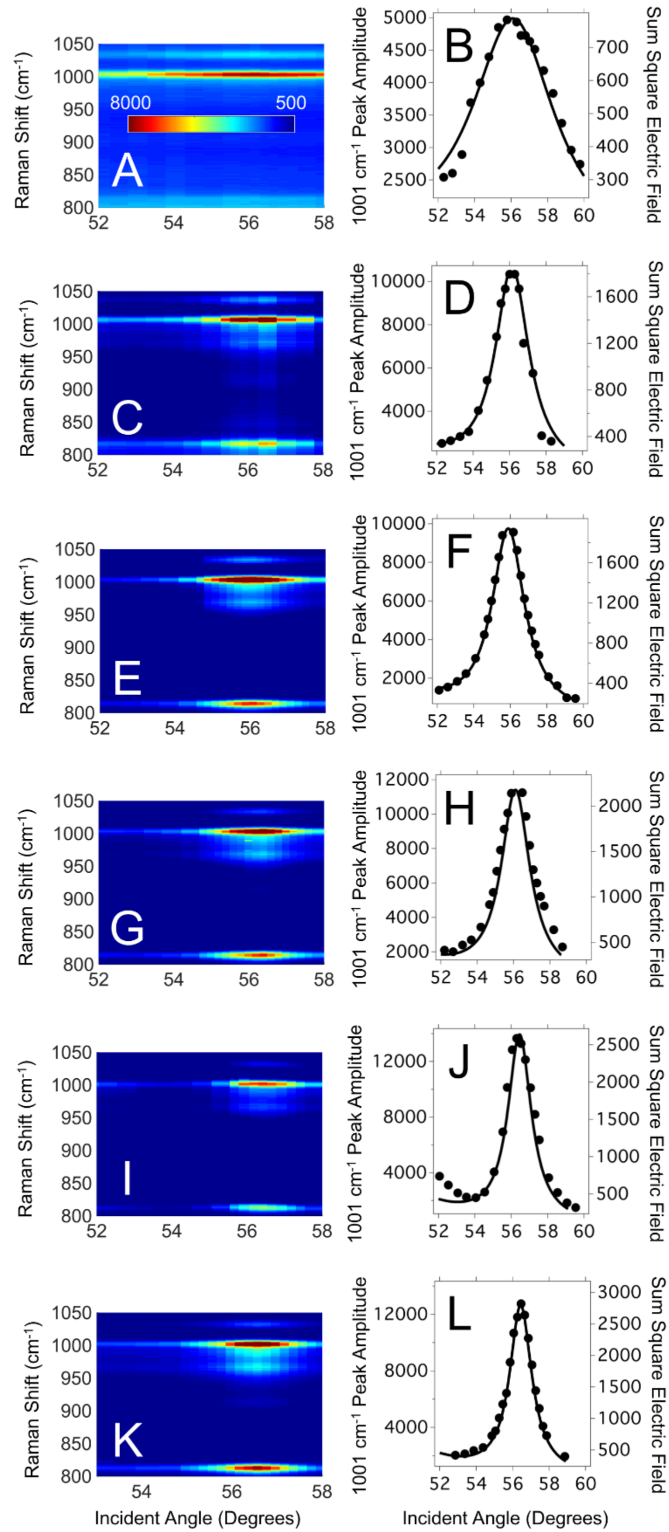

Figure 3: (A, C, E, G, I, and K) SA Raman spectra of PS-b-PMMA and PS-b-PMMA:PMMA films plotted on the same color amplitude scale shown in (A). (B, D, F,

المنارة للاستشارات
www.manaraa.com

H, J, and L) show the 1001 cm^{-1} PS peak amplitude versus incident angle spectra and the solid black line is the SSEF fit for each sample. (A and B) PS-b-PMMA, (C and D) 1:2 PS-b-PMMA:PMMA, (E and F) 1:2.4 PS-b-PMMA:PMMA, (G and H) 1:2.6 PS-b-PMMA:PMMA, (I and J) 1:3 PS-b-PMMA:PMMA, and (K and L) 1:4 PS-b-PMMA:PMMA films.

Figure 3A shows the SA Raman spectra at all collected incident angles for the PS-b-PMMA film without added homopolymer. The peaks assigned to PS (1001 cm^{-1}) and PMMA (812 cm^{-1}) show a broad waveguide mode from approximately 52.3 to 59.8 degrees. The PMMA peak at 812 cm^{-1} has a significantly lower amplitude compared to the PS peak at 1001 cm^{-1}. This is because there is 2.7× less PMMA in the PS-b-PMMA film, and due to PMMA's smaller Raman cross-section compared to PS. The Raman amplitude ratio (r_{PS}), as defined by equation 2, for the PS-b-PMMA film is 0.78 ± 0.01. This is consistent with the manufacturer's reported 0.73 monomer fraction for this block copolymer film.

Figure 3B shows the cross section of the 1001 cm^{-1} PS peak observed in Figure 3A, where the amplitude (black circles) is plotted versus the incident angle for the PS-b-PMMA film. It has been previously shown that matching the calculated SSEF within the polymer film to the experimental Raman amplitude versus incident angle data can be used to measure the polymer film's thickness when its refractive index is known.[24,25,37] For the PS-b-PMMA and PS-b-PMMA:PMMA films the refractive index is not known at the relevant excitation wavelength for these studies. More generally, there are many mixed polymer films where the index of refraction is not known. However, since the

المنارة للاستشارات
www.manaraa.com

Raman amplitude ratio encodes the fractional composition for the mixed polymer film, it can be used to calculate a refractive index for the polymer film. The Raman amplitude ratio is calculated using equation 2 for each incident angle of light, and then an average over all incident angles is calculated. Finally, the average Raman amplitude ratio is used in equation 4 to determine the polymer film's refractive index (RI_{film}), where RI_{PS} and RI_{PMMA} are the indices of refraction for the homopolymers at the excitation wavelength.

$$\boldsymbol{RI_{film} = (r_{PS} \times RI_{PS}) + \left((1 - r_{PS}) \times RI_{PMMA}\right)} \quad (\mathbf{4})$$

المنارة للاستشارات

www.manaraa.com

Table 1: The Raman amplitude ratios and indices of refraction for the prepared films determined by SA Raman as well as a thickness comparison between SA Raman and profilometry measurements.

Sample	Raman Amplitude Ratio (r_{PS})[1]	Refractive Index (RI)	SA Raman Thickness (nm)	Profilometry Thickness (nm)	Percent Difference (%)
PS-b-PMMA	0.78 ± 0.01	1.558	550	495.4 ± 0.8	10
1:2 PS-b-PMMA:PMMA	0.32 ± 0.01	1.515	780	870 ± 10	10
1:2.4 PS-b-PMMA:PMMA	0.28 ± 0.02	1.511	790	850 ± 70	8
1:2.6 PS-b-PMMA:PMMA	0.27 ± 0.01	1.510	830	824 ± 3	0.8
1:3 PS-b-PMMA:PMMA	0.25 ± 0.04	1.509	920	936 ± 5	2
1:4 PS-b-PMMA:PMMA	0.236 ± 0.006	1.507	900	950 ± 30	6
97.0 mg/mL P2VN-b-PMMA	0.29 ± 0.01	1.525	815	795 ± 6	2
133 mg/mL P2VN-b-PMMA	0.29 ± 0.01	1.525	965	971 ± 8	0.6

[1] This ratio is indicative of the fractional composition of the polymer film.

The refractive index determined from equation 4 is 1.558 for the PS-b-PMMA film. The SSEF calculated using the 1.558 refractive index and a thickness that minimized the residual between the fit and experimental data (black line in Figure 3B), shows a waveguide mode maximum angle at 56.04 ± 0.08° and a fwhm of 4.7 ± 0.3°. The residual between the fit and experimental data is below 10%. There is a 10% difference

المنارة للاستشارات
www.manaraa.com

between the thickness determined by SA Raman spectroscopy and the value measured by profilometry (Table 1).

Figure 3C-L show the SA Raman data and 1001 cm^{-1} PS peak amplitude versus incident angle graphs for the 1:2, 1:2.4, 1:2.6, 1:3, and 1:4 PS-b-PMMA:PMMA films. Compared to the measurement on the PS-b-PMMA film, the PMMA Raman peak amplitude increases for the PS-b-PMMA:PMMA films (Figure 3C, E, G, I. and K). This is consistent with the increasing fractional compositions of PMMA in the polymer films. There is a general decreasing trend in the magnitude of the Raman amplitude ratios (r_{PS}) as more PMMA is added, although not all the values are statistically different (Table 1).

Table 2: Waveguide mode location and fwhm determined by fitting the 1001 cm^{-1} PS peak amplitude versus incident angle spectrum from SA Raman measurements.

Sample	Waveguide Mode Location (°)	Waveguide Mode fwhm (°)
PS-b-PMMA	56.04 ± 0.08	4.7 ± 0.3
1:2 PS-b-PMMA:PMMA	56.06 ± 0.03	2.2 ± 0.1
1:2.4 PS-b-PMMA:PMMA	55.90 ± 0.02	2.06 ± 0.06
1:2.6 PS-b-PMMA:PMMA	56.12 ± 0.02	1.94 ± 0.06
1:3 PS-b-PMMA:PMMA	56.48 ± 0.06	1.7 ± 0.2
1:4 PS-b-PMMA:PMMA	56.46 ± 0.02	1.59 ± 0.05
97.0 mg/mL P2VN-b-PMMA	56.85 ± 0.01	2.10 ± 0.03
133 mg/mL P2VN-b-PMMA	57.95 ± 0.01	1.51 ± 0.03

المنارة للاستشارات
www.manaraa.com

The addition of PMMA homopolymer causes the fwhm of the waveguide mode to narrow compared to the PS-b-PMMA film. Table 2 summarizes the waveguide mode properties for the prepared polymer films. These observed changes in the waveguide mode fwhm are generally indicative of an increase in the film thickness. However, varying the polymer fractional composition also causes a change in the refractive index compared to the PS-b-PMMA film, and this will also affect the waveguide properties. This highlights the need to simultaneously determine both the index of refraction and thickness for each polymer film.

The refractive indices calculated by equation 4 using the experimental Raman amplitude ratios (r_{PS}) for each PS-b-PMMA:PMMA film are shown in Table 1, and are used in the subsequent SSEF calculations to fit the experimental data. As with the PS-b-PMMA film, the best fit is determined by minimizing the residual between the fit and experimental data while changing the polymer film thickness. There is an average 5% difference between the thicknesses measured by SA Raman spectroscopy and profilometry for the PS-b-PMMA based films (Table 1). The agreement between the calculated SSEF and the experimental data demonstrate that the film thickness can be accurately determined (*i.e.*, provides a result consistent with the profilometry measurements) when the Raman amplitude ratio is used to determine the polymer film's refractive index.

In order to demonstrate the applicability of the method with other mixed polymer compositions that have distinct Raman peaks for each component, two P2VN-b-PMMA films with different solution concentrations are measured. The relative Raman cross section between P2VN and PMMA is experimentally determined and calculated using

المنارة للاستشارات
www.manaraa.com

equation 1. The relative Raman cross section is then used to determine the Raman amplitude ratio (r_{P2VN}) for the P2VN-b-PMMA films (0.29 ± 0.01), which is similar to the manufacturer's reported 0.27 monomer fraction. The indices of refraction for the P2VN-b-PMMA films are determined using equation 5, and are shown in table 1.

$$\boldsymbol{RI_{film}} = (\boldsymbol{r_{P2VN}} \times \boldsymbol{RI_{P2VN}}) + ((\mathbf{1} - \boldsymbol{r_{P2VN}}) \times \boldsymbol{RI_{PMMA}}) \ (\mathbf{5})$$

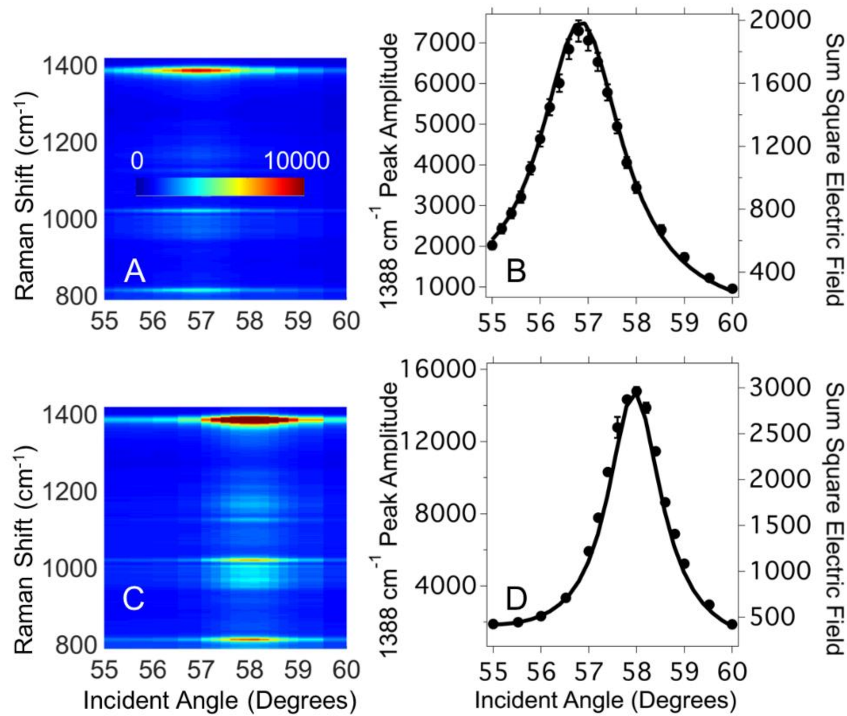

Figure 4: (A and C) SA Raman spectra of P2VN-b-PMMA films plotted on the same color amplitude scale showing 1388 and 812 cm^{-1} peaks of P2VN and PMMA, respectively. (B and D) 1388 cm^{-1} peak amplitude versus incident angle graph of the P2VN-b-PMMA films where the solid black line represents the SSEF fit to the experimental data (circles). (A and B) show the film formed by spin coating the 97.0 mg/mL solution and (C and D) show the film formed by spin coating the 133 mg/mL solution (as described in the Materials and Methods section).

المنارة للاستشارات
www.manaraa.com

Figure 4A and C show the SA Raman spectra collected at each incident angle from 55° to 60°. The 1388 cm^{-1} peak corresponds to P2VN and 812 cm^{-1} peak corresponds to PMMA. The P2VN peak is more intense compared to the PMMA peak due to the larger Raman cross section. Figure 4B and D show the 1388 cm^{-1} peak amplitude versus incident angle graph extracted from the data in Figure 4A and C. There is a shift in the waveguide mode location and fwhm when comparing the P2VN peak from the two films. The 97.0 mg/mL solution forms a 795 ± 6 nm thick film (Table 1) with a waveguide mode at 56.85º ± 0.01º and a fwhm of 2.10 º ± 0.03 º (Table 2). The waveguide mode location shifts to a higher angle (57.95º ± 0.01º) and with a smaller fwhm (1.51º ± 0.03º) for the film prepared from the high concentration solution due to the resulting thicker film (971 ± 8 nm). The differences in the SA Raman data for the two P2VN-b-PMMA films is due only to the change in the thickness since both films have the same Raman amplitude ratio (r_{P2VN}) and refractive index. There is a 0.6% and 2% difference between the thicknesses determined by SA Raman and profilometry (Table 1) for the respective films.

Conclusion

For PS-b-PMMA, PS-b-PMMA:PMMA, and P2VN-b-PMMA films with unknown refractive index and thickness, both parameters can be extracted from the SA Raman data set. The refractive index is calculated from the fractional composition as measured by the SA Raman peak amplitude ratio and the known refractive index of the homopolymers. The thickness is extracted from fitting the 1001 cm^{-1} PS or 1388 cm^{-1} P2VN peak amplitude versus incident angle using the determined refractive index and SSEF calculations. This measurement does not require an external probe (as required for

المنارة للاستشارات
www.manaraa.com

the fluorescence analysis) and is not destructive (in contrast to the profilometry measurement). A "real" application of the SA Raman method will neither require the use of a fluorescent marker nor profilometry and is thus nondestructive and requires little sample preparation. This technique provides thicknesses for films with an average 5% difference between profilometry, and on polymer films that are generally too thin for traditional Raman spectroscopy, as well as other optical thickness measurements. PS-b-PMMA, PS-b-PMMA:PMMA, and P2VN-b-PMMA films were used to demonstrate the method, which will be fully compatible with a range of other mixed polymer systems. SA Raman spectroscopy will be useful whenever the components have distinguishable Raman peaks for measuring films used in energy capture and conversion devices, monitoring films prepared for microelectronics and optics, and biomedical applications.

Acknowledgement

This research was supported by the U.S. Department of Energy (DOE), Office of Science, Basic Energy Sciences, Chemical Sciences, Geosciences, and Biosciences Division. The research was performed at the Ames Laboratory, which is operated for the U.S. DOE by Iowa State University under contract # DE-AC02-07CH11358.

References

(1) Lin, Y.; Zhao, F.; He, Q.; Huo, L.; Wu, Y.; Parker, T. C.; Ma, W.; Sun, Y.; Wang, C.; Zhu, D.; Heeger, A. J.; Marder, S. R.; Zhan, X. *JACS* **2016**, *138*, 4955-4961.

(2) He, Z.; Xiao, B.; Liu, F.; Wu, H.; Yang, Y.; Xiao, S.; Wang, C.; Russell, T. P.; Cao, Y. *Nat Photon* **2015**, *9*, 174-179.

المنارة للاستشارات
www.manaraa.com

(3) Mori, D.; Benten, H.; Okada, I.; Ohkita, H.; Ito, S. *Energy & Environmental Science* **2014**, *7*, 2939-2943.

(4) Paterson, A. F.; Treat, N. D.; Zhang, W.; Fei, Z.; Wyatt-Moon, G.; Faber, H.; Vourlias, G.; Patsalas, P. A.; Solomeshch, O.; Tessler, N.; Heeney, M.; Anthopoulos, T. D. *Adv. Mater.* **2016**, *28*, 7791-7798.

(5) Landi, G.; Altavilla, C.; Ciambelli, P.; Neitzert, H. C.; Iannace, S.; Sorrentino, A. *AIP Conference Proceedings* **2015**, *1695*, 020044.

(6) Wang, X.; Lee, W. H.; Zhang, G.; Wang, X.; Kang, B.; Lu, H.; Qiu, L.; Cho, K. *Journal of Materials Chemistry C* **2013**, *1*, 3989-3998.

(7) Rezem, M.; Kelb, C.; Günther, A.; Rahlves, M.; Reithmeier, E.; Roth, B., 2016, pp 975112-975116.

(8) Fujii, R.; Guo, J.; Klepp, J.; Pruner, C.; Fally, M.; Tomita, Y. *Opt. Lett.* **2014**, *39*, 3453-3456.

(9) Ladj, R.; Bitar, A.; Eissa, M. M.; Fessi, H.; Mugnier, Y.; Le Dantec, R.; Elaissari, A. *Int. J. Pharm.* **2013**, *458*, 230-241.

(10) Guo, B.; Glavas, L.; Albertsson, A.-C. *Prog. Polym. Sci.* **2013**, *38*, 1263-1286.

(11) Ng, A.; Li, C. H.; Fung, M. K.; Djurišić, A. B.; Zapien, J. A.; Chan, W. K.; Cheung, K. Y.; Wong, W.-Y. *The Journal of Physical Chemistry C* **2010**, *114*, 15094-15101.

(12) Hilfiker, J. N.; Stadermann, M.; Sun, J.; Tiwald, T.; Hale, J. S.; Miller, P. E.; Aracne-Ruddle, C. *Appl. Surf. Sci.* **2016**, http://dx.doi.org/10.1016/j.apsusc.2016.08.131

(13) Bobbitt, J. M.; Weibel, S. C.; Elshobaki, M.; Chaudhary, S.; Smith, E. A. *Anal. Chem.* **2014**, *86*, 11957-11961.

المنارة للاستشارات
www.manaraa.com

(14) Zhong, Y.; Suzuki, K.; Inoue, D.; Hashizume, D.; Izawa, S.; Hashimoto, K.; Koganezawa, T.; Tajima, K. *Journal of Materials Chemistry A* **2016**, *4*, 3335-3341.

(15) Rohini, R.; Bose, S. *ACS applied materials & interfaces* **2014**, *6*, 11302-11310.

(16) Cha, K. J.; Lih, E.; Choi, J.; Joung, Y. K.; Ahn, D. J.; Han, D. K. *Macromolecular bioscience* **2014**, *14*, 667-678.

(17) Lindqvist, C.; Sanz-Velasco, A.; Wang, E.; Bäcke, O.; Gustafsson, S.; Olsson, E.; Andersson, M. R.; Müller, C. *Journal of Materials Chemistry A* **2013**, *1*, 7174-7180.

(18) Lee, J.; Kang, M. H.; Lim, W. C.; Shin, K.; Lee, Y. *Surf. Interface Anal.* **2013**, *45*, 498-502.

(19) Lee, Y.; Lee, J.; Lim, W. C.; Shin, K.; Kim, K.-J. *Surf. Interface Anal.* **2011**, *43*, 277-280.

(20) Tran, W.; Tisinger, L. G.; Lavalle, L. E.; Sommer, A. J. *Appl. Spectrosc.* **2015**, *69*, 230-238.

(21) Nikonenko, N.; Tretinnikov, O. *J. Appl. Spectrosc.* **2008**, *75*, 878-882.

(22) Yang, P.; Meng, X.; Zhang, Z.; Jing, B.; Yuan, J.; Yang, W. *Anal. Chem.* **2005**, *77*, 1068-1074.

(23) Chan, K. L. A.; Kazarian, S. G. *Appl. Spectrosc.* **2003**, *57*, 381-389.

(24) Matthew, W. M.; Vy, H. T. N.; Emily, A. S. *Vib. Spectrosc* **2013**, *65*, 95-100.

(25) Damin, C. A.; Nguyen, V. H.; Niyibizi, A. S.; Smith, E. A. *Analyst* **2015**, *140*, 1955-1964.

(26) Meyer, M. W.; Larson, K. L.; Mahadevapuram, R. C.; Lesoine, M. D.; Carr, J. A.; Chaudhary, S.; Smith, E. A. *ACS applied materials & interfaces* **2013**, *5*, 8686-8693.

المنارة للاستشارات
www.manaraa.com

(27) Tsai, H.; Pitera, J. W.; Miyazoe, H.; Bangsaruntip, S.; Engelmann, S. U.; Liu, C.-C.; Cheng, J. Y.; Bucchignano, J. J.; Klaus, D. P.; Joseph, E. A.; Sanders, D. P.; Colburn, M. E.; Guillorn, M. A. *ACS Nano* **2014**, *8*, 5227-5232.

(28) Osinkina, L.; Lohmüller, T.; Jäckel, F.; Feldmann, J. *The Journal of Physical Chemistry C* **2013**, *117*, 22198-22202.

(29) Albrecht, T. R.; Bedau, D.; Dobisz, E.; He, G.; Grobis, M.; Hellwig, O.; Kercher, D.; Lille, J.; Marinero, E.; Patel, K.; Ruiz, R.; Schabes, M. E.; Lei, W.; Weller, D.; Tsai-Wei, W. *Magnetics, IEEE Transactions on* **2013**, *49*, 773-778.

(30) Cho, W. J.; Kim, Y.; Kim, J. K. *ACS Nano* **2011**, *6*, 249-255.

(31) Jung, Y. S.; Lee, J. H.; Lee, J. Y.; Ross, C. A. *Nano Lett.* **2010**, *10*, 3722-3726.

(32) Schneider, G. F.; Calado, V. E.; Zandbergen, H.; Vandersypen, L. M. K.; Dekker, C. *Nano Lett.* **2010**, *10*, 1912-1916.

(33) McKee, K.; Smith, E. *The Review of scientific instruments* **2010**, *81*, 43106.

(34) Kasarova, S. N.; Sultanova, N. G.; Ivanov, C. D.; Nikolov, I. D. *Opt. Mater.* **2007**, *29*, 1481-1490.

(35) Bass, M.; DeCusatis, C.; Enoch, J.; Lakshminarayanan, V.; Li, G.; MacDonald, C.; Mahajan, V.; Van Stryland, E. *Handbook of Optics, Third Edition Volume IV: Optical Properties of Materials, Nonlinear Optics, Quantum Optics (set)*; Mcgraw-hill, 2009.

(36) Sultanova, N.; Kasarova, S.; Nikolov, I. *Acta Physica Polonica-Series A General Physics* **2009**, *116*, 585.

(37) Lesoine, M. D.; Bobbitt, J. M.; Zhu, S.; Fang, N.; Smith, E. A. *Anal. Chim. Acta* **2014**, *848*, 61-66.

المنارة للاستشارات

www.manaraa.com

Supporting Information

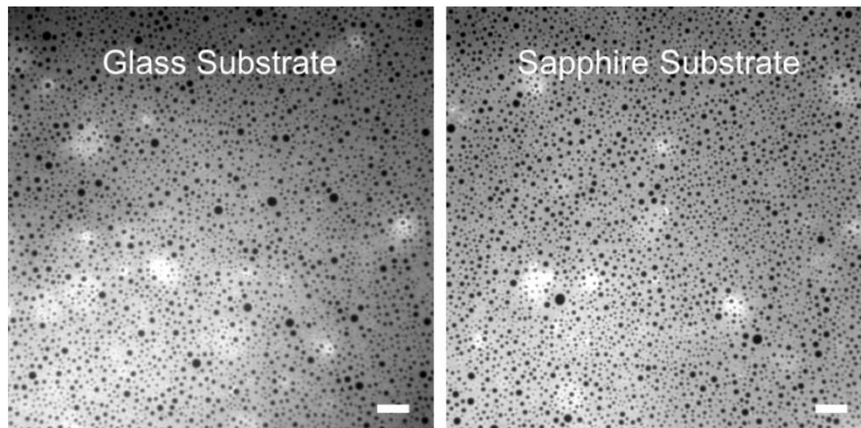

Figure S1: Fluorescence images of a Rhodamine 6G-labeled 1:2 PS-b-PMMA:PMMA film on (**left**) glass and **(right**) after wedge transfer to a sapphire substrate. The morphology and size of PS-rich areas are not affected after transferring to a sapphire substrate. The fluorescence images are on the same intensity scale and were collected with a 20× objective. The scale bar is 51 μm.

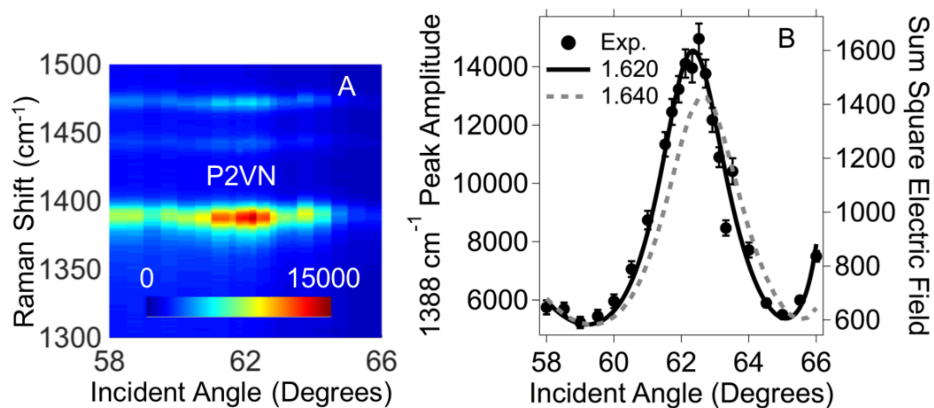

Figure S2: P2VN's refractive index at 785-nm is not known in literature, so SA Raman spectroscopy is used to measure a 1.4 ± 0.1 μm P2VN (homopolymer) film to determine the refractive index. **(A)** SA Raman Spectra showing the 1388 cm^{-1} peak of a P2VN homopolymer film with a thickness of 1.4 ± 0.1 μm. The thickness was measured by

www.manaraa.com

profilometry after the SA Raman measurements were complete. **(B)** The plot of the 1388 cm^{-1} peak amplitude versus incident angle shows the measured waveguide mode that is used to determine the refractive index (1.620, black line) of P2VN at 785-nm excitation wavelength using SSEF calculations. The refractive index, an input parameter in the SSEF calculations, is varied until the residual between the experimental data and the SSEF calculation is below an average of 10%. The data does not fit to a higher or lower index of refraction value (e.g., 1.640 shown with the gray line).

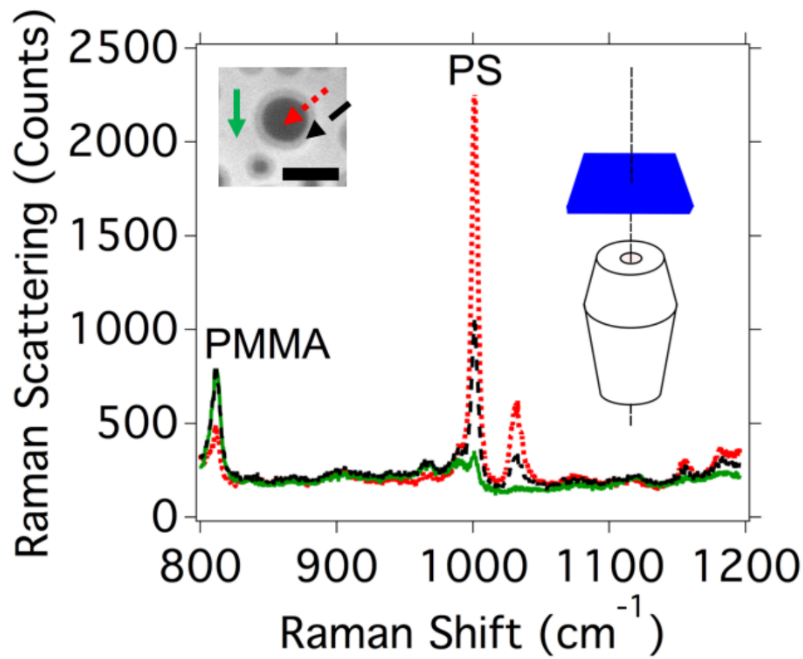

Figure S3: Raman spectra collected at various locations in the 1:2 PS-b-PMMA:PMMA film. The left inset is the fluorescence image of 1:2 PS-b-PMMA:PMMA film. The color is matched between the arrow in the inset and the spectrum. A schematic of the epi-illumination instrument is shown in the right inset where the objective is used to focus the laser and collect the Raman signal. The scale bar is 9 μm. The laser spot size for these measurements is 1.4 ± 0.2 μm, which is significantly smaller than the analyzed

المنارة للاستشارات
www.manaraa.com

8.2 ± 0.3 μm domain; the high and low fluorescence areas can be independently measured.

The **green spectrum** is collected from an area of high fluorescence intensity, and has an intense PMMA carbonyl stretching vibration peak at 812 cm^{-1}. The region with higher fluorescence intensity also has a 1001 cm^{-1} peak, assigned to the ring breathing mode of PS. The PMMA-rich area also contains 8.6 ± 0.2% PS as calculated by converting the ratio from equation 2 into a percentage. The **red spectrum** was collected from a region of the sample with low fluorescence intensity, and is shown to be a PS-rich area with an intense PS peak at 1001 cm^{-1}. The lower fluorescence intensity region also has a PMMA peak at 812 cm^{-1}. There is 32.9 ± 0.3% of PMMA in the PS-rich areas as calculated as calculated by converting the ratio from equation 3 into a percentage. There is also a third region (Figure S3 black spectrum) of intermediate PS and PMMA compositions that occupies a smaller area than the PS-rich and PMMA-rich areas. The Raman peak amplitudes can be used to provide quantitative information on the fractional composition of the films provided the relative Raman cross-section ratio is known.

المنارة للاستشارات
www.manaraa.com

CHAPTER 4

EXTRACTING INTERFACE LOCATIONS IN MULTILAYER POLYMER WAVEGUIDE FILMS USING SCANNING ANGLE RAMAN SPECTROSCOPY

Jonathan M. Bobbitt and Emily A. Smith

The Ames Laboratory, U.S. Department of Energy, and Department of Chemistry, Iowa State University, Ames, IA 50011, United States

Abstract

There is an increasing demand for nondestructive *in situ* techniques that measure chemical content, total thickness, and interface locations for multilayer polymer films, and SA Raman spectroscopy in combination with appropriate data models can provide this information. A scanning angle (SA) Raman spectroscopy method was developed to measure the chemical composition of multilayer polymer waveguide films and to extract the location of buried interfaces between polymer layers with 7–80-nm axial spatial resolution. The SA Raman method measures Raman spectra as the incident angle of light upon a prism-coupled thin film is scanned. Six multilayer films consisting of poly(methyl methacrylate)/polystyrene or poly(methyl methacrylate)/polystyrene/poly(methyl methacrylate) were prepared with total thicknesses ranging from 330-1260 nm. The interface locations were varied by altering the individual layer thicknesses between 140-680 nm. The Raman amplitude ratio of the 1605 cm^{-1} peak for PS and 812 cm^{-1} peak for PMMA was used in calculations of the electric field intensity within the polymer layers

www.manaraa.com

to model the SA Raman data and extract the total thickness and interface locations. There is an average 8% and 7% difference in the measured thickness between the SA Raman and profilometry measurements for bilayer and trilayer films, respectively.

Introduction

Polymer-polymer interface characterization in multilayer polymer films is important for their increasing use in energy storage and capture devices,[1-11] coatings and optics,[12-15] food packaging,[16-18] and biomedical applications.[19] Work on understanding polymer-polymer interface surface mixing,[20] roughness,[21] and stability[22,23] is a focus of many multilayer polymer film studies. As important is characterizing the chemical composition, thickness, and interface locations when creating and optimizing new multilayer polymer devices. Optical-based spectroscopies are well suited for *in situ* nondestructive measurements of polymer films.

Infrared variable angle spectroscopic ellipsometry (IR-VASE) is a technique that is capable of providing multilayer polymer interface and chemical content information.[24] Good signal-to-noise ratio IR-VASE spectra require 8-12 hour collection times for a single multilayer polymer film, which limits the real-time analysis of samples. Infrared spectroscopy operated in attenuated total reflection mode is well suited for monitoring chemical content information during the layer-by-layer formation of polyelectrolyte multilayer films.[25-27] Extracting thicknesses and buried interface locations from the spectra, however, is complicated due to the penetration depth of evanescent waves varying across the infrared spectrum.

المنارة للاستشارات

www.manaraa.com

Raman spectroscopy provides chemical content information using a single excitation wavelength. Micro-Raman spectroscopy with epi-illumination can provide chemical content information for thin multilayer polymer films, but does not provide buried interface locations from polymer films under approximately 2 μm.[28-30] Scanning angle (SA) Raman spectroscopy is a technique that couples a sample to a prism (a schematic is shown in the top of Fig. 1), and generates a data set consisting of the Raman spectra as a function of the incident angle of the excitation light. SA Raman spectroscopy has been used to measure polymer waveguide thicknesses, buried bilayer film interfaces, and mixed polymer film chemical composition.[31-34] Other reported methods that are similar to SA Raman spectroscopy, variable-angle internal-reflection and attenuated total reflection Raman spectroscopy, have been used to measure bilayer polymer films.[35,36] These studies focused on micrometers to hundreds of micrometers thick bilayer films, the reported methods cannot be easily applied to other polymer systems or, in the work by Fumihiko *et al.*, no buried interface location was extracted.

Summarized here is a nondestructive method that combines SA Raman spectroscopy and electric field calculations to extract total thickness and interface locations for thin bilayer and trilayer polymer waveguide films. Polymer films behave as a waveguide when the thickness is greater than approximately $\frac{\lambda}{2\eta}$, where λ is the excitation wavelength and η is the refractive index of the polymer at the excitation wavelength. When light is coupled into the waveguide through a prism, constructive interference occurs at discrete incident angles (referred to as waveguide mode angles), which produces an enhancement in the Raman signal collected at these angles. Previous work by Meyer *et al.*, used electric field calculations to model SA Raman spectra of homopolymer waveguides of varying

المنارة للاستشارات
www.manaraa.com

thicknesses.[31] Raman scattering is proportional to the square of the electric field, so SA Raman spectra are modeled by plotting the square of the electric field intensity integrated over the thickness of each polymer layer (*i.e.,* SSEF) as a function of the incident angle. The current work expands the bilayer polymer film work reported by Damin *et al.*[33] in two important ways. First, we apply the SA Raman amplitude ratio between peaks for each polymer in the film, which has been previously proposed by us to measure mixed polymer films,[34] and recursive SSEF calculations to reduce the computational time required to model the SA Raman data. Second, total film thickness and interface locations for bilayer and trilayer polymer films with distinctly different indices of refraction are reported. This new method significantly reduces analysis time and is demonstrated on thin (< 1.3 µm) bilayer poly(methyl methacrylate)/polystyrene (PMMA/PS) and trilayer (PMMA/PS/PMMA) waveguide films with one or two buried interfaces, respectively. The presented method should be applicable to measure numerous polymer multilayer films whenever the layers have at least one distinct Raman peak.

Experimental

Sample preparation

A 31.3 mg/mL PS (192,000 g/mol, Sigma Aldrich, St. Louis, MO), 39.0 mg/mL PMMA (120,000 g/mol, Sigma Aldrich, St. Louis, MO), 55.3 mg/mL PMMA, and 67.9 mg/mL PMMA solutions were prepared from 120 mg/mL stock solutions in toluene (Fisher Scientific, Waltham, MA). The PMMA solutions of varying concentration were used to fabricate PMMA layers with different thicknesses and to change the interface location(s) in the multilayer films. PS and PMMA films were prepared by spin coating 200 µL of solution with a KW-4A spin coater (Chemat Technology, Northridge, CA) at

المنارة للاستشارات
www.manaraa.com

3000 rpm for 60 seconds. Glass cover slips (25 mm^2 area, Corning Inc., Corning, NY) and sapphire disks (507 mm^2 area, Meller Optics, Providence, RI) were used as substrates, and the film's total and individual layer thicknesses were measured on an AlphaStep® D-600 stylus profiler (KLA Tencor, Milpitas, CA).

Multilayer films were prepared by using the wedge transfer method.[37] A PS film was lifted off of the sapphire disk and floated at the water-air interface using a beaker of water. The PS film was deposited over a PMMA film and the bilayer was dried at 70 °C for 10 minutes. The bilayer film was then left in a petri dish for 24 hours at room temperature to ensure all the residual water had evaporated. After the PMMA/PS bilayer SA Raman measurements were completed, a second PMMA film was lifted off a sapphire disk using a beaker of water and the second PMMA film was placed on top of the bilayer film to create a PMMA/PS/PMMA trilayer film. The drying process was repeated for the trilayer samples.

Scanning angle Raman measurements

A home-built instrument, previously reported by Lesoine *et al.*, was used to collect SA Raman spectra.[38] A 532-nm excitation source (Coherent, Santa Clara, CA) set to s-polarized light was directed onto a sapphire prism (ISP Optics, Irvington, NY) by coupling the source into a polarization maintaining single mode fiber (Thorlabs, Newton, NJ). The incident angle was controlled by using a rotational stage (Zaber Technologies, Vancouver, British Columbia, Canada), which had the fiber mounted on it with a 28-mW laser output. The SA Raman data were collected over an angle range of 48.0-62.0° with a 0.2° step size. A 0.25 numerical aperture 10× microscope objective (Leica, Wetzlar, Germany) was used to direct the collected SA Raman signal into an optical microscope

المنارة للاستشارات
www.manaraa.com

(Leica, Wetzlar, Germany). The light was focused onto a HoloSpec $f/1.8$i spectrograph (Kaiser Optical Systems, Ann Arbor, MI) that was attached to the side port of the optical microscope. A Newton 940 charged coupled device (Andor Technology, Belfast, UK) with 2048 × 512 pixels was used to collect the SA Raman spectra for 60s with two replicate measurements at each angle.

Igor Pro 6.36 scientific analysis and graphing software was used to process all SA Raman spectra. A Gaussian function with a linear baseline was used to batch fit and extract the amplitudes of PS and PMMA peaks at 1605 and 812 cm^{-1}, respectively. SA Raman spectra were plotted as a function of their incident angle using Matlab 2016b. The SA Raman amplitude ratio (r_{PS}) was calculated at each incident angle using equation 1, where *I* represents the peak amplitude at the designated wavenumber for the indicated polymer and σ_R is the relative Raman cross-section (defined in equation 2).

$$\boldsymbol{r_{PS} = \frac{I_{PS,.1605\ cm^{-1}}}{I_{PS,1605\ cm^{-1}} + (I_{PMMA,812\ cm^{-1}} \times \sigma_R)}} \quad (1)$$

$$\boldsymbol{\sigma_R = \frac{I_{PS,1605\ cm^{-1}}}{I_{PMMA,812\ cm^{-1}}} = 1.0} \quad (2)$$

The relative Raman cross-section (σ_R) was determined using epi-illumination with a 532-nm excitation source on a XploRA Plus confocal Raman microscope (Horiba Scientific, Edison, NJ). The samples used to determine σ_R were prepared and characterized as previously reported.[34] The thickness of the samples ensured that the Raman signal was independent of the optical focus (*i.e.*, the same amount of polymer was

المنارة للاستشارات
www.manaraa.com

measured regardless of the focus). Spectra were acquired for 5s with 2 accumulations from 3 separate locations.

Electric field and sum square electric field (SSEF) calculations

Electric field intensity calculations were performed using finite-difference time-domain simulations (EM Explorer, San Francisco, CA). The refractive indices of each polymer layer and the SA Raman amplitude ratio (r_{PS}) were input parameters needed in the calculation to find the thickness of each layer. The refractive index for 532-nm and s-polarized light was 1.764 for sapphire, 1.495 for PMMA, and 1.598 for PS.[39-41] A recursive script (included in the supplemental information) for the finite-difference time-domain calculations varied the total thickness (10-nm step size) over the range shown in Table 1. For a given total thickness, the fractional composition of each polymer was modeled by the SA Raman amplitude ratio (r_{PS}), which was varied in increments of 0.05 over the range of values listed in Table 1. (The range of values in Table 1 represent the experimentally measured range across all incident angles). While the SA Raman amplitude ratio does not match the film composition, as discussed below, over the waveguide mode angle range it can be used to approximate the composition and minimize the computation time required to fit the data. Because the SA Raman amplitude ratio (r_{PS}) range varied for each sample (Table 1), the step size for the thickness of each layer also varied with each sample.

المنارة للاستشارات

www.manaraa.com

Table 1: The experimental SA Raman amplitude ratios (r_{PS}) and interface locations determined by SA Raman spectroscopy.

Sample	Total Thickness Range Used in Calculation (nm)	Measured SA Raman Amplitude Ratio (r_{PS}) Range Used in Calculation	Measured Interface 1 (nm)	Measured Interface 2 (nm)
1-Bi	300-360	0.4-0.8	140 ± 10	NA
2-Bi	420-480	0.3-0.7	296 ± 7	NA
3-Bi	600-660	0.2-0.6	440 ± 10	NA
1-Tri	740-800	0.1-0.3	160 ± 30	340 ± 40
2-Tri	740-800	0.08-0.23	300 ± 30	480 ± 40
3-Tri	1230-1290	0.12-0.22	350 ± 60	580 ± 80

The electric field intensity was calculated over an incident angle range of 48.0-62.0° with a 0.2° step size unless otherwise noted. A 12-nm Yee cell size was used for all calculations. The SSEF was determined by integrating the electric field intensity across the entire thickness of the individual polymer layers. The standard error of the estimate (s_{est}), the square root of the average across all angles squared deviation of the experimental data from the SSEF fit, was calculated for each SSEF fit. The lowest s_{est} value provided the best fit between the experimental data and the SSEF fit. For each polymer film, a SSEF fit was individually determined for the PS and PMMA waveguide modes to determine total thickness and interface location(s). Then the average of the PS and PMMA values were calculated. The reported uncertainties in the total thickness and interface location(s) were determined by finding the second-best SSEF fit (the second lowest s_{est}) that is shifted by at least 0.2°, the angular resolution for these measurements,

المنارة للاستشارات
www.manaraa.com

from the best fit to the experimental data. The waveguide mode maximum angle for PS and PMMA was determined by fitting the SSEF fit to a Lorentzian function and the standard deviation was determined from the Igor Pro fitting software.

Results and Discussion

Motivation for determining buried interfaces using SA Raman spectroscopy

Understanding how the electric field varies across the thickness of a bilayer or trilayer film, as well as with incident angle, is important for understanding the collected SA Raman signal since the electric field intensity is proportional to the Raman signal. The measured parameters in the SA Raman data (*e.g.*, peak intensities and waveguide mode angles) in combination with electric field calculations are used to extract interface locations from thin bilayer and trilayer polymer waveguide films.

The graphs of the electric field intensity across the polymer samples are shown in Fig. 1 for selected bilayer (left) and trilayer (right) films. Hereafter, samples will be referred to with a sample number (1, 2, or 3) and -Bi (for bilayer) or -Tri (for trilayer) films. The electric field profiles shown in Fig. 1 are calculated using the experimentally measured polymer thicknesses for four samples: 1-Bi (Fig. 1A), 2-Bi (Fig. 1B), 1-Tri (Fig. 1C), and 2-Tri (Fig. 1D). All bilayer and trilayer samples are thick enough (≥167 nm) to behave as a waveguide using 532-nm excitation, and clearly show angle-dependent electric field intensities as expected. Sample 1-Bi has 140 nm of PMMA and 180 nm of PS. Across the angle range of 48.0-62.0° a single waveguide mode is evident, and the waveguide mode angles are at 54.90° and 55.50° for PS and PMMA, respectively. The electric field intensity is generated in both the PMMA and PS layers.

المنارة للاستشارات
www.manaraa.com

However, the electric field intensity distribution varies with the incident angle and does not match the 55% PS polymer composition at all incident angles. For example, 63% of the total electric field intensity is generated in the PS layer at the 54.90° PS waveguide mode angle.

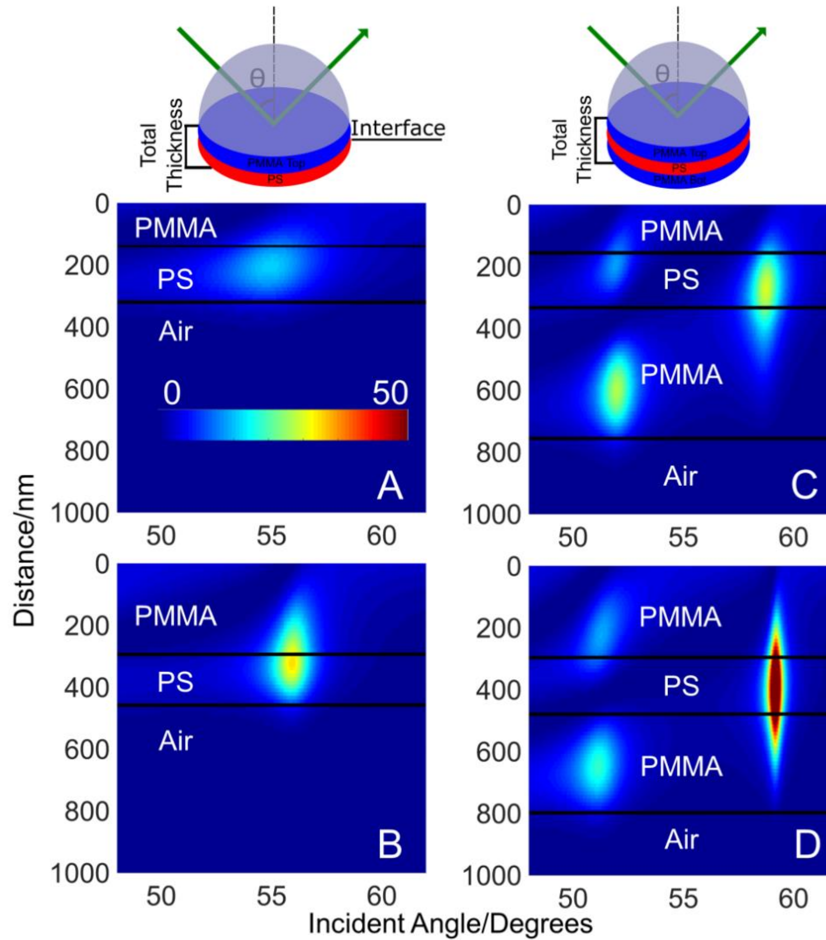

Figure 1: Calculated electric field intensity (square of the electric field) plots as a function of incident angle and distance from the prism/sample interface, which is located at 0 nm. The color scale represents the electric field intensity, and the scale in (A) is the same for all plots. The solid black lines indicate the interface between the polymer layers. The plots show where the electric field intensity is generated within the polymer films as

المنارة للاستشارات
www.manaraa.com

well as waveguide mode angles. (A) Sample 1-Bi: 140 nm PMMA, 180 nm PS; and (B) sample 2-Bi: 296 nm PMMA, 159 nm PS. (C) Sample 1-Tri: 160 nm top PMMA (closest to the prism), 420 nm bottom PMMA (farthest from the prism); and (D) Sample 2-Tri: 300 nm top PMMA, 310 nm bottom PMMA. The Sample 1-Tri and 2-Tri PS layer thickness is 180 nm. The calculations used a 0.05° step size.

Compared to sample 1-Bi, sample 2-Bi (Fig. 1B) shows an increase in the waveguide mode angle as the PMMA thickness increases to 296 nm and the PS layer thickness decreases to 159 nm. For both the PS and PMMA layers the waveguide mode angle occurs at 55.95°. With the increasing PMMA thickness for sample 2-Bi, there is a decrease in the electric field intensity generated in the PS layer down to 55% compared to the 63% generated in the PS layer for sample 1-Bi.

For the trilayer films shown in Fig. 1C and D, the PS thickness is constant at 180 nm. The total thickness is 770 (1-Tri) and 790 nm (2-Tri). Effectively, the PS layer is farther from the prism interface for sample 2-Tri as the thickness increases for the PMMA layer adjacent to the prism. The trilayer films are thick enough to generate two waveguide modes within this angle range, and they are termed mode zero (at high angles) and mode one (at low angles) as observed in Fig. 1C and D. Fig. S1 (Supporting Information) shows the plots of the calculated electric field intensity as a function of the distance from the prism/sample interface at the PMMA waveguide mode angle for sample 1-Tri, where the purple curve is waveguide mode one (51.95° incident angle) and the orange curve is waveguide mode zero (58.75° incident angle). Similar plots are

المنارة للاستشارات
www.manaraa.com

obtained at the PS waveguide mode angle. The graphs show that the distribution of the electric field intensity among the polymer layers varies with each waveguide mode.

In sample 1-Tri waveguide mode zero appears at 58.75° for both PS and PMMA layers, and waveguide mode one is at 51.85° for PS and 51.95° for PMMA. Compared to sample 1-Tri, sample 2-Tri waveguide mode zero for PS and PMMA shifts to a higher angle (59.15°), and waveguide mode one for PS and PMMA decreases by 0.95° and 0.85°, respectively. As the PS layer moves further away from the prism interface for sample 2-Tri, there is an 8% increase in the electric field intensity within the PS layer at waveguide mode zero, while there is a 1.5% decrease at waveguide mode one. Similar trends are observed for sample 3-Bi (Fig. S2A (Supporting Information)) and sample 3-Tri (Fig. S3A (Supporting Information)). These representative calculated results suggest it should be feasible to use SA Raman spectroscopy, with a signal that is proportional to the electric field intensity,[31-34,38,42-45] to measure total film thickness as well as the location of polymer interfaces for both bilayer and trilayer films.

Development of a SA Raman method with iterative fitting for analyzing bilayer polymer films

Fig. 2A shows the SA Raman spectra plotted over an incident angle range of 50.0-60.0° for sample 1-Bi, and Fig. 2B shows a plot of the peak amplitude as a function of incident angle for the PS (1001 cm^{-1}, red circles) and PMMA (812 cm^{-1}, blue circles) peaks. A single broad waveguide mode is measured for PS and PMMA, with waveguide mode angles at 54.86 ± 0.02° for PS and 55.58 ± 0.03° for PMMA. The PMMA amplitude at 812 cm^{-1} is 2.1× lower compared to the PS amplitude at 1605 cm^{-1}, which is not due to differences in their Raman cross-section ($\sigma_R = 1.0$) or the amount of PMMA

www.manaraa.com

in the film (there is only 1.2× less PMMA compared to PS in the sample). Rather, there is an enhancement in the PS signal in sample 1-Bi with the amplitude being 69% of the total signal collected. This agrees with the 63% value from the electric field calculations. Overall, the waveguide mode angles and peak amplitudes follow the trends observed in the electric field intensity plot shown in Fig. 1A.

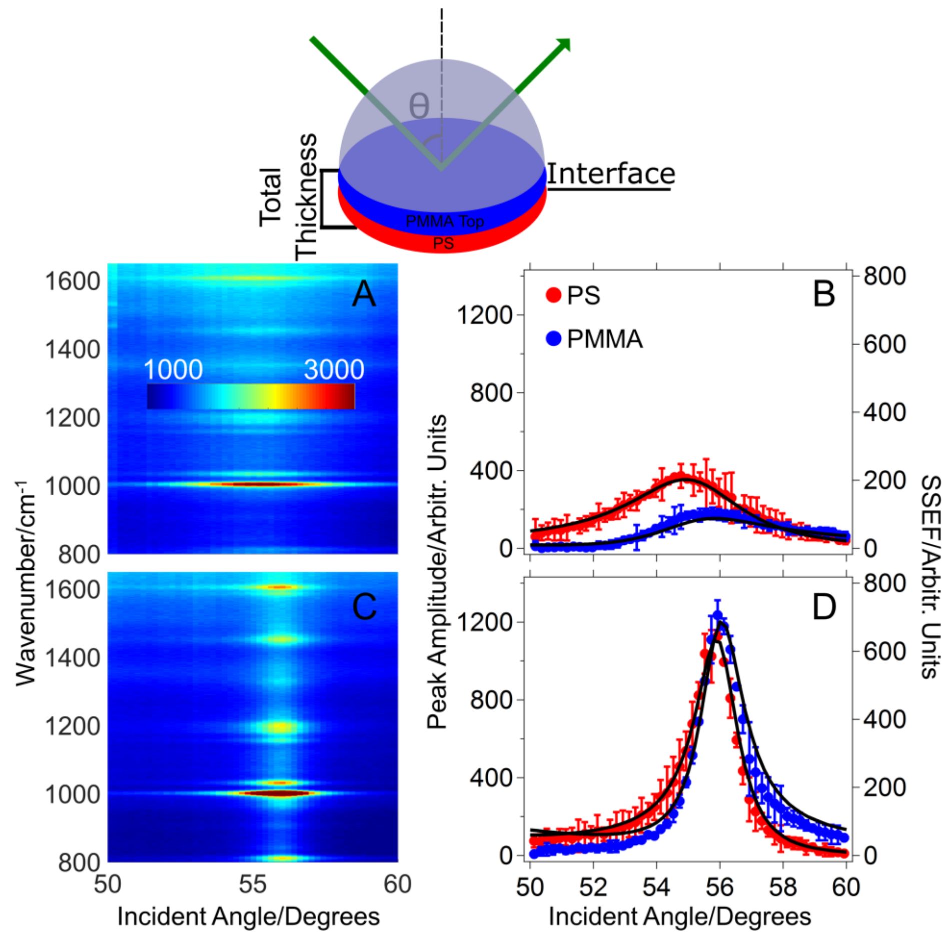

Figure 2: (A and C) SA Raman spectra of PMMA/PS bilayer films plotted on the same color scale shown in A. The color scale represents the SA Raman scattering intensity (Arbitr. Units). (B and D) show plots of the 1605 cm^{-1} PS and the 812 cm^{-1} PMMA peak amplitudes as a function of the incident angle. The black lines represent the

المنارة للاستشارات
www.manaraa.com

best SSEF fit to the experimental data. (A and B) correspond to sample 1-Bi and (C and D) correspond to sample 2-Bi.

SA Raman data for sample 2-Bi (Fig. 2C and D) and 3-Bi (Fig. S2B (Supporting Information)) show the effects of increasing the total thickness. Compared to sample 1-Bi, the PS and PMMA waveguide modes shift to higher angles. The peak amplitudes increase for sample 2-Bi and 3-Bi, and there is an overall decreasing trend in the magnitude of the SA Raman amplitude ratio (r_{PS}) as the PMMA layer thickness increases (Table 1). The SA Raman data are well fit by the iterative SSEF calculations (Fig. 2D and Fig. S2B (Supporting Information)).

Fig. 3 shows the thicknesses measured for each of the bilayer films by SA Raman spectroscopy and by profilometry. Overall, the SA Raman measurements properly capture the increasing PMMA layer thickness, and statistically similar PS thicknesses are measured for each of these samples. The interface locations determined by SA Raman spectroscopy (Table 1) are 140 ± 10 (sample 1-Bi), 296 ± 7 (sample 2-Bi), and 440 ± 10 nm (sample 3-Bi). The total thickness and PMMA layer thickness determined by the SA Raman method have an average 4% and 6% difference, respectively, compared to values measured by profilometry. The PS layer thickness has a larger 14% difference compared to the values measured by profilometry. The s_{est} is used to quantitatively determine how well the SSEF calculations fit the experimental SA Raman data. For sample 1-Bi the s_{est} for the best fit to the PS and PMMA data are determined to be 0.043 and 0.052, respectively. The s_{est} of the second-best fit that is shifted by at least 0.2° (the angular resolution of the experimental data) increases to 0.057 and 0.073 (33% and 40% increase)

المنارة للاستشارات
www.manaraa.com

when the total, PS, and PMMA layer thicknesses change by 10 nm as shown in Fig. S4 (Supporting Information). Increasing the angular resolution used to collect the experimental data and/or reducing the thickness increments used in the iterative calculations should improve the average percent difference between the SA Raman method and profilometry measurements at the cost of increased instrumental and computational time. It is also important to note that the samples measured by profilometry are not the same as those measured by the SA Raman method since profilometry is destructive and can only measure the individual layers prior to forming the bilayer.

للاستشارات المنارة

www.manaraa.com

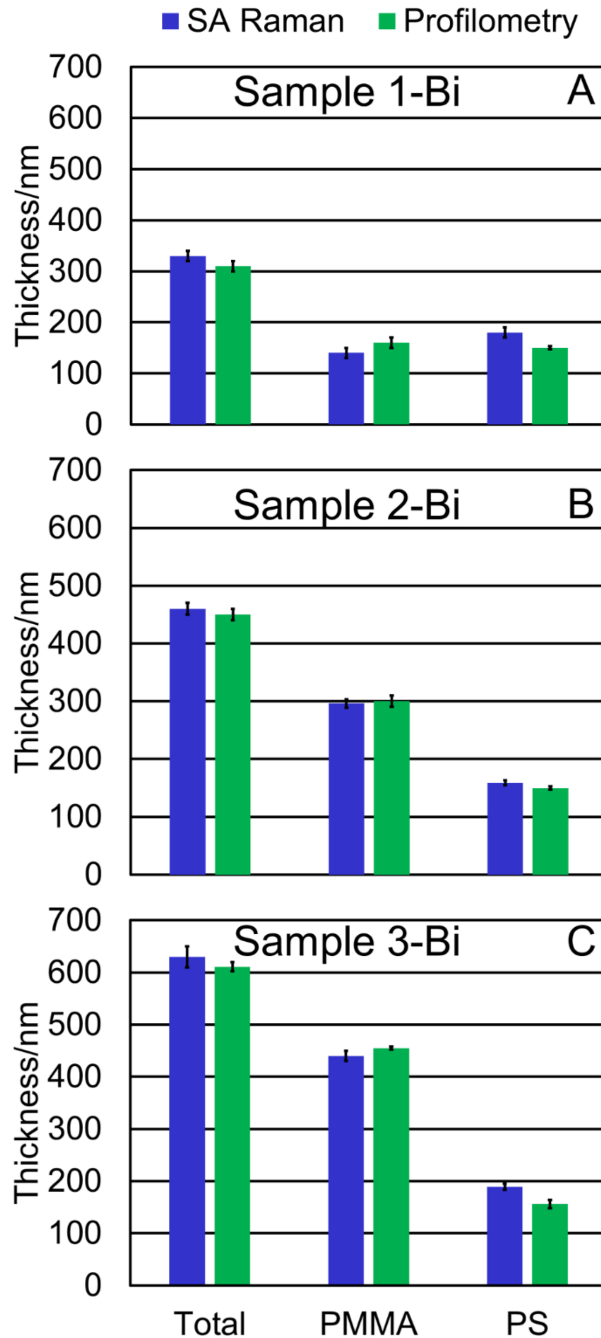

Figure 3: (A) Sample 1-Bi, (B) sample 2-Bi, and (C) sample 3-Bi thicknesses measured by the SA Raman method and profilometry. The profilometry measurements are performed on separate films fabricated with the same method used to prepare the samples measured by SA Raman spectroscopy, and assume the thicknesses measured on the

المنارة للاستشارات
www.manaraa.com

individual layers prior to forming the bilayer are retained in the bilayer. The error bars represent the difference between the best fit and the second-best fit that is shifted by at least 0.2° for two replicate measurements (SA Raman) and the standard deviation from three replicate measurements (profilometry).

Applying the SA Raman method for analysis of trilayer films

Trilayer films are prepared by transferring a third PMMA layer onto samples 1-Bi and 2-Bi. The corresponding multilayer films are samples 1-Tri and 2-Tri, and their SA Raman spectra are plotted in Fig. 4A and C. The SA Raman spectra for the trilayer films show similar trends to the electric field intensity plots (Fig. 1C and D). Waveguide mode one shifts by 0.9° to lower angles for both PS and PMMA in sample 2-Tri (Fig. 4D) when the PS layer moves farther from the sapphire prism interface. Data for a third trilayer sample (3-Tri) are shown in Fig. S3 (Supporting Information).

المنارة للاستشارات

www.manaraa.com

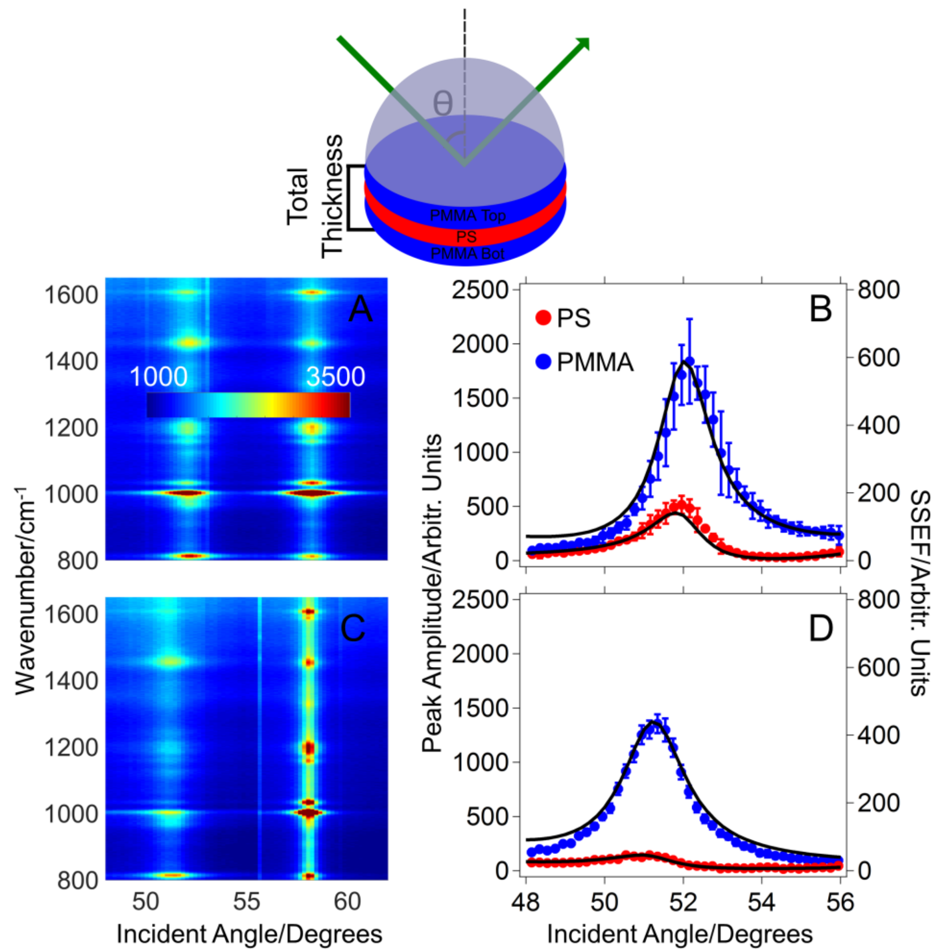

Figure 4: (A and C) SA Raman spectra of PMMA/PS/PMMA trilayer films plotted on the same color scale shown in A. The color scale represents the SA Raman scattering intensity (counts). (B and D) show the plots of waveguide mode one for 1605 cm^{-1} PS and the 812 cm^{-1} PMMA peak amplitudes versus incident angle. The black lines represent the best SSEF fit to the experimental data. (A and B) correspond to sample 1-Tri and (C and D) correspond to sample 2-Tri.

For the trilayer films, waveguide mode one is used to fit the data as better agreement with the profilometry measurement is obtained compared to using waveguide

المنارة للاستشارات
www.manaraa.com

mode zero. This is the result of the smaller angle shifts that occur in thicker films at waveguide mode zero (Fig. 1C and D), and the 0.2° angle resolution used to collect the experimental data. Considering the best instrumental angle resolution of 0.09° and a one micron thick film, the smallest thickness change that can be measured using waveguide mode one is approximately 6 nm. The smallest change in thickness that can be measured using waveguide mode zero is 35 nm since it requires a larger change in the thickness to observe a 0.09° angle shift.

For the trilayer films, the total thickness (1% average difference), top PMMA (6% average difference), PS (15% average difference), and bottom PMMA layer thicknesses (6% average difference) are comparable to the values measured by profilometry as shown in Fig. 5. The layer thicknesses can be used to calculate the two interface locations (Table 1). Since sample 1-Tri and 2-Tri are made by adding a third layer to sample 1-Bi and 2-Bi, the location of the first interface is the same. The location of this interface as measured by SA Raman spectroscopy is statistically similar for the bilayer and trilayer films.

المنارة للاستشارات

www.manaraa.com

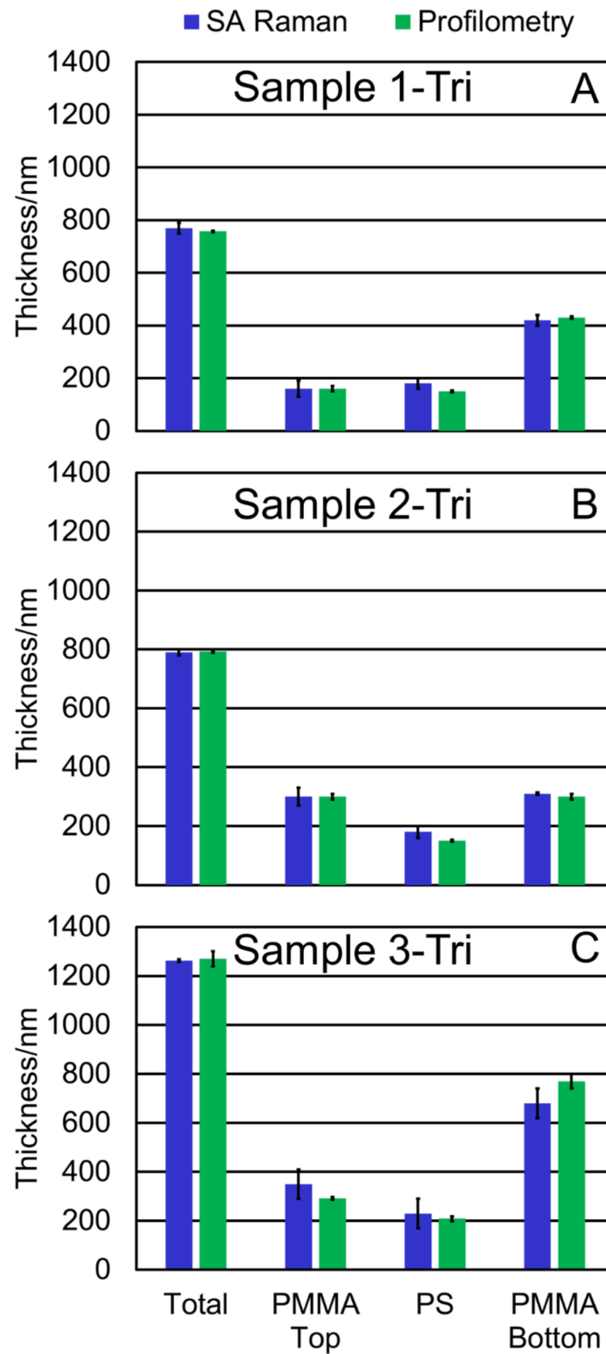

Figure 5: (A) Sample 1-Tri, (B) sample 2-Tri, and (C) sample 3-Tri thicknesses measured by the SA Raman method and profilometry. The profilometry measurements are performed on separate films fabricated with the same method used to prepare the samples measured by SA Raman spectroscopy, and assume the thicknesses measured on

www.manaraa.com

the individual layers prior to forming the trilayer are retained in the trilayer. The error bars represent the difference between the best fit and the second-best fit that is shifted by at least 0.2° (SA Raman) and the standard deviation from three replicate measurements (profilometry).

Conclusion

SA Raman spectroscopy of thin polymer films provides chemical content information about individual layers in intact films, is nondestructive, and requires minimal sample preparation. For PMMA/PS bilayer and PMMA/PS/PMMA trilayer waveguide films total thickness and interface locations are determined by fitting the 812 cm^{-1} PMMA and the 1605 cm^{-1} PS peak amplitude as a function of incident angle with the SSEF calculations. This technique provides chemical content information from multilayer polymer systems with total thicknesses and interface locations with an average 8% (bilayer) and 7% (trilayer) difference when compared to profilometry. This method can be easily applied to a variety of multilayer polymer systems provided each component has at least one distinct Raman peak and a known (or measurable) refractive index and Raman cross section at the excitation wavelength. The SA Raman spectroscopy method of analysis for multilayer polymer waveguide films will be useful for *in situ* measurements for samples ranging from tandem organic/inorganic hybrid energy storage and capture devices to multilayer plastic films used in packaging.

المنارة للاستشارات

www.manaraa.com

Acknowledgement

This research was supported by the U.S. Department of Energy, Office of Science, Basic Energy Sciences, Chemical Sciences, Geosciences, and Biosciences Division. The research was performed at Ames Laboratory, which is operated for the U.S. DOE by Iowa State University under contract # DE-AC02-07CH11358.

References

(1) Mwaura, J. K.; Pinto, M. R.; Witker, D.; Ananthakrishnan, N.; Schanze, K. S.; Reynolds, J. R. *Langmuir* **2005**, *21*, 10119-10126.

(2) Norrman, K.; Madsen, M. V.; Gevorgyan, S. A.; Krebs, F. C. *JACS* **2010**, *132*, 16883-16892.

(3) Fukuta, S.; Seo, J.; Lee, H.; Kim, H.; Kim, Y.; Ree, M.; Higashihara, T. *Macromolecules* **2017**, *50*, 891-899.

(4) Peumans, P.; Uchida, S.; Forrest, S. R. *Nature* **2003**, *425*, 158.

(5) Helgesen, M.; Sondergaard, R.; Krebs, F. C. *J. Mater. Chem.* **2010**, *20*, 36-60.

(6) Lim, I.; Bui, H. T.; Shrestha, N. K.; Lee, J. K.; Han, S.-H. *ACS Appl. Mater. Interfaces* **2016**, *8*, 8637-8643.

(7) Kim, J. Y.; Lee, K.; Coates, N. E.; Moses, D.; Nguyen, T.-Q.; Dante, M.; Heeger, A. J. *Science* **2007**, *317*, 222.

(8) Dou, L.; You, J.; Yang, J.; Chen, C.-C.; He, Y.; Murase, S.; Moriarty, T.; Emery, K.; Li, G.; Yang, Y. *Nat Photon* **2012**, *6*, 180-185.

المنارة للاستشارات

www.manaraa.com

(9) Shao, Z.; Chen, S.; Zhang, X.; Zhu, L.; Ye, J.; Dai, S. *J. Nanosci. Nanotechnol.* **2016**, *16*, 5611-5615.

(10) Fujinami, T.; Mehta, M. A.; Shibatani, M.; Kitagawa, H. *Solid state Ion.* **1996**, *92*, 165-169.

(11) Jenekhe, S. A.; Kiserow, D. J. *Chromogenic phenomena in polymers: tunable optical properties*; ACS Publications, 2004.

(12) Wu, Z.; Walish, J.; Nolte, A.; Zhai, L.; Cohen, R. E.; Rubner, M. F. *Adv. Mater.* **2006**, *18*, 2699-2702.

(13) Komikado, T.; Inoue, A.; Masuda, K.; Ando, T.; Umegaki, S. *Thin Solid Films* **2007**, *515*, 3887-3892.

(14) Lee, H.; Alcaraz, M. L.; Rubner, M. F.; Cohen, R. E. *ACS Nano* **2013**, *7*, 2172-2185.

(15) Chen, C.-T.; Tsai, T.-W. *Sens. Actuators A Phys.* **2016**, *244*, 252-260.

(16) Canellas, E.; Aznar, M.; Nerin, C.; Mercea, P. *J. Mater. Chem.* **2010**, *20*, 5100-5109.

(17) Alix, S.; Mahieu, A.; Terrie, C.; Soulestin, J.; Gerault, E.; Feuilloley, M. G. J.; Gattin, R.; Edon, V.; Ait-Younes, T.; Leblanc, N. *Eur. Polym. J.* **2013**, *49*, 1234-1242.

(18) Siracusa, V.; Ingrao, C.; Lo Giudice, A.; Mbohwa, C.; Dalla Rosa, M. *Food Res. Int.* **2014**, *62*, 151-161.

(19) Such, G. K.; Johnston, A. P. R.; Caruso, F. *Chem. Soc. Rev.* **2011**, *40*, 19-29.

(20) Lee, W.-K.; Ryou, J.-H.; Cho, W.-J.; Ha, C.-S. *Polym. Test.* **1998**, *17*, 167-177.

(21) Müller-Buschbaum, P.; Gutmann, J. S.; Kraus, J.; Walter, H.; Stamm, M. *Macromolecules* **2000**, *33*, 569-576.

(22) Zhang, Z.; Ahn, D. U.; Ding, Y. *Macromolecules* **2012**, *45*, 1972-1981.

(23) Yang, Q.; Zhu, Y.; You, J.; Li, Y. *Colloid. Polym. Sci.* **2017**, *295*, 181-188.

المنارة للاستشارات

www.manaraa.com

(24) Kang, S.; Prabhu, V. M.; Soles, C. L.; Lin, E. K.; Wu, W.-l. *Macromolecules* **2009**, *42*, 5296-5302.

(25) Erel-Unal, I.; Sukhishvili, S. A. *Macromolecules* **2008**, *41*, 8737-8744.

(26) Owusu-Nkwantabisah, S.; Gammana, M.; Tripp, C. P. *Langmuir* **2014**, *30*, 11696-11703.

(27) Ho, T. T. M.; Bremmell, K. E.; Krasowska, M.; MacWilliams, S. V.; Richard, C. J. E.; Stringer, D. N.; Beattie, D. A. *Langmuir* **2015**, *31*, 11249-11259.

(28) Jawhari, T.; Pastor, J. *J. Mol. Struct.* **1992**, *266*, 205-210.

(29) Qin, S.; Qin, D.; Ford, W. T.; Zhang, Y.; Kotov, N. A. *Chem. Mater.* **2005**, *17*, 2131-2135.

(30) Everall, N. J. *Appl. Spectrosc.* **2000**, *54*, 1515-1520.

(31) Matthew, W. M.; Vy, H. T. N.; Emily, A. S. *Vib. Spectrosc* **2013**, *65*, 95-100.

(32) Meyer, M. W.; Larson, K. L.; Mahadevapuram, R. C.; Lesoine, M. D.; Carr, J. A.; Chaudhary, S.; Smith, E. A. *ACS Appl. Mater. Interfaces* **2013**, *5*, 8686-8693.

(33) Damin, C. A.; Nguyen, V. H.; Niyibizi, A. S.; Smith, E. A. *Analyst* **2015**, *140*, 1955-1964.

(34) Bobbitt, J. M.; Mendivelso-Pérez, D.; Smith, E. A. *Polymer* **2016**, *107*, 82-88.

(35) Fontaine, N.; Furtak, T. *Phys. Rev. B: Condens. Matter* **1998**.

(36) Fumihiko, I.; Munsok, K. *Jpn. J. Appl. Phys.* **2008**, *47*.

(37) Schneider, G. F.; Calado, V. E.; Zandbergen, H.; Vandersypen, L. M. K.; Dekker, C. *Nano Lett.* **2010**, *10*, 1912-1916.

(38) Lesoine, M. D.; Bobbitt, J. M.; Zhu, S.; Fang, N.; Smith, E. A. *Anal. Chim. Acta* **2014**, *848*, 61-66.

المنارة للاستشارات

www.manaraa.com

(39) Bass, M.; DeCusatis, C.; Enoch, J.; Lakshminarayanan, V.; Li, G.; Macdonald, C.; Mahajan, V.; Van Stryland, E. *Handbook of optics, Volume II: Design, fabrication and testing, sources and detectors, radiometry and photometry*; McGraw-Hill, Inc., 2009.

(40) Kasarova, S. N.; Sultanova, N. G.; Ivanov, C. D.; Nikolov, I. D. *Opt. Mater.* **2007**, *29*, 1481-1490.

(41) Sultanova, N.; Kasarova, S.; Nikolov, I. *Acta Phys. Pol., A* **2009**, *116*, 585.

(42) McKee, K.; Smith, E. *Rev. Sci. Instrum.* **2010**, *81*, 43106.

(43) Matthew, W. M.; Kristopher, J. M.; Vy, H. T. N.; Emily, A. S. *J. Phys. Chem. C* **2012**, *116*.

(44) McKee, K.; Meyer, M.; Smith, E. *Anal. Chem.* **2012**, *84*, 9049-9055.

(45) McKee, K.; Meyer, M.; Smith, E. *Anal. Chem.* **2012**, *84*, 4300-4306.

المنارة للاستشارات
www.manaraa.com

Supporting Information

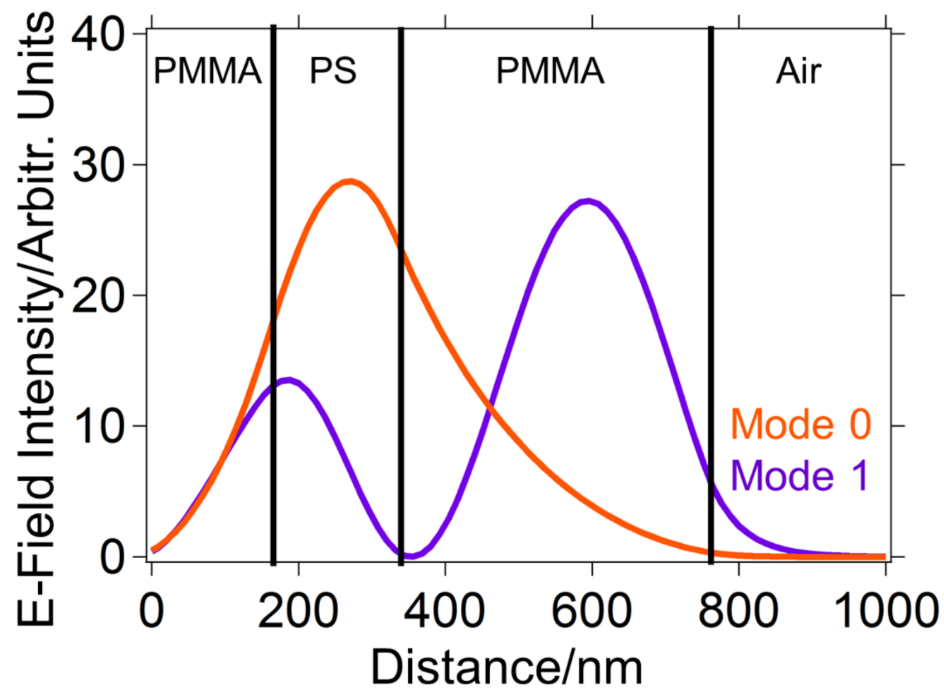

Figure S1: Calculated electric field intensity as a function of the distance from the prism/sample interface for sample 1-Tri. The purple curve corresponds to waveguide mode one at 51.95° and the orange curve corresponds to waveguide mode zero at 58.75°. The vertical black lines represent the interface locations.

www.manaraa.com

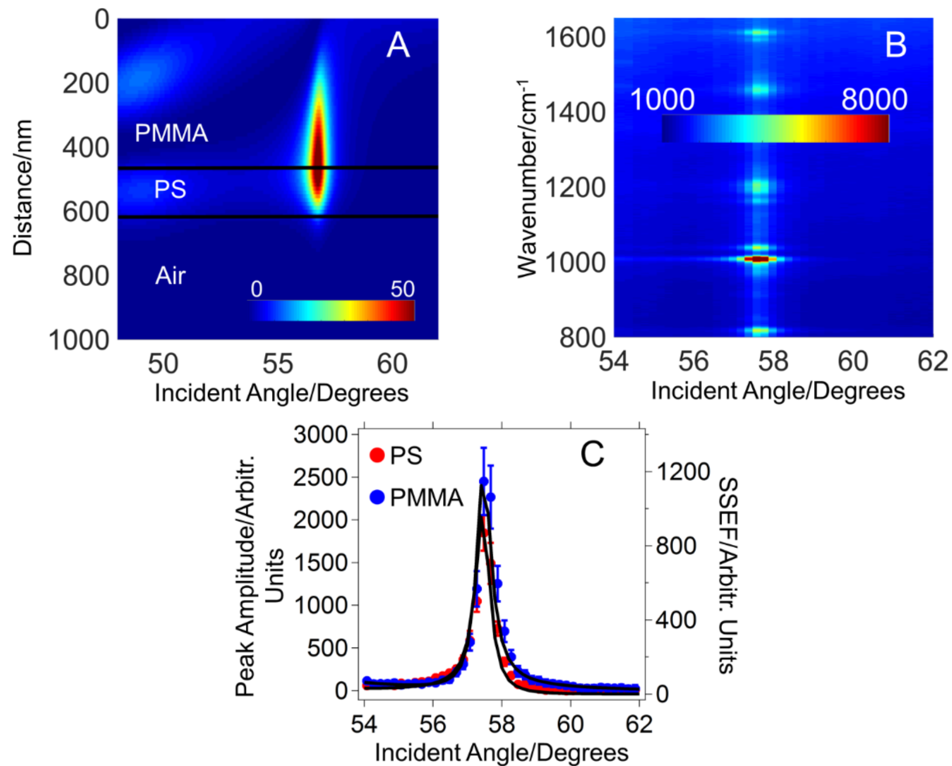

Figure S2: (A) Calculated electric field intensity (color scale) as a function of distance from sapphire prism interface and incident angle for sample 3-Bi. The horizontal black lines represent the PMMA/PS and PS/Air interfaces. The bilayer consists of 440 nm of PMMA and 189 nm of PS. (B) SA Raman spectra plotted as a function of incident angle, where the color scale represents the Raman intensity in counts. (C) shows the peak amplitude as a function of incident angle for the 812 cm^{-1} PMMA peak (blue circles) and the 1605 cm^{-1} PS peak (red circles) for sample 3-Bi. The error bars represent two replicate measurements. The SSEF fit that minimized the standard error of the estimate (s_{est}) between the experimental data are shown as black lines.

www.manaraa.com

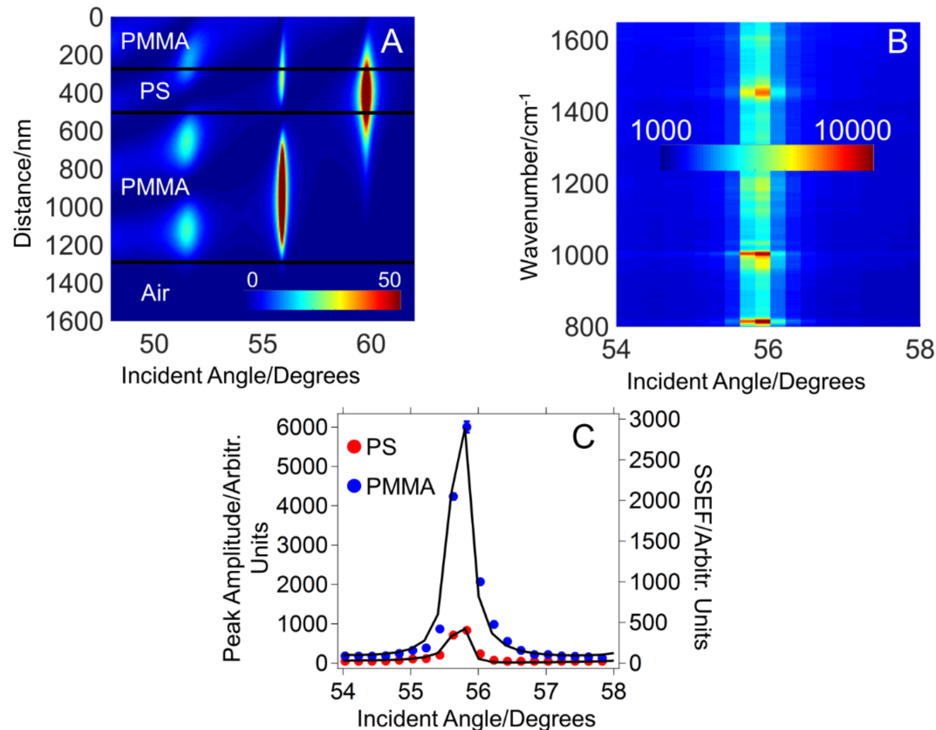

Figure S3: (A) Calculated electric field intensity (color scale) as a function of distance from sapphire prism interface and incident angle for sample 3-Tri. The horizontal black lines represent the PMMA/PS, PS/PMMA, and PMMA/Air interfaces. The trilayer film is 1263 nm thick with a 230 nm PS layer. The top PMMA layer is 350 nm, while the bottom PMMA layer is 680 nm thick. (B) SA Raman spectra plotted as a function of incident angle, where the color scale represents the Raman intensity in counts. (C) shows the peak amplitude as a function of incident angle for the 812 cm^{-1} PMMA peak (blue circles) and the 1605 cm^{-1} PS peak (red circles) for sample 3-Tri. The error bars represent two replicate measurements. The minimized standard error of the estimate (s_{est}) SSEF fit (black lines) for the SA Raman spectra are shown in the (C).

www.manaraa.com

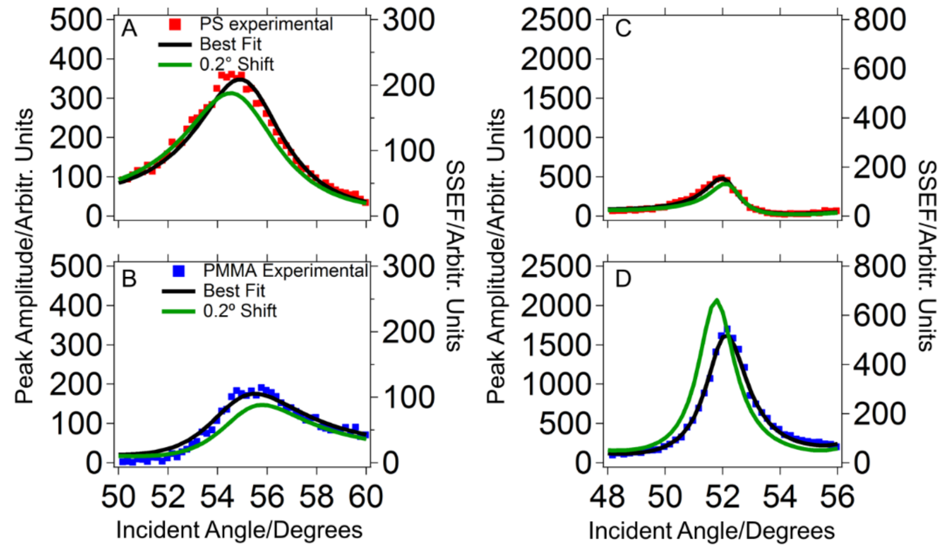

Figure S4: The peak amplitude as a function of incident angle plots for 1605 cm^{-1} (red squares) and 812 cm^{-1} (blue squares) for one experimental data set of samples (A, B) 1-Bi and (C, D) 1-Tri. The best SSEF fit (black lines) is determined by calculating the standard error of the estimate (s_{est}) over the angle range shown. The green line is the second-best fit that is shifted by at least 0.2°, which is the experimental angle step used for collecting the data. The second-best fit for sample 1-Bi and 1-Tri corresponds to a 10 nm (A and B) and a 20 nm (C and D) change in the PS and PMMA thicknesses, respectively.

المنارة للاستشارات
www.manaraa.com

CHAPTER 5

GENERAL CONCLUSIONS

There is an increasing demand for non-destructive *in situ* label-free characterization techniques for analyzing thin polymer waveguide films. Current non-destructive and destructive techniques are not capable of simultaneously providing optical, physical, and chemical properties, which are needed for developing and modeling new thin polymer waveguide devices. Thin polymer waveguide film devices are widely used in energy storage and capture devices, microelectronics, food packaging, and biomedical applications. The methods outlined in this dissertation are non-destructive optical-based spectroscopic methods for simultaneously characterizing thin polymer waveguide film's optical, physical, and chemical properties.

A Fourier transform (FT)-plasmon waveguide spectroscopy (PWR) method can analyze dielectric waveguide films. Polystyrene films' thicknesses and apparent anisotropic indices of refraction are determined using the FT-PWR method with better precision than destructive techniques like profilometry and atomic force microscopy. FT-PWR can be used to measure a variety of polymer layers, as well as non-polymer dielectric layers making it useful as a label free sensor. Replacing the polymer waveguide with a non-polymer waveguide will allow the FT-PWR method to measure the anisotropic properties of adsorbed analytes in lower concentrations than tradition surface plasmon resonance (SPR) and PWR spectroscopies.

المنارة للاستشارات
www.manaraa.com

Similarly, a scanning angle (SA) Raman spectroscopy method is developed to simultaneously measure the refractive index, thickness, and chemical content of mixed waveguide polymer films. The SA Raman spectroscopy method does not require smooth gold films and provides chemical content of thin waveguide films compared to the FT-PWR method. The peak ratios from SA Raman spectra of polystyrene-block-poly(methyl methacrylate) (PS-b-PMMA), PS-b-PMMA:PMMA, and two films of poly(2-vinylnapthalene)-block-poly(methyl methacrylate) (P2VN-b-PMMA) are used to calculate the chemical composition (fractional composition) of each mixed waveguide film. SA Raman peak amplitudes (1001 cm^{-1} PS or 1388 cm^{-1} P2VN) as a function of incident angle are fit by sum square electric field (SSEF) calculations to extract the thickness of the films. The method provides comparable results to profilometry, and is compatible with any mixed polymer film given there are unique Raman peaks for each polymer. The SA Raman spectroscopy method provides refractive index and thickness values for mixed polymer waveguide films, as well as the chemical content information from films too thin for traditional Raman spectroscopy.

Finally, the SA Raman spectroscopy method is modified to analyze bilayer and trilayer films consisting of PMMA/PS and PMMA/PS/PMMA, respectively. An iterative script that calculates all the possible SSEF fits for a given multilayer film is developed. The multilayer film total thickness and interface locations are extracted by fitting PMMA (812 cm^{-1}) and PS (1605 cm^{-1}) amplitudes as a function of incident angle with an axial spatial resolution of 7 to 80 nm. SA Raman spectroscopy and profilometry measurements of the multilayer films are comparable. The method can be easily applied to a variety of multilayer films if the index of refraction is known or measurable.

www.manaraa.com

Future SA Raman spectroscopy work should strive for measuring a variety of mixed and multilayer polymer waveguide films. The SA Raman spectroscopy methods presented in this dissertation will be useful for characterizing "real world" applications. A specific example would be photovoltaic devices, which consist of polymer mixtures and organic-inorganic mixtures fabricated into multilayer structures. The combination of iterative SSEF calculations and SA Raman spectroscopy will be needed for characterizing these photovoltaic devices or other multilayer mixture polymer waveguide films. Another application for future SA Raman spectroscopy experiments will be improving and modifying the methods presented to analyze non-waveguide films (thicknesses $< \frac{\lambda}{2\eta}$). Developing SA Raman spectroscopy into a depth profiling technique will allow for the analysis of nanodomains within thin polymer films.

المنارة للاستشارات
www.manaraa.com

APPENDIX A

HIGH ANGULAR-RESOLUTION AUTOMATED VISIBLE-WAVELENGTH SCANNING ANGLE RAMAN MICROSCOPY

Reprinted from Analytica Chimica Acta, 848, Michael D. Lesoine *et. al.*, High angular-resolution automated visible-wavelength scanning angle Raman microscopy, 61-66, Copyright (2014), with permission from Elsevier.

Michael D. Lesoine[a,b], Jonathan M. Bobbitt[a,b], Shaobin Zhu[a,b], Ning Fang[a,b], and Emily A. Smith[a,b]

[a]U.S. Department of Energy, Ames Laboratory, Ames, Iowa, 50011, United States

[b]Department of Chemistry, Iowa State University, 1605 Gilman Hall, Ames, Iowa 50011, United States

Abstract

A scanning angle Raman microscope with 532-nm excitation is reported for probing chemical content perpendicular to a sample interface. The instrument is fully automated to collect Raman spectra across a range of incident angles from 20.50 to79.50° with an angular spread of 0.4 ± 0.2° and an angular uncertainty of 0.09°. Instrumental controls drive a rotational stage with a fixed axis of rotation relative to a prism-based sample interface mounted on an inverted microscope stage. Three benefits of SA Raman microscopy using visible wavelengths, compared to near infrared wavelengths are: (i)

www.manaraa.com

better surface sensitivity; (ii) increased signal due to the frequency to the fourth power dependence of the Raman signal, and the possibility for resonant enhancement; (iii) the need to scan a reduced angular range to shorten data collection times. These benefits were demonstrated with SA Raman measurements of thin polymer films of polystyrene or a diblock copolymer of polystyrene and poly(3-hexylthiophene-2,5-diyl). Thin film spectra were collected with a signal-to-noise ratio of 30 using a 0.25 second acquisition time.

Introduction

Raman spectroscopy has been used in many fields to identify the chemical composition of diverse samples.[1-7] Several variants of Raman instruments have been developed, including portable units[8-10] and imaging systems.[11,12] Another variant of Raman instruments has the capability to probe interfaces using total internal reflection (TIR) illumination.[13-26] For these measurements the incident laser is directed at an interface with an incident angle (θ_i) at or above the critical angle (θ_c) as given by Snell's law: $\theta_c = \sin^{-1}\left(\frac{\eta_{\text{sample}}}{\eta_{\text{prism/objective}}}\right)$, where η_{sample} and $\eta_{\text{prism/objective}}$ are the indices of refraction of the interfacial layers. A typical sample setup for a TIR experiment is shown in Figure 1.

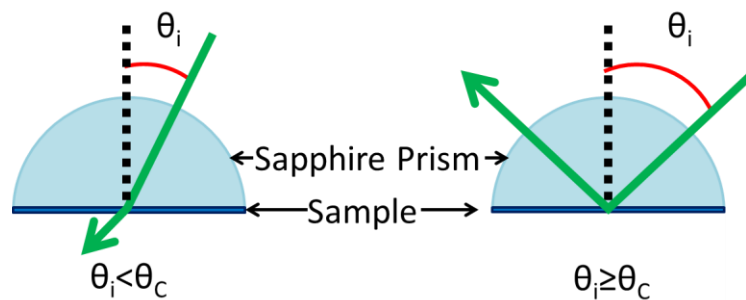

www.manaraa.com

Figure 1. Sapphire/polystyrene interface showing transmission and reflection of the incident excitation light (left) below and (right) at or above the critical angle, respectively.

Two layouts to achieve TIR are through the objective and through a high index of refraction prism.[16-21,24,26,27] Through the objective TIR has the benefit of ease of implementation, but is limited to samples with a low index of refraction (e.g., aqueous) and the exact incident angle is rarely known. In addition, the incident angle for a typical TIR objective is limited to a maximum value in the 67° range.[28] The use of a prism generally presents a greater alignment challenge; however, a high index of refraction prism allows a much wider range of samples to be measured and the angle of incidence is easily determined.

We have previously reported a variation of Raman spectroscopy termed scanning angle (SA) Raman spectroscopy.[20-23,25] SA Raman instruments have a controlled and variable incident angle upon a prism/sample interface in the range of around 25 to 75° with a resolution of a tenth of a degree or less. Three distinct regions in the scanned angular range are below, at, and above the critical angle for total internal reflection. Up to a few orders of magnitude enhancement in the Raman signal is measured at the critical angle. At angles greater than the critical angle, the penetration of the evanescent wave into the sample decreases and these angles are suitable for selectively probing the interface.[14-19] When the sample meets conditions required for a waveguide, spectra collected at angles below the critical angle provide simultaneous information on chemical

المنارة للاستشارات
www.manaraa.com

content and sample thickness.[22,23] The pattern of the Raman signal as the incident angle is changed upon a waveguide interface can be correlated to sample thickness.

Excitation wavelength is an important experimental parameter for any Raman spectroscopy experiment. The Raman intensity scales with the excitation frequency to the fourth power, making shorter excitation wavelengths desirable. However, considerations of the spectral background often make longer excitation wavelengths necessary for many Raman experiments. In addition to these considerations, for SA Raman spectroscopy the excitation wavelength affects the predicted angular dependence of the signal. Under TIR, 98% of the Raman scattering is generated in the sample within a distance D_{RS} (equation 1), which is another important parameter that is dependent on the excitation wavelength (λ) and incident angle (θ_i).[26]

$$D_{RS} = \frac{\lambda}{4 \times \pi} \frac{1}{\sqrt{\left[\left(\eta_{prism}^2 \times sin^2\,\theta_i\right) - \eta_{sample}^2\right]}} \quad (1)$$

For a sapphire/polystyrene interface, the calculated D_{RS} at a 68° incident angle for 785 and 532-nm excitation wavelengths are 148 and 123 nm, respectively. The D_{RS} at 78° is close to the minimum value that can be achieved with many optical schemes and is 90 nm (785-nm excitation) and 65 nm (532-nm excitation). SA Raman measurements with visible excitation wavelengths are predicted to produce better surface sensitivity with smaller D_{RS} values at large incident angles.

In this study, we report a newly developed 532-nm SA Raman instrument that has the benefits of improved design, increased signal due to the short excitation wavelength and resonant enhancement, and decreased experimental times. The incident angular range, spread and uncertainty have been characterized, and a comparison of excitation

المنارة للاستشارات
www.manaraa.com

wavelength on the SA Raman signal for several polymer interfaces has been conducted. The instrument will be of use in a variety of fields where interfacial characterization is needed, particularly in applications that benefit from measurements at ambient laboratory conditions.

Experimental Methods

Instrumentation

The developed instrument can be used for SA Raman imaging or epi-illumination (Figure 2).

المنارة للاستشارات
www.manaraa.com

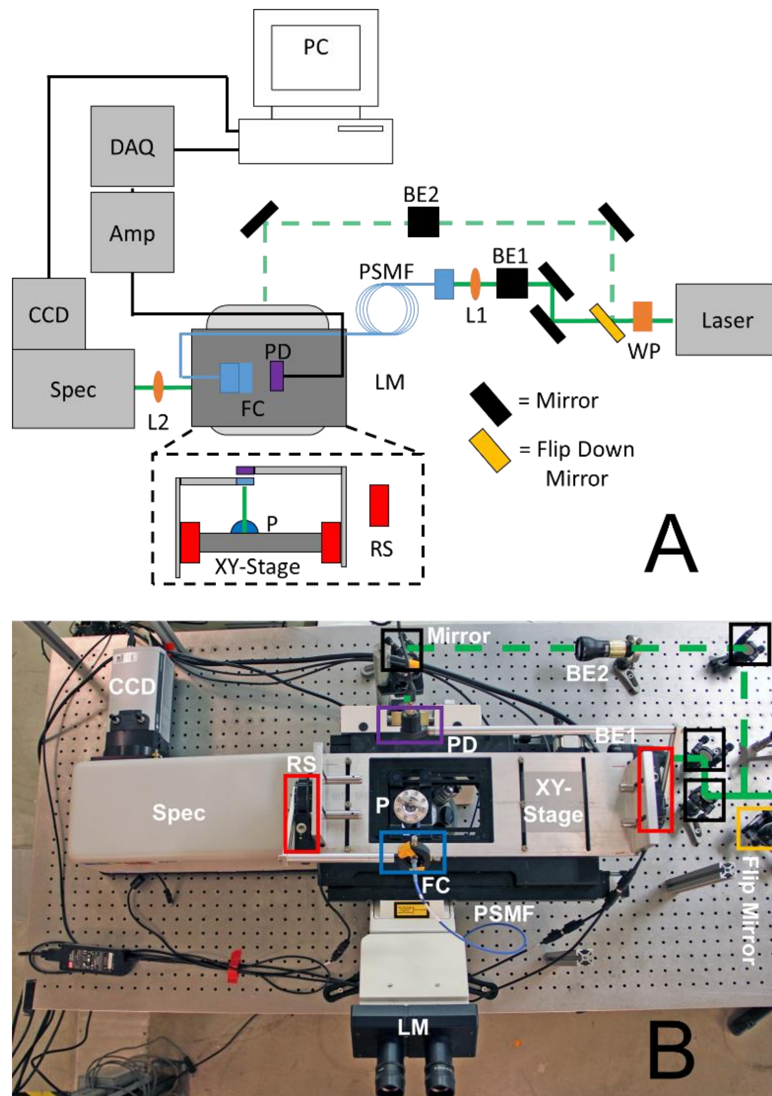

Figure 2: (A) Instrument schematic for a 532-nm SA Raman microscope: half wave-plate (WP), beam expanders (BE1, BE2), Leica microscope (LM), aspheric focusing lens (L1), polarization-maintaining single-mode fiber optic (PSMF), fiber collimator (FC), high index prism (P), photo-diode (PD), rotational stages (RS), amplifier (Amp), data acquisition device (DAQ), computer (CPU), collection lens (L2), spectrometer (Spec), and charged-coupled device (CCD). The dashed view is perpendicular to the optical table. (B) Picture of the 532-nm SA Raman microscope. The laser is not shown. Selected items are highlighted in the picture with color-coded boxes to match the schematic.

المنارة للاستشارات
www.manaraa.com

A single frequency 532-nm laser (Sapphire SF 532 nm 150 mW, Coherent, Santa Clara, CA) set to s-polarization was used for the excitation source. For epi-illumination imaging, the light was directed via a flip down mirror to a 10× beam expander (59-127, Edmund Optics, Barrington, NJ) then the rear port of a DM IRBE microscope (Leica, Wetzlar, Germany). A dichroic mirror (LPD01-532RU-22×27×2.0, Semrock, Rochester, NY) directed the laser to a 10×-magnification 0.25-numerical aperture microscope objective (Leica) that focuses the laser onto the sample plane. For SA Raman imaging, the light was expanded via a 1-3× beam expander (64417, Edmund Optics) to backfill a focusing optic that sends the light into a polarization maintaining single mode fiber (P3-488PM-FC-2, Thorlabs, Newton, NJ). The focusing optic and fiber optic input coupler were mounted on separate translational stages that allow for fine tuning the alignment. The power incident on the fiber was 150 mW and the power exiting the fiber was ~15 mW. A fiber collimator (CFC-2X-A, Thorlabs) at the output end was mounted on a rotational stage (T-RSW60A, Zaber Technologies, Vancouver, British Columbia, Canada) that directs the light with fine control over the incident angles, facilitated by software developed in LabVIEW (version 2010, National Instruments, Austin, TX), onto a 25.4-mm diameter hemispherical sapphire prism (ISP Optics, Irvington, NY) optically coupled to a 25.4-mm diameter 400-µm thick sapphire substrate. The laser spot size was ~75 µm in diameter at the sample interface in the SA mode.

The Raman signal was collected by a 10× objective, directed to a side port on the microscope, and focused onto the entrance of a HoloSpec *f*/1.8i spectrograph (Kaiser Optical Systems, Ann Arbor, MI) in both the epi-illumination and SA imaging modes. The spectrometer contains a holographic notch filter (532-nm SuperNotch) and a 100-µm

المنارة للاستشارات
www.manaraa.com

slit (SLIT-100) and grating (HSG-532-LF). The spectra were collected with a charged coupled device (CCD) (Newton 940, Andor Technology, Belfast, UK) with 2048 × 512 pixels and Solis software version 4.23.30002.0 (Andor Technology). Two accumulations were collected to facilitate automatic solar ray removal. Images were generated by raster scanning the sample using a XY-translational stage (ProScan, Prior Scientific, Rockland, MA) with a 35 μm step size.

The reflected light intensity from the prism/sample interface was collected along with the Raman scattering in the SA Raman imaging mode. An amplified photodiode (SM1PD1A and PDA200C, Thorlabs) on a second rotational stage (T-RSW60A, Zaber Technologies) moves in concert with the first rotational stage. The photodiode output voltage was measured with a National Instruments (Austin, TX) NI USB-6221 data acquisition device. Reflectivity measurements were collected at a rate of 1 KHz for 0.5 seconds per angle with an angular-resolution of ~0.005 to 0.05°.

Sample preparation

A thin polystyrene film was made by spin coating 50 μL of a 4.4 wt.% solution of polystyrene (Sigma-Aldrich, St Lois, MO) in toluene (Fisher Scientific, Waltham, MA) on a sapphire substrate (Meller optics, Providence, RI) at 3000 RPM for one minute utilizing a W-4A spin coater (Chemat Technology, Inc. Northridge, CA). A diblock copolymer of polystyrene (15 wt.%) and poly(3-hexylthiophene-2,5-diyl) (85 wt.%) film (PS-b-P3HT) was made by spin coating 100 μL of a 5 wt.% solution in chloroform (Fisher Scientific) on a sapphire substrate at 1000 RPM for 40 seconds or 100 μL of a 2 wt.% solution in dichlorobenzene (Fisher Scientific) on a sapphire substrate at 2000 RPM for 40 seconds. Optical contact between the prism and substrate was established with

www.manaraa.com

index matching fluid (η = 1.7800 Cargille Laboratories, Cedar Grove, NJ). 1.00 and 1.15 wt.% NaCl (Fisher Scientific) solutions were prepared in deionized water from an Easy Pure II purification system (Fisher Scientific).

Data processing and calculations

All data were processed using the software Igor Pro 6.3.2.3 (Wavemetrics, Lake Oswego, OR) or Origin 8.6 (OriginLab, Northampton, MA). Fresnel reflectivity coefficients were calculated and used to fit the experimental reflectivity data to determine the instrumental angular spread and uncertainty.[29] The calculations allow the incident angle to have a spread of values rather than a discrete angle. MSEF calculations were performed using EM Explorer (EM Explorer, San Francisco, CA). The refractive indices used in all calculations were $\eta_{sapphire} = 1.76355$,[30] $\eta_{polystyrene} = 1.59861$,[31] and $\eta_{air} = 1.00028$.[32] Selected Raman peaks were fit to a Gaussian using Igor Pro's batch-fitting function.[33] To generate images, spectra collected with the Solis software were processed using Igor Pro to obtain peak amplitude, width, and location. The desired properties were input into MATLAB version 2013b (Mathworks, Natick, MA) to construct images.

Results and Discussion

Characterization of instrument specifications

The goals of this work were to develop a SA Raman microscope based on a simple layout and to demonstrate the benefits of visible excitation wavelength SA Raman spectroscopy by measuring thin polymer films. The SA Raman microscope utilized a fiber optic to direct the laser onto a prism/sample interface (Figure 2). The layout has the advantage of few moving parts; and the ability to compare epi and SA-illumination geometries using a simple flip down mirror. A single rotational stage mounted on the

المنارة للاستشارات
www.manaraa.com

microscope's translational stage was the only moving part required for collecting Raman data. A second rotational stage mounted on the opposite side of the translational stage recorded the reflected light intensity from the interface, which was used for angle calibration. The instrumental design was compatible with any excitation wavelength. For this work, a 532-nm laser was utilized.

The parameters that need to be determined experimentally for any SA Raman instrument include the angular calibration, range, spread, and uncertainty. A summary of all measured parameters is shown in Table 1.

المنارة للاستشارات

www.manaraa.com

Table 1. Measured instrumental parameters for the 532-nm SA Raman instrument and calculated values for a sapphire/polystyrene interface.

Spectral Range[a]	150-2460 cm^{-1}
Incident angle spread	0.4° ± 0.2°
Incident angle uncertainty	0.09°
Highest angle	79.50°
Lowest angle	20.50°
Values for a sapphire/polystyrene interface (532 nm excitation)	
θ_c	65.05°
D_{RS} range (65.05-79.50°)	1.3 µm-63 nm
Average ΔD_{RS} near the θ_c (65.50-66.00)	7.8 nm
Average ΔD_{RS} far from the θ_c (75.00-79.50)	0.1 nm

[a]lower value limited by notch filter, upper value limited by grating and detector

The angular range and spread were characterized by collecting the reflected light intensities from a sapphire/364 ± 8-nm polystyrene interface. The curve of reflected light intensity was fit using Fresnel reflectivity coefficients. First, the experimental curve was adjusted by 4.77° to overlap with the calculated curve at angles below approximately 30° (Figure 3A). This provides an angular calibration, which was necessary since the input angle in the software does not necessarily represent the true incident angle. There was a rapid drop in the reflected light intensity below 20.50° and above 79.50°, within this range was suitable for data collection. The angular range of this instrument was measured to be 9° larger than a previously reported instrument that utilized 2 translational stages and a galvanometer to control the incident angle of light upon the interface.[20] Next, the angular spread was characterized by fitting the experimental data in the region between 0.5° below to 0.5° above the critical angle. The angular spread in the calculated Fresnel reflectivity coefficients was adjusted until the calculation coincides with extremes

المنارة للاستشارات
www.manaraa.com

established by the uncertainty in the reflectivity data (Figure 3B). The angular spread was 0.4 ± 0.2°. This was 2.5° smaller than a previously reported SA Raman instrument.[20] A small angular spread is desirable when measuring and fitting SA Raman signals, as an average signal is obtained across all incident angles. Near the critical angle, the expected enhancement in the Raman signal decreases by 16% and 38% for a 0.4 and 2.9-degree angular spread, respectively.

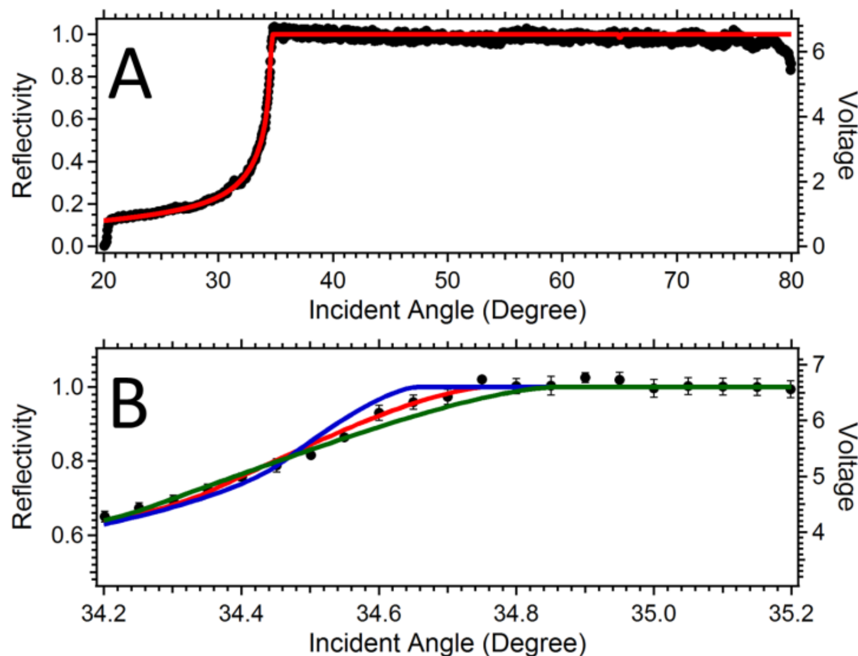

Figure 3: Reflectivity curve from (A) sapphire/364 ± 8 nm polystyrene/air interface (black squares) with a best fit Fresnel reflectivity curve that has a 0.4 ± 0.2° incident angle spread (red curve). (B) Expanded view of (A) near the critical angle with Fresnel reflectivity curves corresponding to an angle spreads of 0.2° (blue curve), 0.4°, and 0.6° (green curve). The signal was collected every 0.05° between adjacent data points.

Since the reflectivity values were used to calibrate the incident angle of the laser upon the interface, the uncertainty in the reflectivity data affects the uncertainty in the

المنارة للاستشارات
www.manaraa.com

incident angle. This in turn affects the ability to model SA Raman data. The angular uncertainty was measured using dilute NaCl solutions of varying concentration to alter their refractive index (Figure 4A). Three replicate reflectivity measurements for each NaCl solution were averaged and the standard deviations were calculated. The average standard deviation for all reflectivity data was 0.04. Near the critical angle in the reflectivity curves shown in Figure 3B, a 0.04 uncertainty in the reflectivity corresponds to a 0.09° uncertainty in the incident angle. The mean in reported incident angles had a 0.09° uncertainty combined with a 0.4° spread, as discussed above.

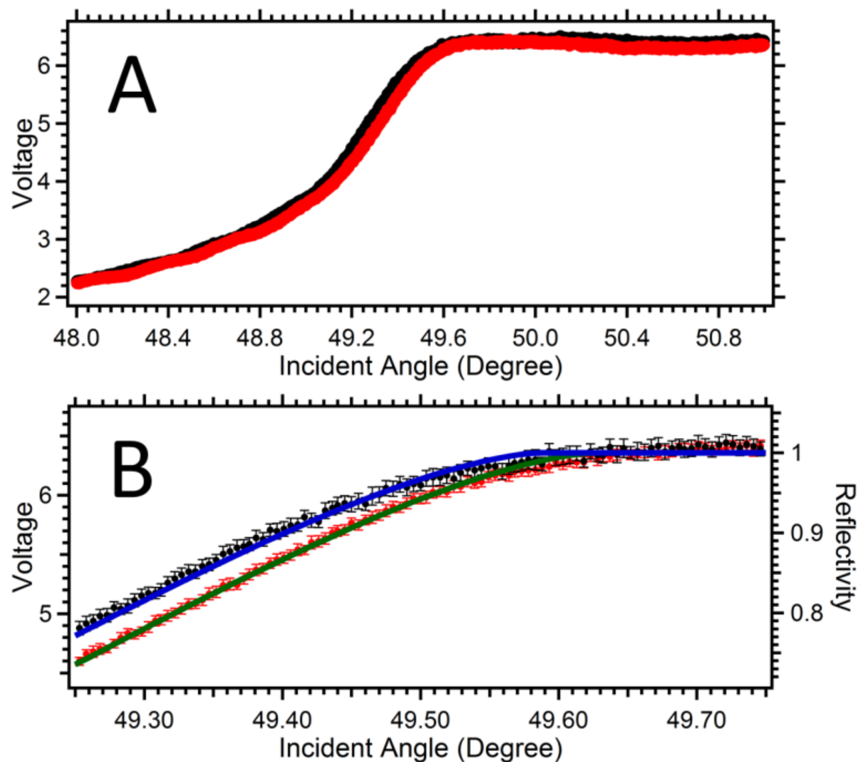

Figure 4: (A) Comparison of the reflectivity curves of a 1.00 (black circles) and 1.15 (red circles) wt.% NaCl solution. (B) An expanded view around the critical angles to show the standard deviation.

المنارة للاستشارات
www.manaraa.com

SA Raman instruments require a precise alignment of the laser's axis of rotation with the center of the hemispherical prism. The sensitivity of the alignment on the resulting data was tested by collecting spectra at a fixed incident angle while translating the stage holding the prism/sample. A uniform 364 ± 8-nm polystyrene film was used, which should generate a uniform Raman intensity. Deviations from a uniform Raman signal were assumed to be a result of misalignment. As shown in Figure 5 there was a ~100 µm oblong region around the center of the prism that yielded the highest signal-to-noise ratio. Outside of this maximal region the signal was decreased by roughly an order of magnitude. The sample translational stage aided in obtaining the optimal alignment in the SA optical path.

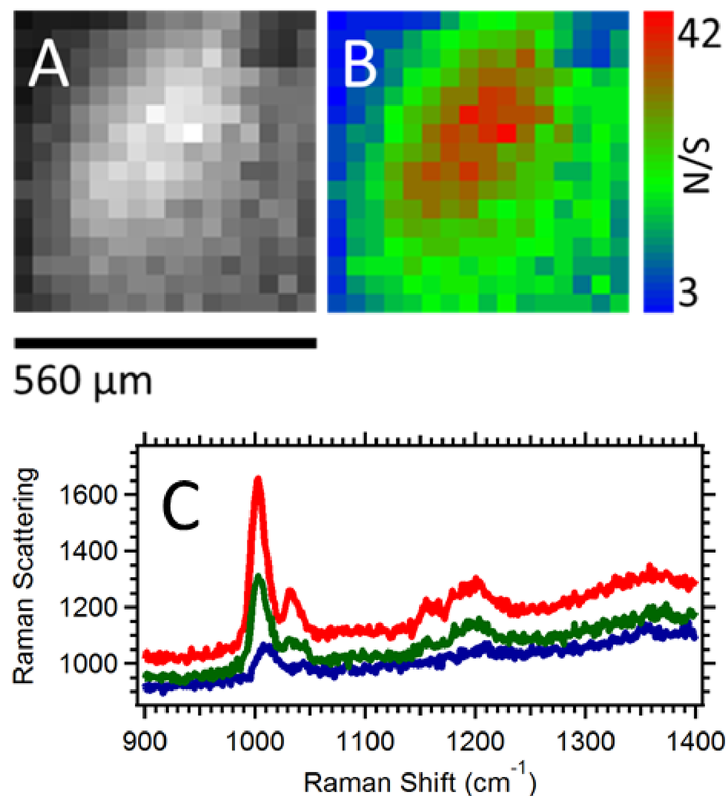

Figure 5: Images taken in the SA mode of a 364 ± 8 nm polystyrene film depicting the (A) magnitude and (B) an associated signal-to-noise ratio of the ~1000 cm^{-1} peak. (C)

المنارة للاستشارات

www.manaraa.com

Raman spectra over the range of signal-to-noise values with corresponding color-coded scheme shown in (B). Raman measurements were collected with an acquisition time of 15 seconds, and a step size of 35 µm.

Considerations of the excitation wavelength for SA Raman spectroscopy: increased signal.

In addition to the frequency to the fourth dependence of the Raman signal, possible resonant enhancements are expected to generate larger Raman signals with visible excitation wavelengths. A diblock copolymer film composed of semiconducting thiophene-based P3HT and polystyrene (PS-b-P3HT) was prepared and atomic force microscopy images indicated its thickness was ~65 nm. Thiophene absorbs across the visible region of the electromagnetic spectrum (Figure 6A). For a PS-b-P3HT copolymer film, the thiophene Raman peaks should exhibit resonance enhancement with 532-nm excitation, whereas polystyrene will not.

المنارة للاستشارات

www.manaraa.com

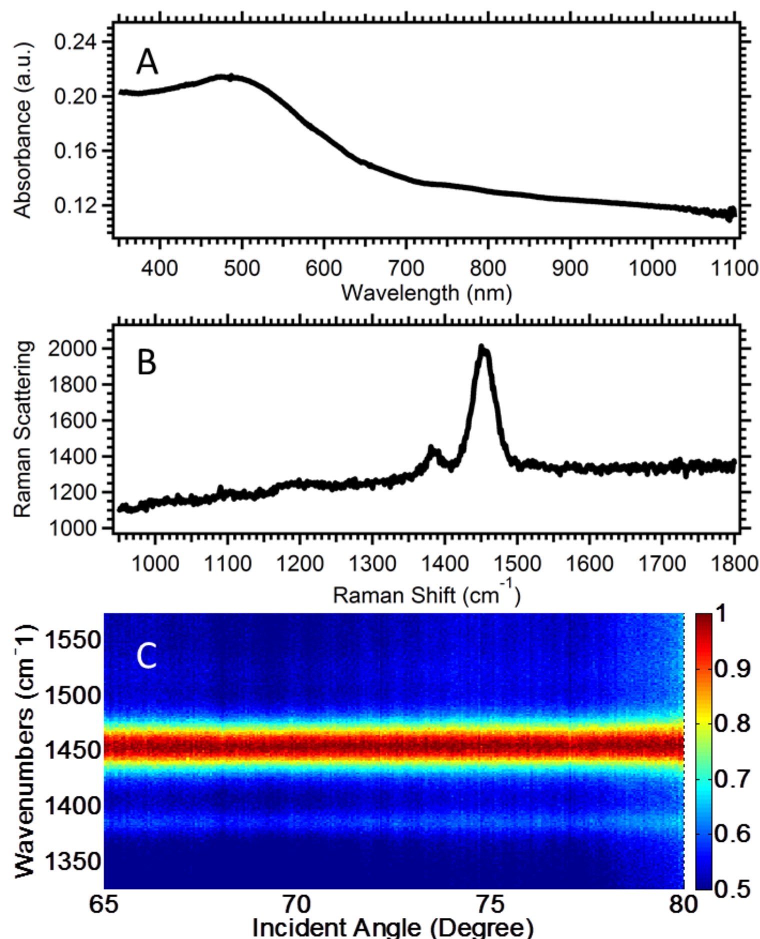

Figure 6: For a ~65-nm PS-b-P3HT film on sapphire: (A) absorption spectrum; (B) Raman spectrum with a 2.5 second acquisition time; and (C) Raman scattering intensity as function of wavenumber and incident angle with background subtraction and normalization of the signal to the 1455 cm^{-1} thiophene peak.

The Raman spectrum of the diblock copolymer film collected at a 40° incident angle is shown in Figure 6B. Strong thiophene Raman peaks were measured at 1385 and 1455 cm^{-1} corresponding to C–C skeletal stretching and C=C ring stretching, respectively. The signal-to-noise ratio of the 1455 cm^{-1} thiophene peak was 40, and no polystyrene peaks were measured as expected due to a lack of resonant enhancement. The

www.manaraa.com

spectra collected upon scanning the incident angle from 64 to 80° are shown in Figure 6C. The index of refraction of the diblock copolymer is not known. The reflectivity data support the notion that the diblock copolymer, like pure P3HT, has a larger index of refraction than the sapphire prism. Thus, total internal reflection is not achieved at the sapphire/diblock copolymer interface, and the entire film thickness is probed at each angle. The uniform Raman signal at all incident angles is consistent with probing the entire thin film. The signal-to-noise ratio for a 490 ± 60-nm film of the diblock copolymer film was 120 and 40 for 532-nm (18 mW) and 785-nm (90 mW) SA Raman excitation, respectively. The higher signal-to-noise ratio with 532-nm SA Raman excitation is primarily the result of resonant enhancement, although some differences in the instrumental parameters also play a part. The frequency dependence of the Raman signal has been compensated by the laser powers. With both excitation wavelengths, the MSEF calculations for this interface predict an order of magnitude increase in the signal when using SA Raman illumination compared to a 180° back scattering illumination. The improved signal-to-noise ratios with visible excitation wavelengths enable collection times of a fraction of a second for nanometer-thick films.

One limitation to visible-wavelength SA Raman spectroscopy occurs when collecting measurements at a gold interface. Due to the optical properties of gold, excitation with a 785-nm laser generates larger SA Raman signals and enables the measurement of a monolayer with a ~50-nm gold film, whereas no signal was generated using 532-nm excitation (data not shown).

المنارة للاستشارات
www.manaraa.com

Considerations of the excitation wavelength for SA Raman spectroscopy: decreased scanning angular range.

A graph of predicted Raman intensity (i.e., mean squared electric field (MSEF)) versus incident angle for a polystyrene waveguide film shows narrower features with 532 compared to 785-nm excitation (Figure 7A-C). This means sample thickness can be determined by scanning a narrower range of angles using visible excitation wavelengths, and this reduces experimental time.

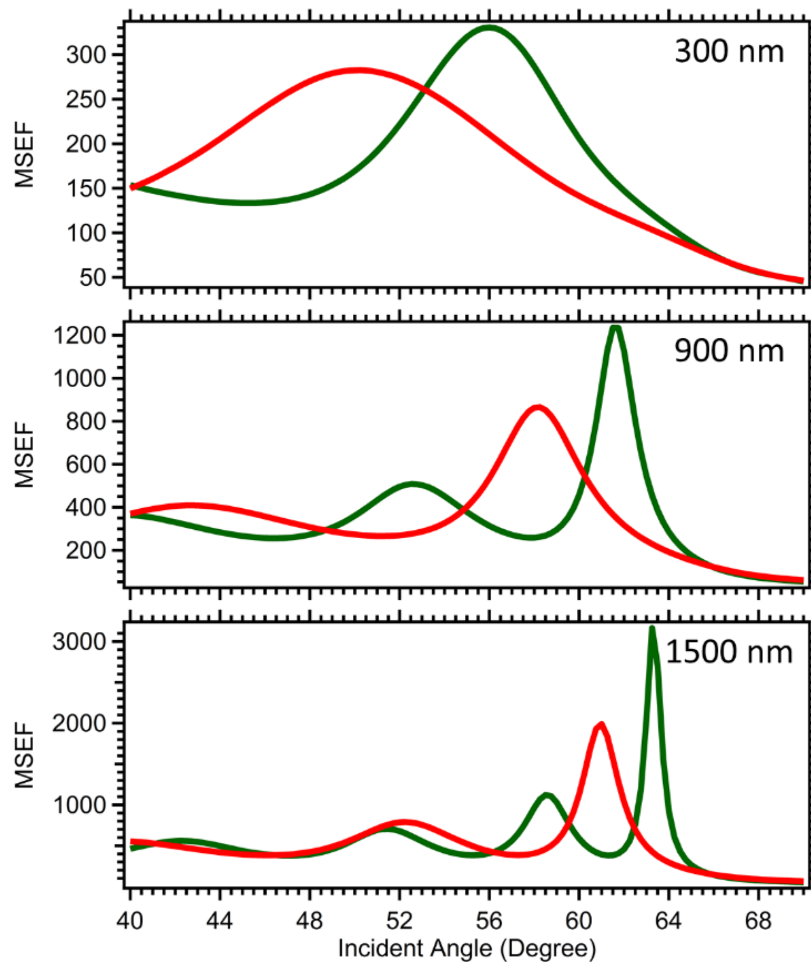

Figure 7: Comparison of the sum of the mean squared electric field (MSEF) for sapphire/(A) 300-nm, (B) 900-nm, and (C) 1500-nm polystyrene interface for (green) 532 and (red) 785-nm excitation.

المنارة للاستشارات
www.manaraa.com

In order to demonstrate the ability to measure polymer waveguide thickness using a narrow range of incident angles, SA Raman spectra were collected for a polystyrene film prepared by spin coating a 5 wt.% solution onto a substrate. The Raman spectra were collected every 0.05° over the angular range 55.50 to 68.00° (Figure 8).

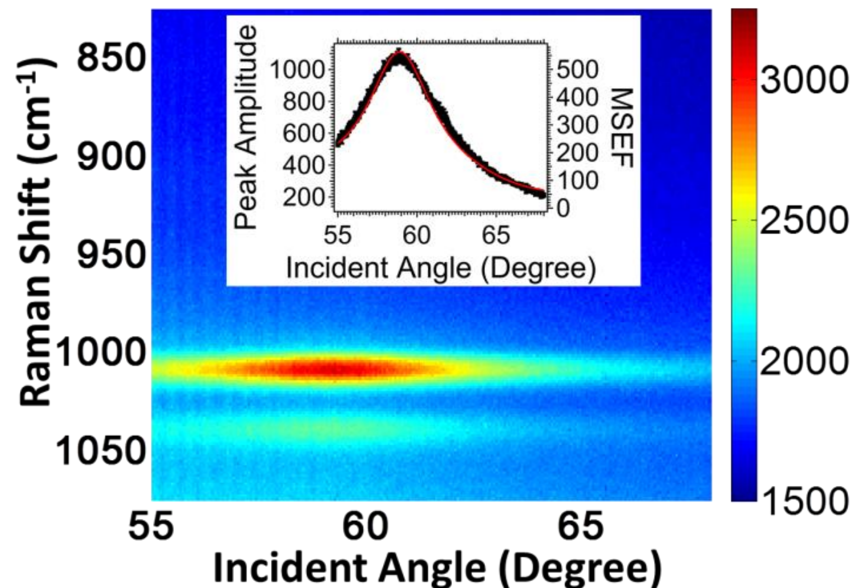

Figure 8: SA Raman spectra of a 420-nm polystyrene film. The ~1007 cm^{-1} peak exhibits an angle-dependent signal, as expected for a waveguide. The maximum signal is measured at 59.25°. The critical angle for the interface is 65.0°. The thin film's Raman data (black curve inset) were best modeled (MSEF, red curve inset) to a 420-nm thickness. A 2.5-minute acquisition time was used to obtain a spectrum at each incident angle.

The intensity of the Raman signal varies with incident angle, as expected for a waveguide, and the maximum Raman signal was measured at 59.25°. Matching this experimentally determined maximum with calculations of the mean squared electric

www.manaraa.com

field[23] within polymer layers of varying thickness, the polystyrene film was measured to be 420 nm (Figure 8). If using 785-nm excitation the maximum in the Raman signal for a 420-nm film was centered at 54.40° and twice the angular range was needed to sufficiently model the data compared to when 532-nm light was used.

Thinner films can be measured as waveguides using visible wavelengths compared to near infrared wavelengths. The minimum polystyrene thickness required to support a waveguide using 532-nm excitation is ~170 nm. At the opposite thickness extreme, polystyrene films greater than 1000 nm require a high angular resolution because of the narrow waveguide peaks (Figure 7). The instrument described herein has the scanning capabilities and angular-resolution to simultaneously measure the thickness and composition at both thickness extremes with second or sub second collection times per spectrum when resonance is achieved, minutes collection time in total for a 40° angular range, and signal-to-noise ratios exceeding 30.

Conclusions

An automated visible-wavelength SA Raman instrument was constructed with an angular range of 20.50° to 79.50°, uncertainty of 0.09°, and spread of 0.4° ± 0.2°. The instrument's function was demonstrated by measuring thin polymer films. Visible wavelength SA Raman spectroscopy generates better signal-to-noise ratio spectra and the need to scan a narrower range of angles when measuring waveguides compared to the use of infrared lasers. Increased surface sensitivity and signals will make it possible to measure faster kinetics and dynamic events than was previously feasible with SA Raman spectroscopy. In addition, the coupling of resonant conditions to enhance sample

المنارة للاستشارات
www.manaraa.com

detection without the use of specialized substrates (e.g., plasmon supporting) will prove beneficial in expanding the utility of the technique.

Acknowledgements

This research is supported by the U.S. Department of Energy, Office of Basic Energy Sciences, Division of Chemical Sciences, Geosciences, and Biosciences through the Ames Laboratory. The Ames Laboratory is operated for the U.S. Department of Energy by Iowa State University under Contract No. DE-AC02-07CH11358. The authors thank Dr. Curtis Mosher of the Roy J. Carver Laboratory for Ultrahigh Resolution Biological Microscopy for performing AFM measurements on the PS-b-P3HT diblock copolymer.

References

(1) Delhaye, M.; Bridoux, M.; Wallart, F. *Journal of Molecular Structure* **1982**, *79*, 51-66.

(2) Vendrell, M.; Maiti, K. K.; Dhaliwal, K.; Chang, Y.-T. *Trends in Biotechnology* **2013**, *31*, 249-257.

(3) Poliakoff, M.; Howdle, S. M.; Kazarian, S. G. *Angewandte Chemie International Edition in English* **1995**, *34*, 1275-1295.

(4) Weckhuysen, B. M. *Chemical Communications* **2002**, 97-110.

(5) Biju, V.; Itoh, T.; Anas, A.; Sujith, A.; Ishikawa, M. *Analytical & Bioanalytical Chemistry* **2008**, *391*, 2469-2495.

(6) Stuart, D. A.; Haes, A. J.; Yonzon, C. R.; Hicks, E. M.; Van Duyne, R. P. *IEE Proceedings -- Nanobiotechnology* **2005**, *152*, 13-32.

المنارة للاستشارات

www.manaraa.com

(7) Lupoi, J.; Singh, S.; Simmons, B.; Henry, R. *Bioenerg. Res.* **2014**, *7*, 1-23.

(8) Cullum, B. M.; Mobley, J.; Chi, Z.; Stokes, D. L.; Miller, G. H.; Vo-Dinh, T. *Review of Scientific Instruments* **2000**, *71*, 1602-1607.

(9) Zhang, X.; Young, M. A.; Lyandres, O.; Van Duyne, R. P. *Journal of the American Chemical Society* **2005**, *127*, 4484-4489.

(10) Kudelski, A. *Talanta* **2008**, *76*, 1-8.

(11) Weiss, I. M.; Tuross, N.; Addadi, L.; Weiner, S. *Journal of Experimental Zoology* **2002**, *293*, 478-491.

(12) Keren, S.; Zavaleta, C.; Cheng, Z.; de la Zerda, A.; Gheysens, O.; Gambhir, S. S. *Proceedings of the National Academy of Sciences* **2008**, *105*, 5844-5849.

(13) Ikeshoji, T.; Ono, Y.; Mizuno, T. *Appl. Opt.* **1973**, *12*, 2236-2237.

(14) Iwamoto, R.; Miya, M.; Ohta, K.; Mima, S. *Journal of the American Chemical Society* **1980**, *102*, 1212-1213.

(15) Iwamoto, R.; Ohta, K.; Miya, M.; Mima, S. *Applied Spectroscopy* **1981**, *35*, 584-587.

(16) Fujiwara, K.; Watarai, H. *Langmuir* **2003**, *19*, 2658-2664.

(17) Tisinger, L. G.; Sommer, A. J. *Microscopy and Microanalysis* **2004**, *10*, 1318-1319.

(18) Greene, P. R.; Bain, C. D. *Colloids and Surfaces B: Biointerfaces* **2005**, *45*, 174-180.

(19) Beattie, D. A.; Larsson, M. L.; Holmgren, A. R. *Vibrational Spectroscopy* **2006**, *41*, 198-204.

(20) McKee, K. J.; Smith, E. A. *Review of Scientific Instruments* **2010**, *81*, -.

المنارة للاستشارات

www.manaraa.com

(21) McKee, K. J.; Meyer, M. W.; Smith, E. A. *Analytical Chemistry* **2012**, *84*, 4300-4306.

(22) McKee, K. J.; Meyer, M. W.; Smith, E. A. *Analytical Chemistry* **2012**, *84*, 9049-9055.

(23) Meyer, M. W.; McKee, K. J.; Nguyen, V. H. T.; Smith, E. A. *The Journal of Physical Chemistry C* **2012**, *116*, 24987-24992.

(24) Woods, D. A.; Bain, C. D. *Analyst* **2012**, *137*, 35-48.

(25) Meyer, M. W.; Nguyen, V. H. T.; Smith, E. A. *Vibrational Spectroscopy* **2013**, *65*, 94-100.

(26) Greene, P. R.; Bain, C. D. *Spectroscopy Europe* **2004**, *16*, 8-15.

(27) Greene, P. *SpectroscopyEurope* **2004**, *16*.

(28) Paige, M. F.; Bjerneld, E. J.; Moerner, W. E. *Single Molecules* **2001**, *2*, 191-201.

(29) Corn, R. M., 2014.

(30) Bass, M.; DeCusatis, C.; Enoch, J.; Lakshminarayanan, V.; Li, G.; MacDonald, C.; Mahajan, V.; Van Stryland, E. *Handbook of Optics, Third Edition Volume IV: Optical Properties of Materials, Nonlinear Optics, Quantum Optics (set)*; Mcgraw-hill, 2009.

(31) Kasarova, S. N.; Sultanova, N. G.; Ivanov, C. D.; Nikolov, I. D. *Opt. Mater.* **2007**, *29*, 1481-1490.

(32) Ciddor, P. E. *Appl. Opt.* **1996**, *35*, 1566-1573.

(33) Bradley, M. S.; Krech, J. H. *The Journal of Physical Chemistry* **1992**, *96*, 75-79.

المنارة للاستشارات

www.manaraa.com

APPENDIX B

QUANTITATIVE COMPARISON OF ORGANIC PHOTOVOLTAIC BULK HETEROJUNCTION PHOTOSTABILTY UNDER LASER ILLUMINATION

Reprinted with permission from Lesoine, M. D.; Bobbitt, J. M.; Carr, J. A.; Elshobaki, M.; Chaudhary, S.; Smith, E. A., Quantitative Comparison of Organic Photovoltaic Bulk Heterojunction Photostability Under Laser Illumination. *J. Phys. Chem. C* **2014,** *118* (51), 30229-30237. Copyright 2014 American Chemical Society.

Michael D. Lesoine[1,2§], Jonathan M. Bobbitt[1,2§], John A. Carr[3], Moneim Elshobaki[4,5] Sumit Chaudhary[3,4], Emily A. Smith[1,2,]

[1]U.S. Department of Energy, Ames Laboratory, Ames, Iowa, 50011, United States;

[2]Department of Chemistry, Iowa State University, 1605 Gilman Hall, Ames, Iowa 50011, United States;

[3] Department of Electrical and Computer Engineering, Iowa State University, Ames, Iowa 50011, United States; and

[4] Department of Materials Science and Engineering, Iowa State University, Ames, Iowa 50011, United States

[5] Department of Physics, Mansoura University, Mansoura, 35516, Egypt.

[§] Both authors contributed equally

www.manaraa.com

Abstract

The photostability of bulk heterojunction organic photovoltaic films containing a polymer donor and a fullerene-derivative acceptor was examined using resonance Raman spectroscopy and controlled laser power densities. The polymer donors were poly(3-hexylthiophene-2,5-diyl) (P3HT), poly[[9-(1-octylnonyl)-9H-carbazole-2,7-diyl]-2,5-thiophenediyl-2,1,3-benzothiadiazole-4,7-diyl-2,5-thiophenediyl] (PCDTBT), or poly({4,8-bis[(2-ethylhexyl)oxy]benzo[1,2-b:4,5-b′]dithiophene-2,6-diyl}{3-fluoro-2-[(2-ethylhexyl)carbonyl]thieno[3,4-b]thiophenediyl}) (PTB7). Four sample preparation methods were studied: (i) thin or (ii) thick films with fast solvent evaporation under nitrogen, (iii) thick films with slow solvent evaporation under nitrogen, and (iv) thin films dried under nitrogen conditions followed by thermal annealing. Polymer order was assessed by monitoring a Raman peak's full width at half-maximum and location as a function of illumination time and laser power densities from 2.5×10^{3} to 2.5×10^{5} Wcm^{-2}. Resonance Raman spectroscopy measurements show that before prolonged illumination PCDTBT and PTB7 have the same initial order for all preparation conditions, while P3HT order improves with slow solvent drying or thermal annealing. All films exhibited changes to bulk heterojunction structure with 2.5×10^{5} Wcm^{-2} laser illumination as measured by resonance Raman spectroscopy, and atomic force microscopy images show evidence of sample heating that affects the polymer over an area greater than the illumination profile. Photostability data are important for proper characterization by techniques involving illumination and the development of devices suitable for real-world applications.

المنارة للاستشارات

www.manaraa.com

Introduction

Organic photovoltaic devices (OPVs) fabricated from polymer donors and fullerene-derivative acceptors are a promising portable and renewable source of electricity.[1,2] A common OPV design has a transparent substrate, a transparent anode, anodic buffer layer, an active layer containing a donor mixed with acceptor, a cathodic buffer layer and finally a cathode.[2] Other designs have been reported.[2,3] The morphology and order of the active layer affect OPV performance.[4,5] A bound electron-hole pair (exciton) is created upon absorption of light by the donor. Bulk heterojunction morphology consists of a highly ordered polymer donor with an interpenetrating bicontinuous acceptor structure that helps facilitate the dissociation of an exciton at the interface between the donor and acceptor. Donor/acceptor domains of the size of the exciton diffusion length, typically less than 10 nm, are essential to prevent the majority of the excitons from decaying.[6] Morphology affects, among other properties, electronic defects (e.g., distortions in the geometry of sp^2 carbon covalent bonds in π-conjugated polymers' backbone), charge mobility (i.e., electron transport efficiency), and absorption (e.g., shift to longer wavelengths with increasing polymer order).[7-9]

Performance metrics for OPV devices typically focus on how efficiently a constructed device converts solar radiation into electricity. Of equal importance is the development of stable OPVs with long operating lifetimes.[10-18] One reported case showed that OPV stability increases when low molecular weight organic contaminants are removed from the polymer PBDTTPD (poly[[5-(2-ethylhexyl)-5,6-dihydro-4,6-dioxo-4*H*-thieno[3,4-c]pyrrole-1,3-diyl][4,8-bis[(2-ethylhexyl)oxy]benzo[1,2-b:4,5-b′]dithiophene-2,6-diyl]]).[14] The short-circuit current density of cells stored in dark and

المنارة للاستشارات

www.manaraa.com

inert conditions drops only 6% after 111 days when size exclusion chromatography is used to reduce low molecular weight species. Fullerene-based acceptors containing bulky substituents to suppress crystallinity increased thermal stability. Devices fabricated from these acceptors can be maintained at 150 °C up to 10 hours without degradation of device efficiency.[10] In addition to altering the composition of the donor and acceptor, OPVs are being optimized with different preparation conditions. For example thermal[10,13,19,20] and solvent[21] annealing can improve device performance for P3HT-based OPVs. Treatment of the hole transport layer with ultraviolet light is reported to improve OPV stability as a result of increased wettability and contact with the active layer.[15] These selected examples may not extend to other systems; degradation mechanisms are known to be complex and largely material specific.

Raman spectroscopy can be used to measure chemical and structural properties of the OPV active layer.[21-25] Reported indicators of order in thiophene-based bulk heterojunction OPVs are the location and FWHM of the thiophene symmetric stretch.[21,24-27] Smaller FWHM or Raman shifts are reported to correspond to an increase in the device efficiency.[21,23-25] Furukawa reported the Raman spectra of powdered and solution P3HT with maximum intensities at 1450 and 1470 cm^{-1}, respectively.[28,29] The solution should exhibit relative disorder while the powder is expected to exhibit relative order. A recent publication by Wood et al. showed negligible shifts in the thiophene peak maximum with heating up to at least 140° C and a shift of approximately 15 cm^{-1} only after annealing the film at ~200° C.[30]

We report photostability measurements of bulk heterojunction thin films prepared with one of three polymer donors and one of four sample preparation methods using

المنارة للاستشارات

www.manaraa.com

resonance Raman spectroscopy combined with controlled laser power densities. Raman spectroscopy is ideally suited for these measurements since the changes in the spectra over time simultaneously provide information about the polymer stability and the mechanism of degradation. For example, changes in the Raman peaks can be assigned to specific functional groups and spectral background can indicate changes in luminescence. Many previous Raman studies of OPV films don't report laser power densities or, when reported, used high laser power densities. This may affect the measurement of polymer order through sample heating, degradation or a similar mechanism. Our work provides additional information on the photostability of OPV thin films prepared with different active layer compositions and processing methods, while simultaneously elucidating the effect of laser power density on the measurement of polymer order.

Experimental Methods

Film preparation

Samples were generated with the strata shown in Figure 1.

المنارة للاستشارات

www.manaraa.com

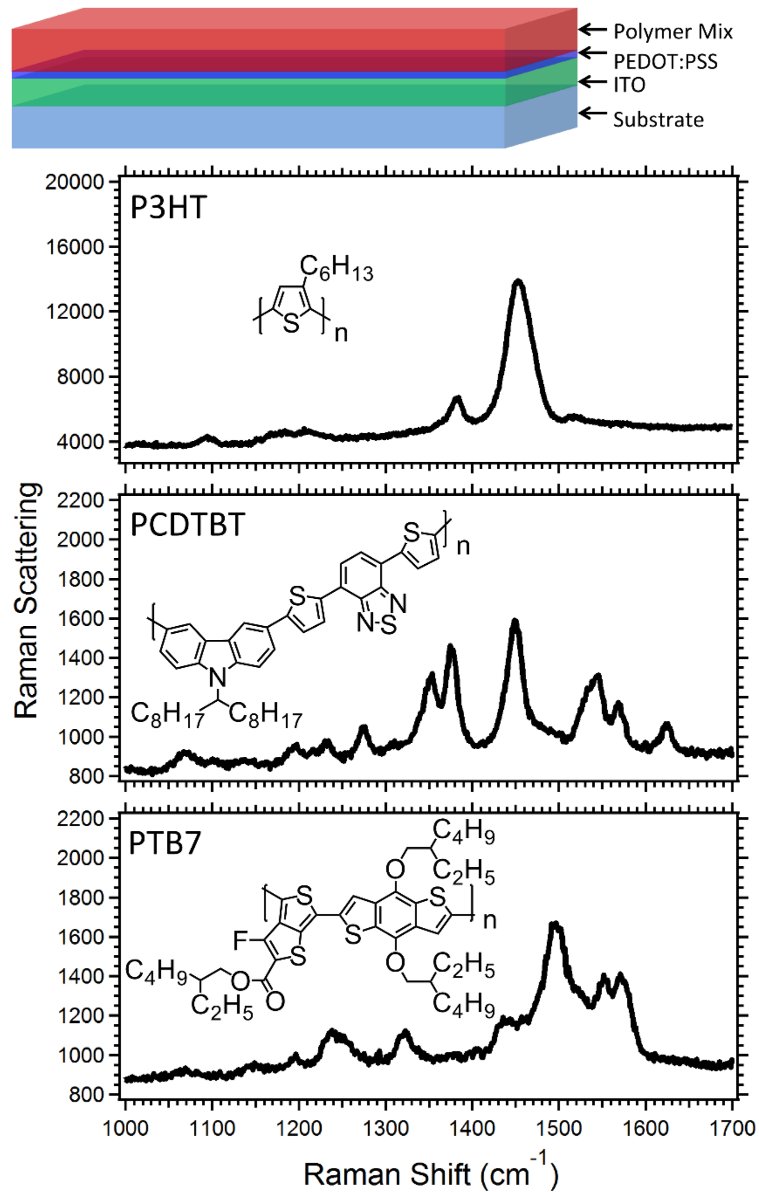

Figure 1: At top is a schematic of the sample layout. Raman spectra of samples formed with the donor P3HT, PCDTBT or PTB7 (as indicated by the label and structure) mixed with $PC_{60}BM$. P3HT (180.6 ± 0.7 nm thickness), PCDTBT (180 ± 10 nm), and PTB7 (160 ± 10 nm) films were prepared with solvent evaporation under nitrogen and measured with 2.5×10^3 (P3HT) or 5.0×10^3 Wcm^{-2} (PCDTBT and PTB7)

المنارة للاستشارات
www.manaraa.com

All samples were prepared and annealed in a nitrogen environment. First glass substrates coated with a 120 to 160-nm layer of indium tin oxide (ITO) from Delta Technologies were spin coated with poly(3,4-ethylenedioxythiophene) and poly(styrenesulfonate) (PEDOT:PSS) (*Clevios*™ P VP AI 4083, Heraeus Precious Metals GmbH & Co. KG, Leverkusen, Germany) at 4,000 rpm for 60 s to form a 30 to 40-nm layer. Next, a film of P3HT, PCDTBT, or PTB7 (1-Material, Dorval, Quebec, Canada) mixed with the acceptor PC_xBM (x = 60 for P3HT and x = 70 for PCDTBT and PTB7) was formed. The specific film compositions and spin coating parameters are shown in Table 1. Four preparation methods were used with each donor: a slow or fast spin coating speed (which affects the film thickness) with drying under nitrogen, slow spin coating speed with slow solvent evaporation under nitrogen, and a fast spin coating speed with drying under nitrogen followed by thermal annealing for 10 minutes. After initial sample preparation, the PCDTBT and PTB7 samples were stored under vacuum for 24 hours before measurements were performed. The films were removed from the nitrogen environment, and all further analyses were performed at ambient laboratory conditions. The thickness of the films was measured after the Raman spectra were collected with a NewView™ 7100 Profilometer (Zygo, Middlefield, CT).

المنارة للاستشارات

www.manaraa.com

Table 1: Sample preparation conditions and measured thickness for the samples included in this study.

Polymer	Sample	Ratio[1]	RPM[2]	Time (s)[3]	Drying	Thermal annealing	Thickness (nm)[4]	FWHM (cm^{-1})[5]
P3HT	Fast Dry Thick	1:1	600	40	Nitrogen	NA	277 ± 3	34.1 ± 0.7
	Slow Dry Thick	1:1	600	40	Solvent[6]	NA	278 ± 5	31.3 ± 0.4
	Fast Dry Thin	1:1	1000	40	Nitrogen	NA	180.6 ± 0.7	34.73 ± 0.07
	Fast Dry Thermal Anneal Thin	1:1	1000	40	Nitrogen	100°C; 600 s	170 ± 20	32.2 ± 0.3
PCDTBT	Fast Dry Thick	1:3.5	600	40	Nitrogen	NA	180 ± 10	22.2 ± 0.6
	Slow Dry Thick	1:3.5	600	40	Solvent[6]	NA	170 ± 20	22.2 ± 0.3
	Fast Dry Thin	1:3.5	1500	40	Nitrogen	NA	111 ± 8	22.0 ± 0.6
	Fast Dry Thermal Anneal Thin	1:3.5	1500	40	Nitrogen	80°C; 600 s	81 ± 3	22.5 ± 0.8
PTB7	Fast Dry Thick	1:1.5	600	60	Nitrogen	NA	160 ± 10	20.9 ± 0.8
	Slow Dry Thick	1:1.5	600	60	Solvent[6]	NA	190 ± 10	21 ± 1
	Fast Dry Thin	1:1.5	1000	60	Nitrogen	NA	114 ± 4	22.1 ± 0.8
	Fast Dry Thermal Anneal Thin	1:1.5	1000	60	Nitrogen	80°C; 600 s	103 ± 6	21 ± 1

[1]Ratio of polymer donor to PC_xBM acceptor; [2]Spin-coating speeds, rotations per minute; [3]Spin-coating duration; [4]As determined by profilometry; [5]2.5×10^3 Wcm^{-2}; [6]Solvent was 1, 2-dichlorobenzene and 2 hours elapsed during drying under nitrogen

المنارة للاستشارات
www.manaraa.com

Spectral measurements

A lab-built Raman microscope based on a DM IRBE platform (Leica, Wetzlar, Germany) with 532-nm laser excitation with a FWHM of 15.8 ± 0.2 cm^{-1} (Sapphire SF 532 nm 150 mW, Coherent, Santa Clara, CA) was used to perform the Raman measurements. The laser profile was expanded using a 10× beam expander (59-127, Edmund Optics, Barrington, NJ) to backfill a 10×-magnification 0.25-numerical aperture microscope objective (Leica) to achieve a laser spot with a diameter of 1.6 ± 0.2 μm. Laser excitation powers at the sample were 50-5000 μW corresponding to 2.5×10^3 to 2.5×10^5 Wcm^{-2}. The films were illuminated with 1.8×10^4 to 1.8×10^6 suns equivalent of 532-nm laser. The suns equivalent was determined by dividing the laser power density (at 532 nm) by the integrated power density of the sun over all wavelengths. The objective was used to both focus the laser for excitation as well as collect the Raman scattering signal from the epi-direction. The Raman signal was focused with a lens onto a HoloSpec *f*/1.8i spectrograph (Kaiser Optical Systems, Ann Arbor, MI) and directed to a charged coupled device (CCD) (Newton 940, Andor Technology, Belfast, UK) with 2048 × 512 pixels.

Raman spectra were obtained at ambient laboratory conditions using Solis software version 4.23.30002.0 (Andor Technology). Collection times between 1 to 150 seconds were used depending on the excitation power to maintain a signal-to-noise ratio in the range of 40 to 75 throughout the measurements. Two collections were performed to facilitate cosmic ray removal. Raman images of P3HT samples were generated with a lab-developed program in LabVIEW (2010 version, National Instruments, Austin, TX) to translate a sample on a XY-stage (ProScan, Prior Scientific, Rockland, MA). A power

المنارة للاستشارات
www.manaraa.com

density of 2.5×10^3 Wcm^{-2} was used with a collection time of 15 seconds and a stage movement of 1 μm per step.

Absorption spectra were collected using an Agilent 8453 UV-visible spectrophotometer (Santa Clara, CA). A sample without the active layer was used to collect a blank spectrum.

Data analysis

Raman spectra were analyzed using Igor Pro 6.3.2.3 (Wavemetrics, Lake Oswego, OR) batch-fit function with a Gaussian fit from 1325 to 1525 cm^{-1} for P3HT and PCDTBT and 1450 to 1550 cm^{-1} for PTB7. A linear baseline was used in all the fits. The properties of a spectral peak, including full-width at half-maximum (FWHM) and location, were plotted as a function of time for the stability measurements. Luminescence, which appears as background in Raman spectra, was measured in a spectral region without Raman peaks (2000 cm^{-1}).

Results and Discussion

Bulk heterojunction thin film photostability measured with controlled laser power densities and resonance Raman microscopy

The Raman spectra of films containing P3HT:$PC_{60}BM$, PCDTBT:$PC_{70}BM$, or PTB7:$PC_{70}BM$ with thicknesses between 160 to 180 nm are shown in Figure 1. (Hereafter, only the polymer donor is used to identify the sample under study and the acceptor is omitted for simplicity.) All three polymer donors have thiophene-based groups in their backbone, and exhibit resonantly-enhanced Raman spectra using 532-nm excitation due to the appreciable absorption at this wavelength (Figure 2).

المنارة للاستشارات
www.manaraa.com

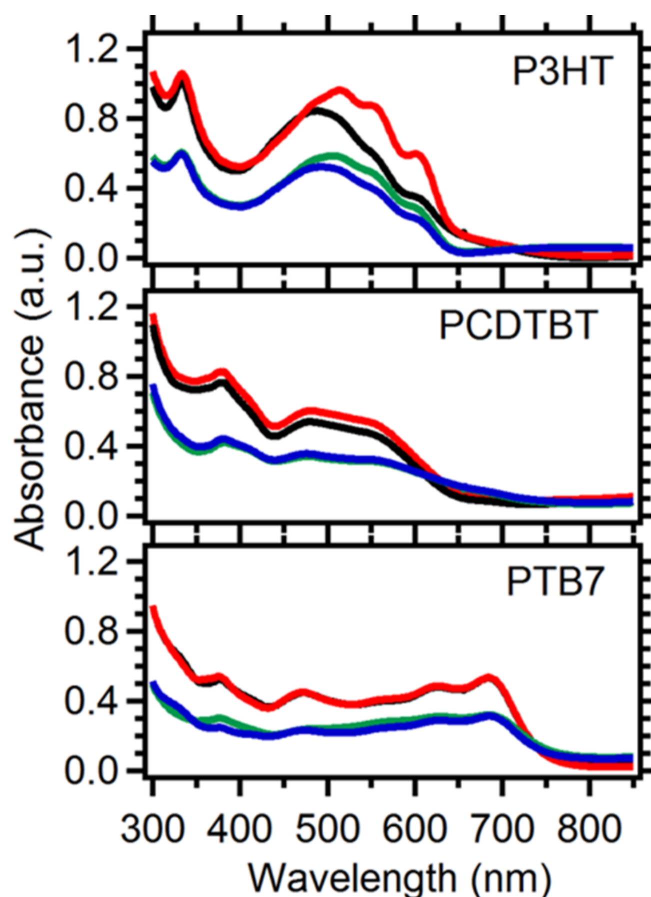

Figure 2: Absorption spectra for P3HT, PCDTBT or PTB7 samples with the following preparation conditions: thick film with solvent evaporation under nitrogen (black); thick film with slow solvent evaporation under nitrogen (red); thin film with solvent evaporation under nitrogen (blue); and a thin film dried under nitrogen followed by thermal annealing (green). Other sample preparation conditions and thicknesses are shown in Table 1.

The most intense peak in each spectrum was used for subsequent stability measurements. These are the thiophene group at ~1450 cm^{-1} for P3HT,[20,31] a broad ring stretch spanning the two thiophenes and the benzothiadiazole at ~1447 cm^{-1} for PCDTBT,[32] and the 3-fluorothiophene group at ~1490 cm^{-1} for PTB7.[33] The Raman

المنارة للاستشارات
www.manaraa.com

spectrum of $PC_{60}BM$ and $PC_{70}BM$ has a peak at 1465 cm^{-1} that is not apparent in any of the spectra shown in Figure 1. This is expected since $PC_{60}BM$ and $PC_{70}BM$ have minimal absorption at 532 nm relative to the polymers, and also have a smaller Raman cross section compared to the polymers.[26] Using the same collection parameters, ~10× more signal is measured for P3HT compared to PCDTBT and PTB7. The latter two have similar signal intensities. In order to compare spectra with similar signal-to-noise ratios, the acquisition time for all subsequent Raman measurements was increased for PCDTBT and PTB7. This results in a decreased time resolution for photostability studies of these polymers compared to P3HT.

The samples prepared with fast solvent evaporation under nitrogen conditions were illuminated with power densities of 2.5×10^3 (P3HT), 5.0×10^3 (PCDTBT and PTB7), and 2.5×10^5 Wcm^{-2} while simultaneously collecting Raman spectra to measure the photostability of the films over time (Figure 3).

المنارة للاستشارات
www.manaraa.com

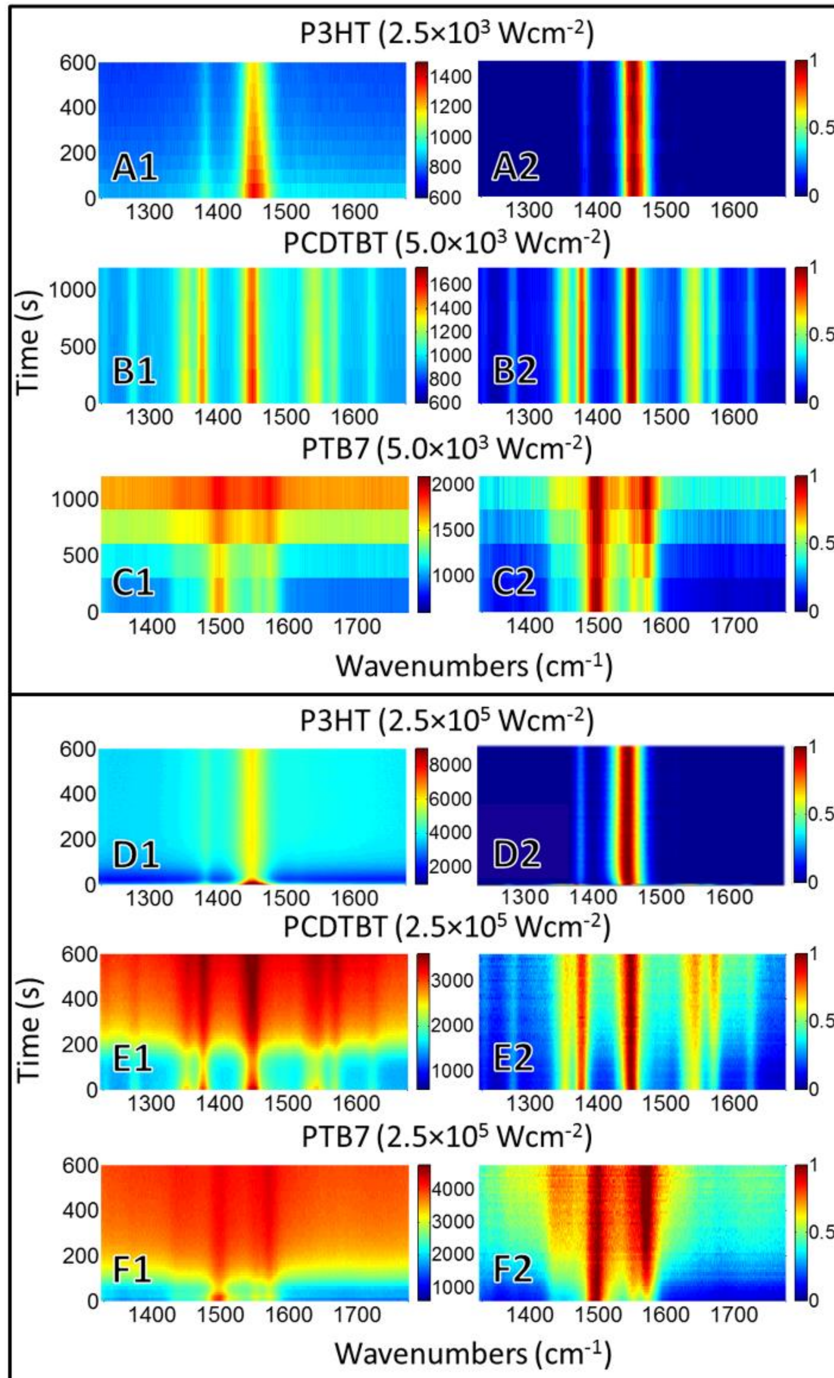

Figure 3: Raw (A1-F1) and normalized background subtracted (A2-F2) Raman spectra versus illumination time for samples prepared with the indicated donor. The laser power density is listed at the top of each set of graphs. All samples were thick films with solvent

المنارة للاستشارات

www.manaraa.com

evaporation under nitrogen (Table 1). The raw spectra show changes in peak intensity, including the generation of background luminescence, while the normalized spectra show changes in peak width and location. The color scale is Raman scattering intensity.

The unprocessed spectra (Figure 3, left column) reveal changes in the peak and background intensity. The electronic transitions that occur when using a resonant laser wavelength can generate background luminescence in the Raman spectra. With the same experimental conditions as used to collect data shown in figure 3, no Raman peaks are recorded for a solution of P3HT; the background luminescence dominates the spectrum (data not shown). Background luminescence is decreased and P3HT Raman peaks are measured for P3HT or P3HT:$PC_{60}BM$ solid thin films. The intensity of background luminescence is thus dependent on many properties including the bulk heterojunction structure. Changes in peak widths or locations are best observed in the spectra that have been background subtracted and normalized to the most intense peak in the spectra (Figure 3, right column).

For P3HT, a 33% decrease in the Raman peak intensity and a 38% decrease in luminescence over 112 seconds of illumination with 2.5×10^5 Wcm^{-2} is followed by a relatively stable Raman signal and slightly increased background over the remaining illumination time (Figure 3 D1). The decrease in the Raman signal with continuous illumination indicates less P3HT is measured over the analysis time. This could be the result of P3HT photodegradation (i.e., alterations in the chemical structure) or changes to the thickness of the film. Atomic force microscopy (AFM) images of the area illuminated by 2.5×10^5 Wcm^{-2} indicate there are morphological changes to the film because of the

المنارة للاستشارات
www.manaraa.com

laser illumination (Figure S1). Approximately 9% of the polymer is displaced from around the location of illumination to surrounding areas; surprisingly, the area affected is considerably greater than the 1.6 μm diameter spot of the laser profile. This suggests that sample heating occurs, affecting approximately 15 μm diameter spot centered around the illuminated area. The amount of polymer displaced by the laser does not entirely explain the 33% decrease in the Raman signal. Some P3HT photodegradation may be contributing to the initial decrease in Raman signal and background. With 2.5×10^5 Wcm^{-2} illumination the peak FWHM increases from 34.3 ± 0.1 to 36.3 ± 0.4 cm^{-1} over 600 seconds; the peak location does not change (Figure 3 D2). The polymer that is not displaced by the laser exhibits decreased order as measured by resonance Raman spectroscopy with 2.5×10^5 Wcm^{-2} illumination. The increase in luminescence with an onset time of 75 seconds suggests the bulk heterojunction, or mixing of P3HT and $PC_{60}BM$, may be affected by the illumination or resulting sample heating.

The Raman spectra of P3HT show a 14% decrease in the Raman peak intensity and 22% decrease in luminescence over 600 seconds with 5.0×10^3 Wcm^{-2}illumination (Figure 3 A1). Considering the normalized P3HT spectra, there is no meaningful change in the ~1450 cm^{-1} peak location and a slight increase in FWHM from 34.1 ± 0.7 to 35.3 ± 0.4 cm^{-1} with illumination (Figure 3 A2). No sign of laser-induced changes to the film were visible in optical images after illumination with 5.0×10^3 Wcm^{-2}. Some amount of polymer displacement and/or photodegradation explain the decrease in Raman signal and luminescence, however, there are minimal changes to the bulk heterojunction structure when studied with the lower power density. This is consistent with work by Manceau et al. that shows high stability with 1 sun (1000 W m^{-2}) over long exposure times for

المنارة للاستشارات
www.manaraa.com

thiophene-based donors, and is also consistent with the work by Tromholt et al. that shows low degradation rates for thick P3HT:PCBM films.[34,35]

The stability of the PCDTBT and PTB7 samples with illumination is fundamentally different compared to the P3HT sample. PCDTBT has a relatively stable Raman intensity, background, peak FWHM, and peak location with 5.0×10^{3} Wcm^{-2} illumination (Figure 3B1-B2). With 2.5×10^{5} Wcm^{-2} illumination, the Raman signal is constant, but there is an evolution of luminescence starting after approximately 200 seconds of illumination and a 2 cm^{-1} increased peak FWHM after 50 s (Figure 3 E1-E2). The AFM image of the illuminated area shows extensive morphology changes to the film with a decrease in polymer thickness localized to the area of illumination (Figure S1). Interestingly, the 82% decrease in the AFM height images at the area of illumination does not result in a decrease in the Raman intensity. One possibility for the stable PCDTBT Raman intensity could be due to the localized heating causing the $PC_{70}BM$ to phase segregate and migrate, which is known to occur during thermal annealing.[36] The Raman spectra of PTB7 follow similar trends at all power densities as measured for PCDTBT with a 5.0×10^{3} Wcm^{-2} illumination (Figure 3 C1-C2, F1-F2). Also, the AFM images of PTB7 after 5.0×10^{3} Wcm^{-2} illumination are nearly identical to the P3HT AFM image, both showing an approximately 9% displacement of the polymer film extending beyond the illuminated area. For both PCDTBT and PTB7, the relatively stable Raman intensity, increased FWHM, and increase in luminescence suggest a less favorable bulk heterojunction structure results with illumination or associated sample heating.

When performing laser-based measurements of thin films the power density should be low enough to avoid influencing the measurement unless photostability is the

www.manaraa.com

property of interest. Laser-based measurements can provide false information as a result of the laser illumination used to generate the data. The laser power and illumination area (i.e., power density) should be considered as well as the duration of illumination. High NA objectives are especially problematic as they focus the light to a small spot and can lead to substantial laser power densities. Power densities of 2.5×10^3 to 2.5×10^5 Wcm^{-2} with a 1.6 ± 0.2 μm diameter excitation spot size was used in this work (only data for selected, representative power densities have been included in the figures and tables). As discussed above, changes to the films were measured within seconds for P3HT, PCDTBT, and PTB7 at the higher end of the power density range used in this study, which is similar to the $\sim10^5$ Wcm^{-2} power densities with visible excitation wavelengths that have been used in some Raman studies of polymer order.[22,23] Recent work indicates that the film thickness can affect degradation rates for a polymer donor.[35,37,38] Two thickness ranges were included for each polymer donor in the present study; photostability rates may vary for other film thicknesses.

Bulk heterojunction thin film order and stability as a function of sample preparation method

Raman measurements were performed to determine the effect of preparation conditions on the polymer order in bulk heterojunction thin films. The peak FWHM was measured with 2.5×10^3 (P3HT) or 5.0×10^3 (PCDTBT and PTB7) Wcm^{-2} and a 3.5 second acquisition and illumination time (Table 1). In these studies peak FWHM exhibited greater changes than peak location from one sample to the next. P3HT shows significant changes to polymer order with varying sample preparation methods; this is consistent with other analysis methods.[21,39-41] The relative order is highest for the film that was

المنارة للاستشارات
www.manaraa.com

slowly dried by solvent annealing under nitrogen, and decreases for the film that was thermally annealed after drying under nitrogen. The least ordered are the thin and thick films dried under nitrogen without further processing. Figure S2 corresponds to 32×32 μm Raman images generated from FWHM of P3HT spectra measured with a power density of 2.5×10^3 Wcm^{-2}. Each image corresponds to one of the sample preparation methods studied. While the order varies for samples with different preparation conditions, as already discussed, the 0.3 cm^{-1} standard deviation in the FWHM indicates a high degree of uniformity across a sample. This is expected since the typical P3HT or PCBM domain size measured for samples with similar preparations conditions is reported to be considerably smaller (e.g., nanoscale) than the diameter of the laser spot used to collect the Raman images.[5] Absorption spectra are susceptible to changes in isolated, ordered and disordered phases of P3HT.[42] Peaks at 550 and 600 nm are assigned to ordered phases, while peaks at higher energies correspond to isolated and disordered phases. The Raman FWHM values (Table 1) and absorption spectra (Figure 2), when normalized to account for differences in film thickness, show relative agreement on the degree of polymer order for the P3HT films prepared with different preparation conditions.

In the case of PCDTBT and PTB7 there are no statistically significant differences in the FWHM measured for samples with different preparation conditions (Table 1). Raman spectroscopy measurements show that the PCDTBT film is not affected by thermal annealing at 80°. This finding is supported by neutron reflectivity and grazing incidence wide-angle X-ray scattering measurements that showed thermal annealing at 70° has a negligible effect on PCDTBT order.[43] Consistent with the Raman data,

المنارة للاستشارات
www.manaraa.com

PCDTBT and PTB7 show minimal changes in their absorption spectra for samples with different preparation conditions when sample thickness is taken into account (Figure 2).

Photostability was tested for each polymer donor and sample preparation method. The Raman spectra collected for the four sample preparation methods and three power densities are shown in Figure 4 for P3HT, Figure 5 for PCDTBT and Figure 6 for PTB7. Qualitatively the Raman spectral changes and luminescence (Figure 7) are similar to the trends that have already been discussed and are independent of sample preparation method for a given polymer donor. A quantitative measure of peak properties was performed for P3HT and PCDTBT (Table 2). The error in measuring the peak locations listed in Table 2 is based on the instrument spectral resolution of 13 cm^{-1}.

المنارة للاستشارات

www.manaraa.com

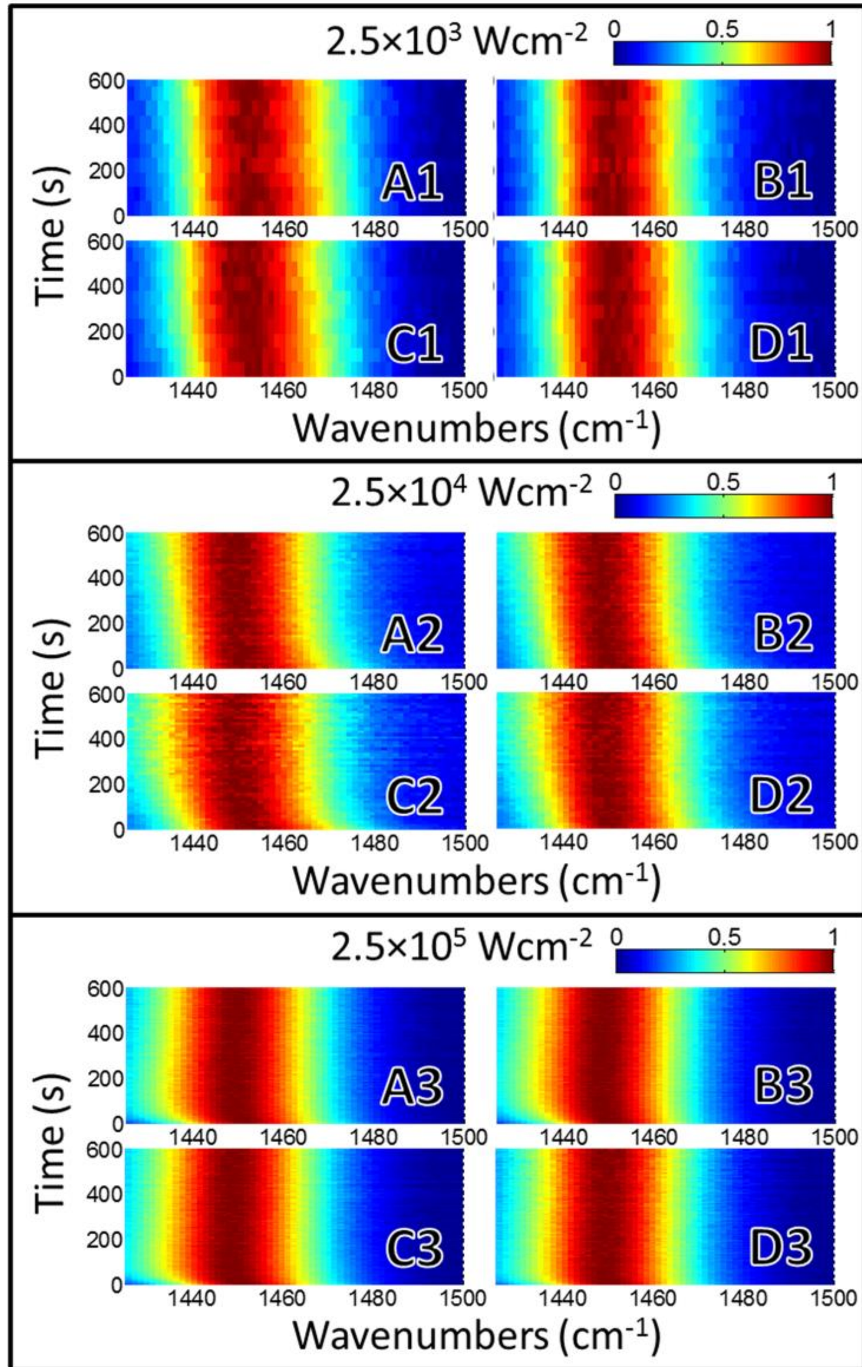

Figure 4: An expanded view of normalized P3HT Raman spectra versus illumination time for three laser power densities listed above each set of graphs. Thick film with solvent evaporation under nitrogen (A1-A3), thick film with slow solvent evaporation

المنارة للاستشارات
www.manaraa.com

under nitrogen (B1-B3), thin film with solvent evaporation under nitrogen (C1-C3), and a thin film dried under nitrogen followed by thermal annealing (D1-D3). The color scale is Raman scattering intensity.

المنارة للاستشارات

www.manaraa.com

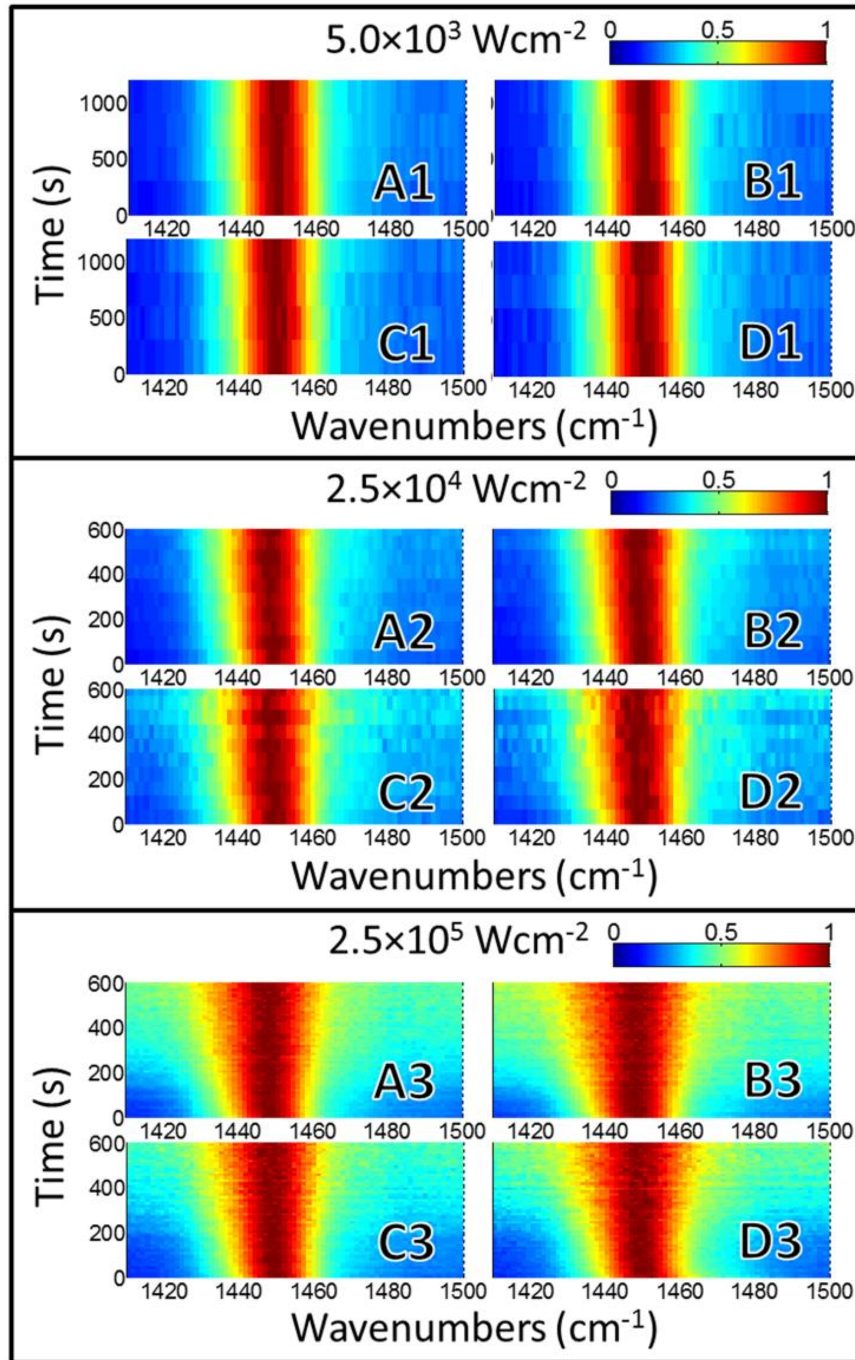

Figure 5: An expanded view of normalized PCDTBT Raman spectra versus illumination time for three laser power densities listed above each set of graphs. Thick film with solvent evaporation under nitrogen (A1-A3), thick film with slow solvent evaporation

المنارة للاستشارات
www.manaraa.com

under nitrogen (B1-B3), thin film with solvent evaporation under nitrogen (C1-C3), and a thin film dried under nitrogen followed by thermal annealing (D1-D3). The color scale is Raman scattering intensity.

المنارة للاستشارات

www.manaraa.com

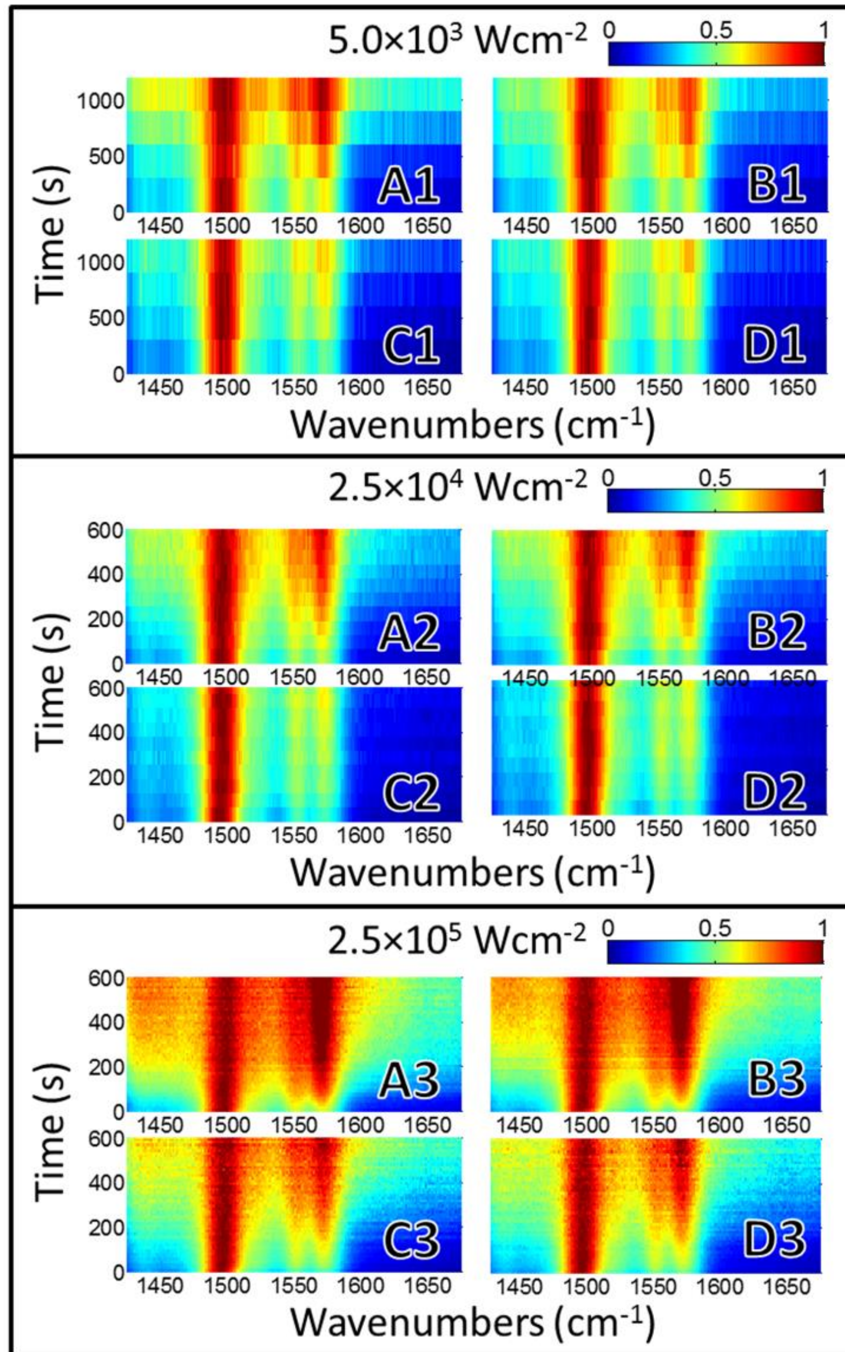

Figure 6: An expanded view of normalized PTB7 Raman spectra versus illumination time for three laser power densities listed above each set of graphs. Thick film with solvent evaporation under nitrogen (A1-A3), thick film with slow solvent evaporation

www.manaraa.com

under nitrogen (B1-B3), thin film with solvent evaporation under nitrogen (C1-C3), and a thin film dried under nitrogen followed by thermal annealing (D1-D3). The color scale is Raman scattering intensity.

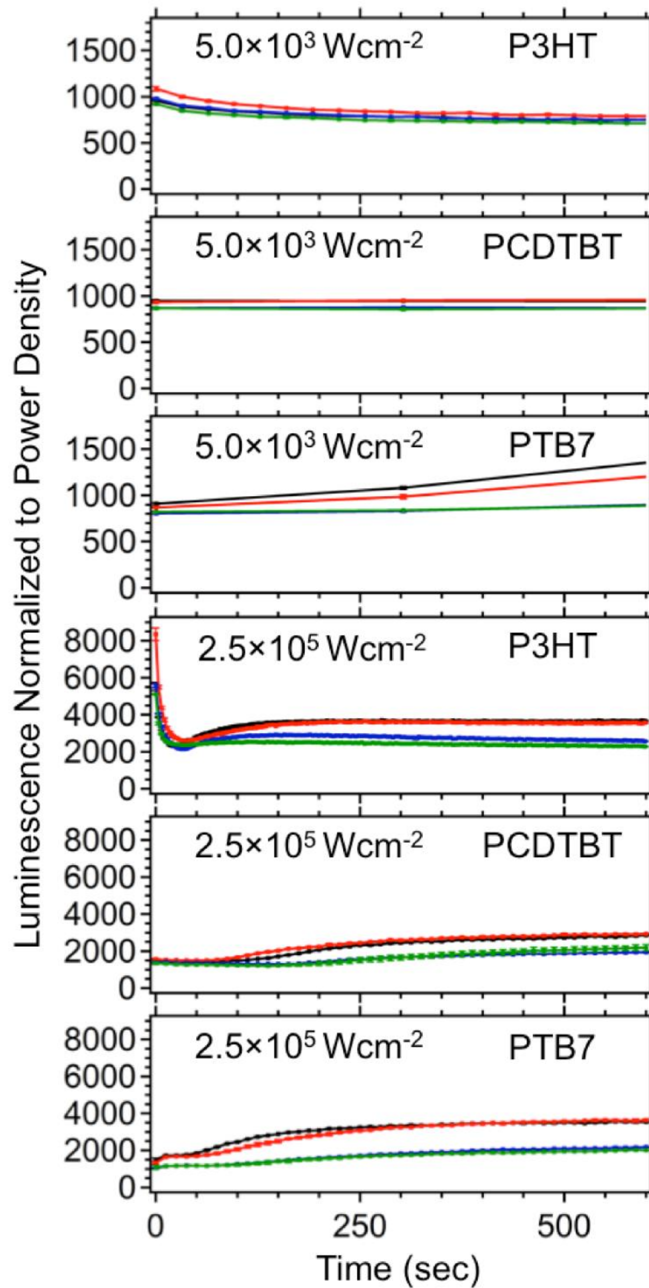

www.manaraa.com

Figure 7: Plots of background luminescence measured at 2000 cm^{-1} in the Raman spectra versus illumination time for samples fabricated with the indicated donor. The top three graphs were collected using 5.0×10^3 W cm^{-2} and the bottom three graphs with 5.0×10^3 W cm^{-2}. The color code for the samples are: thick film with solvent evaporation under nitrogen (black); thick film with slow solvent evaporation under nitrogen (red); thin film with solvent evaporation under nitrogen (blue); and a thin film dried under nitrogen followed by thermal annealing (green). Comparing the results for samples with different preparation conditions, the primary differences in the luminescence intensity is explained by film thickness (Table 1), with the thicker films producing more luminescence than the thinner films in most cases.

المنارة للاستشارات

www.manaraa.com

Table 2: Raman peak parameters measured at the start of the illumination and after 600 seconds of illumination for samples with the indicated donor, preparation condition, and power density.

Polymer	Sample	Power Density (Wcm^{-2})	FWHM (cm^{-1}) at t_0	FWHM (cm^{-1}) at t_{end}	Peak Location (cm^{-1}) at t_0	Peak Location (cm^{-1}) at t_{end}
P3HT	Fast Dry Thick	2.5×10^3	34.1 ± 0.7	35.3 ± 0.4	1454	1452
		2.5×10^4	34.4 ± 0.2	35.1 ± 0.3	1453	1449
		2.5×10^5	34.3 ± 0.1	36.3 ± 0.4	1452	1449
	Slow Dry Thick	2.5×10^3	31.3 ± 0.4	31.23 ± 0.09	1451	1451
		2.5×10^4	31.3 ± 0.2	34.8 ± 0.8	1451	1447
		2.5×10^5	32.03 ± 0.09	36.4 ± 0.5	1450	1448
	Fast Dry Thin	2.5×10^3	34.73 ± 0.07	34.0 ± 0.9	1454	1451
		2.5×10^4	35.4 ± 0.3	37.8 ± 0.8	1453	1448
		2.5×10^5	34.1 ± 0.3	36.4 ± 0.05	1451	1448
	Fast Dry Thermal Anneal Thin	2.5×10^3	32.2 ± 0.3	32.2 ± 0.5	1452	1451
		2.5×10^4	32.6 ± 0.1	36.8 ± 0.5	1451	1447
		2.5×10^5	33.6 ± 0.2	36 ± 1	1450	1449

المنارة للاستشارات
www.manaraa.com

Table 3 Continued: Raman peak parameters measured at the start of the illumination and after 600 seconds of illumination for samples with the indicated donor, preparation condition, and power density.

Polymer	Sample	Power Density (Wcm^{-2})	FWHM (cm^{-1}) at t_0	FWHM (cm^{-1}) at t_{end}	Peak Location (cm^{-1}) at t_0	Peak Location (cm^{-1}) at t_{end}
PCDTBT	Fast Dry Thick	5.0×10^3	22.2 ± 0.6	22.9 ± 0.6	1449	1448
		2.5×10^4	22.1 ± 0.2	24.0 ± 0.3	1449	1447
		2.5×10^5	23.0 ± 0.1	25 ± 1	1448	1446
	Slow Dry Thick	5.0×10^3	22.2 ± 0.3	23.3 ± 0.4	1449	1448
		2.5×10^4	22.2 ± 0.2	23.8 ± 0.2	1449	1447
		2.5×10^5	23.7 ± 0.2	25 ± 1	1447	1446
	Fast Dry Thin	5.0×10^3	22.0 ± 0.6	21.8 ± 0.8	1449	1448
		2.5×10^4	23.0 ± 0.7	26 ± 1	1448	1447
		2.5×10^5	22.4 ± 0.1	27.3 ± 0.9	1449	1447
	Fast Dry Thermal Anneal Thin	5.0×10^3	22.5 ± 0.8	22.9 ± 0.6	1449	1448
		2.5×10^4	22.9 ± 0.2	24.9 ± 0.2	1448	1447
		2.5×10^5	26 ± 3	27 ± 2	1451	1447

المنارة للاستشارات
www.manaraa.com

The background in the PTB7 spectra produced large uncertainties at long illumination times, particularly for the highest power density, and further quantification of peak properties was not performed. Despite having different FWHM values at the start of illumination, the FWHM measured for all four sample preparation methods are statistically similar after illumination with the highest power density for P3HT. This indicates that regardless of the effect of preparation conditions on the initial order, the resulting order after illumination is not dependent on the preparation conditions. This is not true for PCDTBT, which shows a correlation between film thickness and polymer order after illumination at the higher power densities. The two thinnest samples had the greatest relative disorder (FWHM 27.3 ± 0.9 and 27 ± 2 cm^{-1}) measured after illumination for power densities greater than 2.5×10^4 W cm^{-2}.

Conclusions

Laser-based studies of P3HT, PCDTBT, and PTB7 using high laser power densities can degrade the morphology or bulk heterojunction structure, which will invalidate the results of the study. This work highlights power densities and exposure times that lead to reliable resonance Raman measurements of polymer order, which varies with preparation conditions for P3HT but not PCDTBT or PTB7. Also, the measured photostability varied for P3HT, PCDTBT and PTB7. The photostability after prolonged illumination with the highest power density was not significantly different for the sample preparation conditions studied for P3HT; however, PCDTBT may exhibit a thickness dependent stability with illumination. This information can be used to design more stable devices, with the end goal of OPVs suitable for a range of real-world applications.

المنارة للاستشارات
www.manaraa.com

Acknowledgments

Raman measurements and film characterization was supported by the U.S. Department of Energy, Office of Basic Energy Sciences, Division of Chemical Sciences, Geosciences, and Biosciences through the Ames Laboratory. The Ames Laboratory is operated for the U.S. Department of Energy by Iowa State University under Contract No. DE-AC02-07CH11358. Film preparation was supported by NSF ECCS-1055930. ME was supported by the Egyptian Government through grant GM915.

References

(1) Lizin, S.; Van Passel, S.; De Schepper, E.; Vranken, L. *Sol. Energy Mater. Sol. Cells* **2012**, *103*, 1-10.

(2) García-Valverde, R.; Cherni, J. A.; Urbina, A. *Progress in Photovoltaics: Research and Applications* **2010**, *18*, 535-558.

(3) Carlé, J. E.; Krebs, F. C. *Sol. Energy Mater. Sol. Cells* **2013**, *119*, 309-310.

(4) Aïch, B. R.; Beaupré, S.; Leclerc, M.; Tao, Y. *Org. Electron.* **2014**, *15*, 543-548.

(5) Chen, D.; Nakahara, A.; Wei, D.; Nordlund, D.; Russell, T. P. *Nano Lett.* **2010**, *11*, 561-567.

(6) Grossiord, N.; Kroon, J. M.; Andriessen, R.; Blom, P. W. *Org. Electron.* **2012**, *13*, 432-456.

(7) Gregg, B. A. *Soft Matter* **2009**, *5*, 2985-2989.

(8) Wang, H.; Fukuda, T.; Ishikawa, N.; Matsuo, Y. *Org. Electron.* **2014**, *15*, 139-143.

المنارة للاستشارات

www.manaraa.com

(9) Brown, P. J.; Thomas, D. S.; Köhler, A.; Wilson, J. S.; Kim, J.-S.; Ramsdale, C. M.; Sirringhaus, H.; Friend, R. H. *Physical Review B* **2003**, *67*, 064203.

(10) Zhang, Y.; Yip, H.-L.; Acton, O.; Hau, S. K.; Huang, F.; Jen, A. K. Y. *Chem. Mater.* **2009**, *21*, 2598-2600.

(11) Zimmermann, B.; Würfel, U.; Niggemann, M. *Sol. Energy Mater. Sol. Cells* **2009**, *93*, 491-496.

(12) Hsieh, C.-H.; Cheng, Y.-J.; Li, P.-J.; Chen, C.-H.; Dubosc, M.; Liang, R.-M.; Hsu, C.-S. *JACS* **2010**, *132*, 4887-4893.

(13) He, D.; Du, X.; Zhang, W.; Xiao, Z.; Ding, L. *Journal of Materials Chemistry A* **2013**, *1*, 4589-4594.

(14) Mateker, W. R.; Douglas, J. D.; Cabanetos, C.; Sachs-Quintana, I. T.; Bartelt, J. A.; Hoke, E. T.; El Labban, A.; Beaujuge, P. M.; Frechet, J. M. J.; McGehee, M. D. *Energy & Environmental Science* **2013**, *6*, 2529-2537.

(15) Xu, X.-J.; Yang, L.-Y.; Tian, H.; Qin, W.-J.; Yin, S.-G.; Zhang, F. *Chinese Physics Letters* **2013**, *30*, 077201.

(16) Gevorgyan, S. A.; Jørgensen, M.; Krebs, F. C. *Sol. Energy Mater. Sol. Cells* **2008**, *92*, 736-745.

(17) Krebs, F. C. *Sol. Energy Mater. Sol. Cells* **2008**, *92*, 715-726.

(18) Krebs, F. C.; Spanggaard, H. *Chem. Mater.* **2005**, *17*, 5235-5237.

(19) An, L.; Duan, Y.; Yuan, Y.; Zhou, L.; Zhang, J. *Vib. Spectrosc* **2013**, *68*, 40-44.

(20) Carach, C.; Gordon, M. J. *The Journal of Physical Chemistry B* **2013**, *117*, 1950-1957.

المنارة للاستشارات
www.manaraa.com

(21) Miller, S.; Fanchini, G.; Lin, Y.-Y.; Li, C.; Chen, C.-W.; Su, W.-F.; Chhowalla, M. *J. Mater. Chem.* **2008**, *18*, 306-312.

(22) Gao, Y.; Grey, J. K. *JACS* **2009**, *131*, 9654-9662.

(23) Gao, Y.; Martin, T. P.; Thomas, A. K.; Grey, J. K. *The Journal of Physical Chemistry Letters* **2009**, *1*, 178-182.

(24) Tsoi, W. C.; James, D. T.; Kim, J. S.; Nicholson, P. G.; Murphy, C. E.; Bradley, D. D.; Nelson, J.; Kim, J. S. *J. Am. Chem. Soc.* **2011**, *133*, 9834-9843.

(25) Veerender, P.; Saxena, V.; Chauhan, A. K.; Koiry, S. P.; Jha, P.; Gusain, A.; Choudhury, S.; Aswal, D. K.; Gupta, S. K. *Sol. Energy Mater. Sol. Cells* **2014**, *120*, 526-535.

(26) Meyer, M. W.; Larson, K. L.; Mahadevapuram, R. C.; Lesoine, M. D.; Carr, J. A.; Chaudhary, S.; Smith, E. A. *ACS Applied Materials & Interfaces* **2013**, *5*, 8686-8693.

(27) Yun, J.-J.; Peet, J.; Cho, N.-S.; Bazan, G. C.; Lee, S. J.; Moskovits, M. *Appl. Phys. Lett.* **2008**, *92*, -.

(28) Furukawa, Y.; Seto, K.; Nakajima, K.; Itoh, Y.; Eguchi, J.; Sugiyama, T.; Fujimura, H. *Vib. Spectrosc* **2012**, *60*, 5-9.

(29) Furukawa, Y. *AIP Conference Proceedings* **2013**, *1554*, 5-8.

(30) Wood, S.; Garnett, O.; Tokmoldin, N.; Tsoi, W. C.; Haque, S. A.; Kim, J.-S. *Faraday Discuss.* **2014**.

(31) Wang, X.; Zhang, D.; Braun, K.; Egelhaaf, H.-J.; Brabec, C. J.; Meixner, A. J. *Adv. Funct. Mater.* **2010**, *20*, 492-499.

(32) Reish, M. E.; Nam, S.; Lee, W.; Woo, H. Y.; Gordon, K. C. *The Journal of Physical Chemistry C* **2012**, *116*, 21255-21266.

المنارة للاستشارات
www.manaraa.com

(33) Jameh-Bozorghi, S.; Il Beigi, H. S. *J. Fluorine Chem.* **2011**, *132*, 190-195.

(34) Manceau, M.; Bundgaard, E.; Carle, J. E.; Hagemann, O.; Helgesen, M.; Sondergaard, R.; Jorgensen, M.; Krebs, F. C. *J. Mater. Chem.* **2011**, *21*, 4132-4141.

(35) Tromholt, T.; Madsen, M. V.; Carle, J. E.; Helgesen, M.; Krebs, F. C. *J. Mater. Chem.* **2012**, *22*, 7592-7601.

(36) Watts, B.; Belcher, W. J.; Thomsen, L.; Ade, H.; Dastoor, P. C. *Macromolecules* **2009**, *42*, 8392-8397.

(37) Madsen, M. V.; Tromholt, T.; Norrman, K.; Krebs, F. C. *Advanced Energy Materials* **2013**, *3*, 424-427.

(38) Madsen, M. V.; Tromholt, T.; Böttiger, A.; Andreasen, J. W.; Norrman, K.; Krebs, F. C. *Polym. Degrad. Stab.* **2012**, *97*, 2412-2417.

(39) Campoy-Quiles, M.; Ferenczi, T.; Agostinelli, T.; Etchegoin, P. G.; Kim, Y.; Anthopoulos, T. D.; Stavrinou, P. N.; Bradley, D. D. C.; Nelson, J. *Nat Mater* **2008**, *7*, 158-164.

(40) Ebadian, S.; Gholamkhass, B.; Shambayati, S.; Holdcroft, S.; Servati, P. *Sol. Energy Mater. Sol. Cells* **2010**, *94*, 2258-2264.

(41) Lichang, Z.; Tang, C. W.; Chen, S. H. *Appl. Phys. Lett.* **2010**, *97*, 053305.

(42) Hu, R.; Zhang, W.; Wang, P.; Qin, Y.; Liang, R.; Fu, L.-M.; Zhang, J.-P.; Ai, X.-C. *ChemPhysChem* **2014**, *15*, 935-941.

(43) Staniec, P. A.; Parnell, A. J.; Dunbar, A. D. F.; Yi, H.; Pearson, A. J.; Wang, T.; Hopkinson, P. E.; Kinane, C.; Dalgliesh, R. M.; Donald, A. M.; Ryan, A. J.; Iraqi, A.; Jones, R. A. L.; Lidzey, D. G. *Advanced Energy Materials* **2011**, *1*, 499-504.

المنارة للاستشارات

www.manaraa.com

Supporting Information

Optical and AFM Images (Figure S1)

Atomic force microscopy (AFM) images (25×25 μm) were collected in contact mode on a Dimension ICON from Bruker (Santa Barbara, CA, USA). A Bruker sharp nitride lever AFM probe was used with a spring constant of 0.06 N/m. Standard optical bright-field microscopy was used to collect 2x-magnification optical images of the illuminated regions.

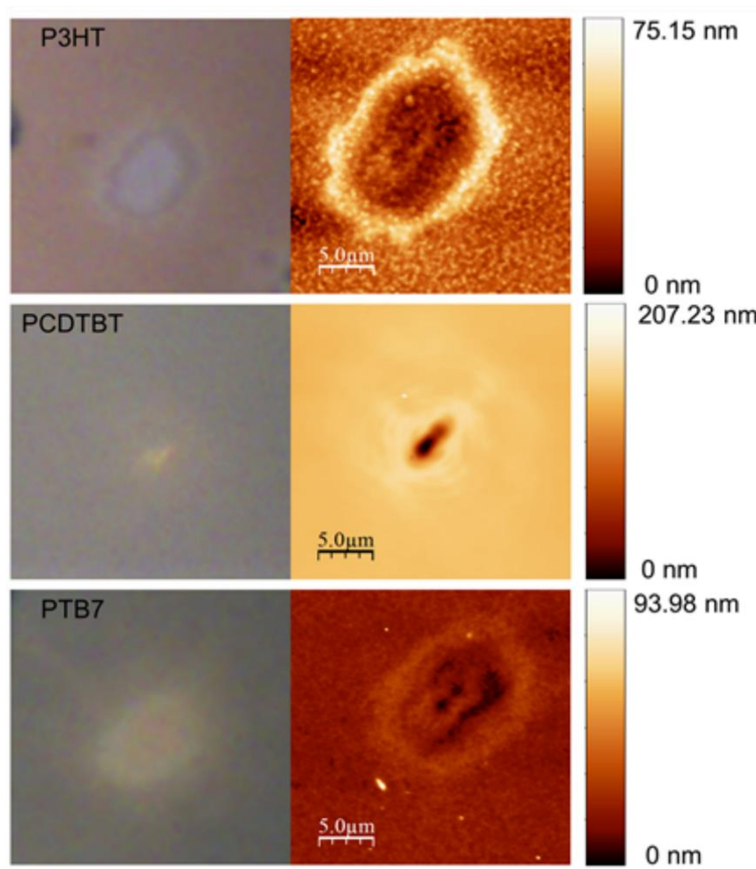

S1: Optical (left column) and AFM height (right column) images of the 600 RPM slow dry P3HT (top), PCDTBT (middle), and PTB7 (bottom) samples after illumination with a power density of 2.5×10^{5} Wcm^{-2} for 600 seconds. The optical and AFM images were

www.manaraa.com

collected at approximately the same sample location. The color scale bars for the AFM images are different due to the varying thickness of each film (as reported in Table 1) and the amount of polymer displaced by the laser beam.

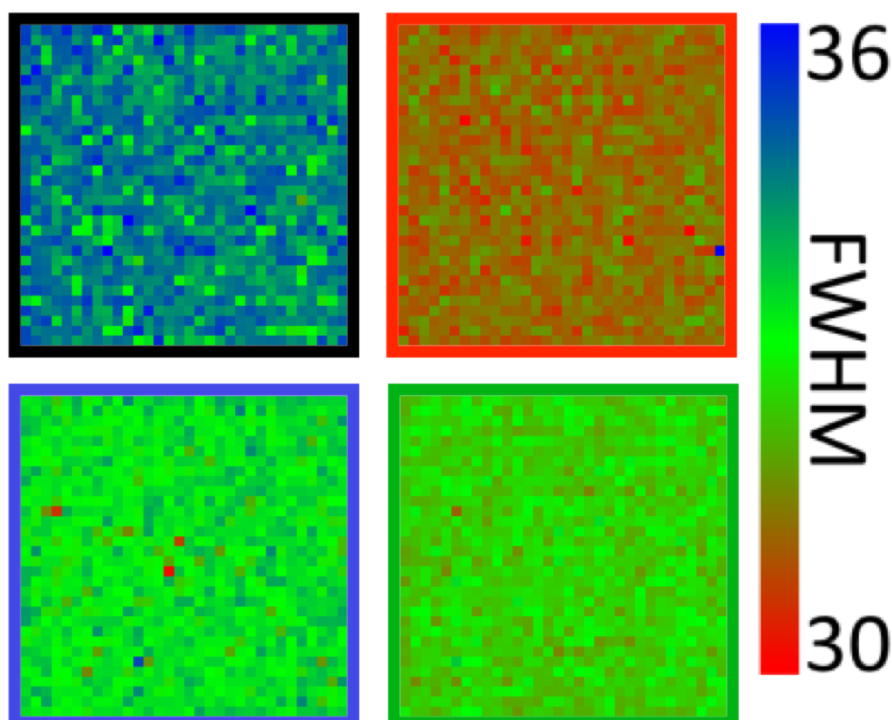

S2: Raman images of the P3HT film with the outline color coded to the preparation conditions: thick film with solvent evaporation under nitrogen (black); thick film with slow solvent evaporation under nitrogen (red); thin film with solvent evaporation under nitrogen (blue); and a thin film dried under nitrogen followed by thermal annealing (green).

المنارة للاستشارات

www.manaraa.com

APPENDIX C

CHARACTERIZING ELECTRIC FIELD EXPOSED P3HT THIN FILMS USING POLARIZED-LIGHT SPECTROSCOPIES

A paper published in M*acromol. Chem. Phys.* **2016**, *217*, 1801-1809

Ujjal Bhattacharjee,[1,§] Moneim Elshobaki,[3,§] Kalyan Santra[1], Jonathan M. Bobbitt[1], Sumit Chaudhary[2], Emily A. Smith[1], and Jacob W. Petrich[1]

[1] Department of Chemistry, Iowa State University, Ames, and U.S. Department of Energy Ames Laboratory, Ames, IA, USA

[2] Materials Science & Engineering Department, Iowa State University, Ames, IA, USA

[3] Physics Department, Mansoura University, Mansoura, Egypt

[§] Contributed equally to this work

Abstract

P3HT (poly (3-hexylthiophene)) has been widely used as a donor in the active layer in organic photovoltaic devices. Although moderately high-power conversion efficiencies have been achieved with P3HT-based devices, structural details, such as the orientation of polymer units and the extent of H- and J-aggregation are not yet fully understood; and different measures have been taken to control the ordering in the material. One such measure, which we have exploited, is to apply an electric field from a Van de Graaff generator. We used fluorescence (to measure *anisotropy* instead of

المنارة للاستشارات

www.manaraa.com

polarization, which is more commonly measured) and Raman spectroscopy to characterize the order of P3HT molecules in thin films resulting from the field. We determine preferential orientations of the units in a thin film, consistent with observed hole mobility in thin-film-transistors, and observe that the apparent H-coupling strength changes when the films are exposed to oriented electrical fields during drying.

Introduction

Π-conjugated polymers (π-CP) have been of considerable interest and applicability since their discovery.[1,2] The combination of the properties of metals and semiconductors, mechanical properties such as tensile strength, ductility, *etc.,* and the ease of processing gives these materials a very important role in the development of organic photovoltaic (OPV) devices. Among the polymers used for solar cells, P3HT (poly (3-hexylthiophene)), is the most extensively studied. The efficiency of P3HT-based solar cells typically lies in the range of 4-6 %;[3-7] and in similar polymers, such as poly[[4,8-bis[(2-ethylhexyl)oxy] benzo [1,2- b:4,5-b′]dithiophene-2,6-diyl] [3-fluoro-2-[(2-ethylhexyl) carbonyl] thieno [3,4-b] thiophenediyl]] (PTB7), an efficiency as high as ~10% has been achieved.[8]

The two main challenges that P3HT-based solar cells face are: (1) poor overlap between the absorption spectrum of P3HT and the solar spectrum; and (2) structural defects. The first can be somewhat alleviated by making the film thicker, ensuring sufficient absorption of solar light. On the other hand, owing to the small exciton-diffusion length and the large charge-transfer radius (4.8 to 9 nm), excitons reach interfaces by swift delocalization in P3HT domains instead of by diffusion.[9] Disorder in the polymer matrix, however, limits the carrier mobility.[10] Studies directed towards

المنارة للاستشارات
www.manaraa.com

reducing structural disorder and, thus, increasing carrier mobility are fundamental to enhancing the efficiency of these materials. Thermal annealing,[11-13] solvent annealing,[14,15] slow growth,[16] epitaxy,[17] and the use of shear forces,[18,19] high boiling solvents[20,21] and solvent additives[22,23] have been explored as a means to attenuate the problem. Electric fields have previously been used to align[24] or to generate a particular morphology of nanomaterials.[25] There are also a few reports in the literature concerning the orienting of P3HT "nanofibers" in microchannels by the field between two electrodes.[26,27] Attraction of the P3HT solution towards the cathode is believed to be a result of the generation of positive charge in the nanofibers owing to solvent-P3HT interaction preceding their alignment.[26,28]

There is not, however, any report concerning the orientation of P3HT polymer units using a unipolar electric field while the polymer solution is spin coated on an ITO substrate. To date, studies have only been performed on P3HT nanofibers (*i.e.*, crystalline phases). As there is a possibility of forming amorphous phases in addition to crystalline phases while the film is drying, there is the possibility of orienting the polymer units in the both phases and producing a concomitant change in charge mobility.[29] In other words, it is possible that the orientation of the P3HT polymers in the amorphous phases can also play a role irrespective of crystallinity itself, which has previously been studied in a microchannel.[26,27] While crystallinity can, of course, provide strong orientational effects, it is important to note that the carrier diffusion length in P3HT is very small (less than 2 nm[9,30,31]) and that amorphous character may be helpful in connecting nanocrystalline domains. Thus, understanding the molecular ordering of P3HT is critical when using these thin films as active layers in various electronic devices.

المنارة للاستشارات

www.manaraa.com

Here we investigate the use of steady-state and time-resolved fluorescence anisotropy along with polarized Raman spectroscopy to characterize the orientation of the polymer units. (Although several reports have appeared in the literature using polarization to investigate ordering of P3HT nanofibers,[26,27,32] our study is the first to measure the anisotropy, a quantitative measure of orientation, as rigorously defined below in equation 1.) Consistent with our anisotropy measurements, we observed an enhancement of in-plane charge mobility in the films exposed to an electric field.[29]

Barnes and coworkers have studied P3HT nanofibers with polarized time- and wavelength-resolved fluorescence microscopy.[33] They showed that the dominant inter-chain exciton coupling (H-aggregation) in low-molecular-weight nanofibers changes to predominantly intra-chain coupling (J-aggregation) for high molecular-weight nanofibers.[33] In thin films, P3HT remains a weakly coupled H-aggregate,[34,35] although varying amounts of inter- and intra-chain coupling can be observed depending on the molecular weight, processing conditions, and other parameters.[36] We show that an applied electric field can change the effective coupling strength in the polymer and that these orientational changes can be effectively probed by spectroscopic techniques using polarized light.

Experimental Section

Solution preparation

Neat P3HT (92% regio-regular) with molecular weight 70 kDa (1-Materials, Inc., Dorval, Québec, Canada) was dissolved in 1, 2-dichlorobenzene (DCB) with a dilution of 20 mg/ml. The solutions were stirred at 850 rpm on a hot plate at 50°C and then filtered.

www.manaraa.com

Substrate preparation under an E-field

Indium tin oxide (ITO)-coated glass slides (25-mm × 25-mm) (Delta Technologies, Loveland, CO) were cleaned following the method described by Chaudhary et al.[37] The solution-processed π-CP based films were subjected to an electric field immediately after they were formed by spin coating at 500 rpm for 40 s while they were still wet. This was accomplished by placing the coated substrates around a Van de Graaff dome in three different orientations: 0°, 45°, and 90° relative to the normal of the surface of the dome (**Figure 1**). The field strength was approximately 5.88 kV/m at the surface of the generator's dome, and the films were kept at a distance of approximately 1 cm from the surface of the dome. Furthermore, the degree of crystallinity in our P3HT films has been calculated following the procedure described by Hashimoto and co-workers[38]: a value of 39% is obtained (Figure S1).

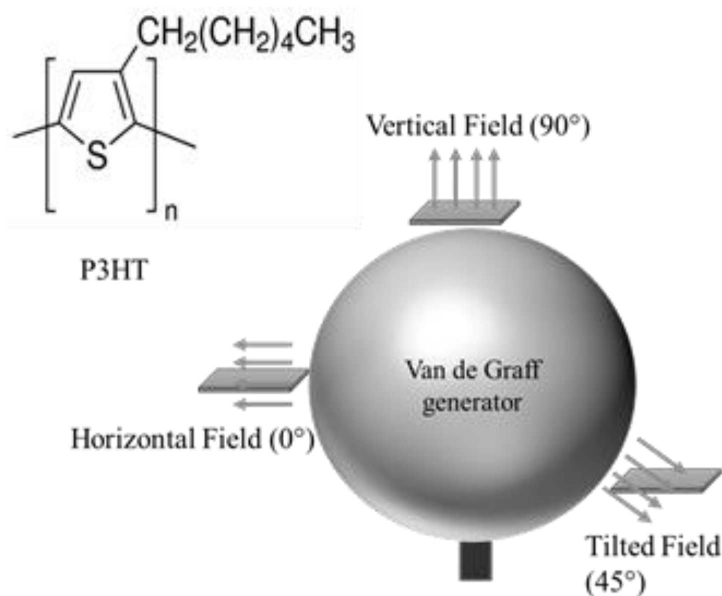

Figure 1: Diagram of the Van de Graaff electric-field generator, showing the sample placement and directions of the electric field relative to the sample. Also included is the structure of P3HT.

المنارة للاستشارات
www.manaraa.com

Steady-state fluorescence measurements: excitation anisotropy

These were performed with a Spex Fluoromax-4 with a 4- or 5-nm excitation and emission bandpass and corrected for lamp spectral intensity and detector response. The steady-state spectra were collected using a front-faced orientation. Glan-Thompson polarizers were appropriately placed before and after the sample. A 550-nm long-pass filter was used to eliminate scattered light. Excitation spectra were collected with a 720 ± 5-nm interference filter. To obtain the excitation anisotropy spectra, the films were excited with vertically polarized light, and emission polarized both parallel and perpendicular to the excitation polarization was collected. The anisotropy (r) was computed as[39,40]:

$$r = \frac{I_{||} - I_{\perp}}{I_{||} + 2I_{\perp}} \qquad (1)$$

Note that the anisotropy, as defined in equation 1, differs from a frequently used quantity, the polarization, by the presence of the 2 in the denominator. The factor of two normalizes the difference in $I_{||}$ and $I_{\perp}$ to the excited-state lifetime of the fluorophores, since the denominator in equation 1 is proportional to the excited-state lifetime.[39,40] More importantly, the anisotropy is rigorously defined to have values such that $-0.2 \leq r \leq 0.4$.[39] These limits on the value of r provide an invaluable means for gauging the precision of the experimental measurement: *e.g.*, the quality of the polarizers employed and whether they are properly aligned parallel or perpendicular to each other; the optical quality of the sample (scattering can provide spurious results); and the wavelength dependence of the grating and optics of the spectrometer.

Because the grating and optics of a monochromator may be sensitive to polarization, a correction factor must also be determined. Such a factor, g, is obtained by

المنارة للاستشارات

www.manaraa.com

taking the ratio of two spectra of a dye in solution. (Here we used ATTO 655 in water, as its absorption and emission spectra overlapped those of P3HT). Insofar as the dye can be freely rotating on the time scale of the measurement, $I_{||}$ and $I_{\perp}$ should be identical, regardless of the excitation polarization. Any differences in $I_{||}$ and $I_{\perp}$ must thus be attributed to the monochromator and detection optics. As discussed in our previous work and that of other groups,[41-44] the steady-state anisotropy, corrected for instrumental polarization dependence, is thus given by:

$$\boldsymbol{r = \frac{I_{V,V} - g\, I_{V,H}}{I_{V,V} + 2\, g\, I_{V,H}}} \qquad (2)$$

Where the notation $I_{V,V}$ indicates fluorescence obtained using excitation light polarized vertically to the plane of the table and collected vertically to the plane of the table. $I_{V,H}$, similarly, indicates vertical excitation and horizontal collection. The correction factor is given as: $g = \frac{I_{H,V}}{I_{H,H}} = \frac{I_{V,V}}{I_{V,H}}$. Measurements were repeated at least three times. The optical system was optimized by comparing results with those obtained from the excitation anisotropy of hypericin, which emits in the same region and which we had reported previously.[41]

Time-resolved fluorescence measurements

These were obtained with the time-correlated, single-photon counting (TCSPC) technique. The apparatus for time-correlated, single-photon counting is described elsewhere.[45] Our system provides an instrument response function whose full-width at half-maximum (FWHM) is ~40-50 ps. Experiments were performed in a front-faced orientation. Crossed polarizers provided an extinction of 10^5. An interference filter at 720 ± 5 nm was used to collect photons, to be consistent with the steady-state measurements.

المنارة للاستشارات
www.manaraa.com

Fluorescence lifetimes were measured with a polarizer oriented at "the magic angle," 54.7˚ to the vertical in order to prevent depolarizing events from skewing the measured fluorescence lifetime.[46] For each sample, fluorescence lifetime and anisotropy decays were measured at three random locations on the sample. Fluorescence decays were best fit to two decaying exponentials, after deconvolution with the instrument response function. The time-dependent anisotropy, $r(t)$, was constructed using the equation 1 and was well described by a single-exponential decay. The parallel and the perpendicular traces were collected for equal amounts of time, during which the incident excitation power remained constant. This resulted in the overlap of the "tails" of the parallel and perpendicular traces at sufficiently long times, thus obviating the need for "tail matching."[40,44]

Raman measurements

All Raman spectra were collected using a lab-built microscope system (Leica, Wetzlar, Germany) with a 532-nm laser excitation (Sapphire SF 532-nm 150 mW, Coherent, Santa Clara, CA) after the fluorescence measurements were completed. The laser beam was expanded with a 10× beam expander to backfill a 10× Leica microscope objective with a 0.25 numerical aperture. The laser spot size after the objective was 1.6 ± 0.2 µm. The objective was used for focusing and collecting the Raman scattering from the epi-direction and then directed to a side port on the microscope where it was focused onto an f/1.8i HoloSpec spectrograph (Kaiser Optical Systems, Ann Arbor, MI). A Newton 940 (2048 × 512 pixels) charged-coupled device (CCD) was used to detect the Raman signal (Andor Technology, Belfast, UK).

المنارة للاستشارات
www.manaraa.com

Raman spectra were collected at 5 various locations from the center of each P3HT film under ambient laboratory conditions. An XY translation-stage (ProScan, Prior Scientific, Rockland, MA) controlled by a lab-developed LabVIEW program (2010 version, National Instruments, Austin, TX) was used to move 1 mm to each new location. The spectra were collected for 10 s with 2 accumulations and illuminated with 1.09×10^4 W/cm^2, which is a low enough power density to avoid film degradation.[47] Two accumulations were used in order to remove cosmic rays.

Polarized Raman spectra were also collected on the P3HT films from the center of the film. The excitation polarization was controlled by a half-wave plate, and was set to s-polarization. A linear polarizer was placed at the side port of the microscope to collect either s- or p-polarized Raman scattering. A second linear polarizer set 45° to the collection polarizer was placed before the spectrometer to correct the spectrometer response function.[48] The ratio of the scattered light intensity with the detection polarizer set to p (I_p) to the intensity with the detection polarizer set to s (I_s) was calculated. Benzene was used to test the instrument setup (I_p/I_s 0.035 ± 0.009 at 991 cm^{-1}, 0.77 ± 0.02 at 1171 cm^{-1} and 0.783 ± 0.009 at 1588 cm^{-1}), and similar ratios were obtained to those found in literature.[48,49] The polarized spectra were collected for 30 s with 2 accumulations at a power density of 1.32×10^4 W/cm^2.

Igor Pro 6.36 (Wavemetrics, Lake Oswego, OR) was used to correct for background and to analyze the Raman spectra. The spectra were fit with a linear baseline and to a Gaussian function from 1250 to 1550 cm^{-1} with Igor Pro's batch fitting macro. The full-width at half-maximum (FWHM) and peak amplitudes were extracted from the fits.

Results and Discussion

المنارة للاستشارات

www.manaraa.com

Steady-state fluorescence measurements

Spano, Barnes, and coworkers have shown that two vibronic transitions in the steady-state fluorescence spectra of P3HT are exquisitely sensitive to the state of aggregation of the polymer chains: the 0-0 transition at ~650 nm and the 0-1 transition at ~720 nm.[50] In particular, the ratio between the intensities of these bands ($S_r = I_{0-0} / I_{0-1}$) is indicative of the resultant H- coupling strength in the polymer chain.[51] In H-aggregation, the columbic interaction arising from the side-by-side stacking of the chromophores between the chains of the crystalline films is suggested to suppress the 0-0 transition, yielding $S_r < 1$.[51] In contrast, in J-aggregation, the head-to-tail conformation of chromophores is suggested to enhance a one-dimensional intrachain interaction, increasing the intensity of the 0-0 band, yielding $S_r > 1$.[51,52] In addition, emission spectra exhibit red shifts for H-aggregation; blue shifts, for reduction of effective H-aggregation strength.

Polarized emission spectra of neat P3HT films are presented in **Figure 2**. The results are summarized in **Table I**. For emission collected parallel to the excitation polarization (**Figure 2a**), the 0-0 peak of the normalized steady-state spectra decreased with increasing angle of the applied E-field, and was always less than 1. Such low values of S_r, coupled with the spectral red-shift with increasing E-field angle, suggest H-aggregation. In contrast, for emission collected perpendicular to the excitation polarization, S_r was consistently higher than for the parallel case. This suggests an decrease of apparent H-coupling strength, which is consistent with the attendant spectral blue shift with E-field angle (**Figure 2b**).[53] Thus, the polarized emission spectra are sensitive to the extent of H- and J- aggregation of the film, induced by the applied electric

المنارة للاستشارات
www.manaraa.com

field. The values of excitonic coupling (J_0) in the different films are also given in **Table I**.[53,54]

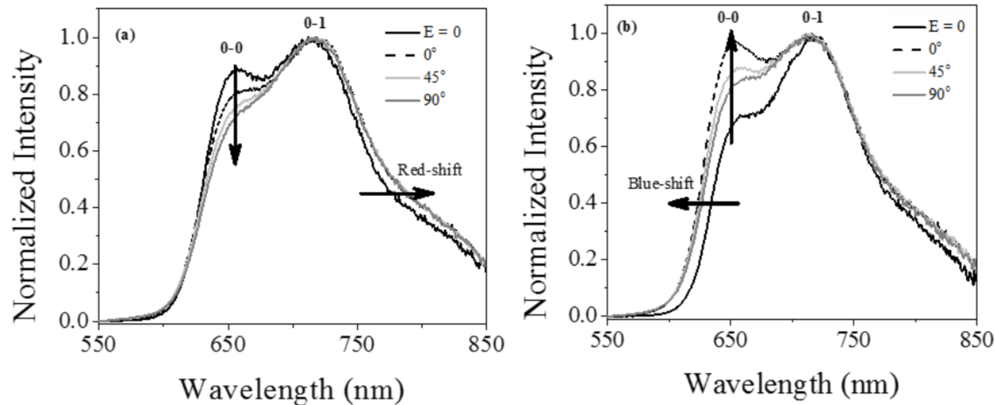

Figure 2: Polarized fluorescence emission spectra of P3HT thin films: (a) emission parallel, and (b) perpendicular to the polarization of the 520-nm excitation beam. The spectra are normalized at the 0-1 vibronic transition. $S_r = I_{0-0}/I_{0-1}$. For (a) S_r = 0.81, 0.77, 0.76 and 0.89 for angles of 0°, 45°, and 90° and for the control (E = 0), respectively. Changing the electric field orientation from 0˚ to 90˚ decreases I_{0-0}, and hence S_r, as indicated by the direction of the vertical arrow. This change in electric field also induces a red shift in the spectra, as indicated by the direction of the arrow. For (b) S_r = 0.98, 0.88, 0.85, and 0.71, for angles of 0°, 45°, and 90° and for the control (E = 0), respectively. From reference (E = 0) film to the films exposed to E-field, I_{0-0} increases, and hence S_r, as indicated by the direction of the vertical arrow. This change in electric field also induces a blue shift in the spectra, as indicated by the direction of the arrow. (The orientation of the polarizers with respect to the electric field is given in **Figure S2** for further clarification.)

www.manaraa.com

Table I: Ratio of the Intensity of the Emission of the 0-0 to 0-1 Vibronic Bands of P3HT, S_r, as a Function of Electric Field Orientation for Emission Collected Parallel and Perpendicular to the Excitation Polarization.[a]

S_r, parallel	S_r, perpendicular	J_0 (cm^{-1})[b]	Electric field angle [c]
0.89 ± 0.02	0.71 ± 0.01	267	No field (E = 0)
0.81 ± 0.01	0.98 ± 0.02	307	0˚
0.77 ± 0.01	0.88 ± 0.02	273	45˚
0.73 ± 0.01	0.85 ± 0.02	288	90˚

[a] Data summarized from the polarized fluorescence spectra presented in **Figure 2**.

[b] The excitonic coupling, J_0 is calculated using the equation, $J_0 = J_{k=0}/2$, where the excitonic shift of the $k = 0$ exciton ($J_{k=0}$) is given by: $\frac{I_{0-0}}{I_{0-1}} = \frac{\left(1-0.48\frac{J_{k=0}}{\omega_0}\right)^2}{\left(1+0.146\frac{J_{k=0}}{\omega_0}\right)^2}$.[54] ω_0 is the energy difference (in cm^{-1}) between the 0-0 and 0-1 transitions in the *absorption spectrum*, given by the *I* in the equation above. ω_0 = 1444, 1514, 1476, and 1509 cm^{-1} for E = 0 (no applied field), and for E = 0˚, 45˚, 90˚ field angles, respectively.

[c] Angles are defined for the applied electric field (E ≠ 0) as described in **Figure 1**.

Several optical methods have been used for studying the orientation of units in polymers, for example: polarized UV-Vis absorption,[17,26] polarized electroluminescence,[32] and polarized emission.[55] We note, however, that while these orientational measurements often are discussed in terms of the "anisotropy" of the sample, the anisotropy is not measured in the sense of equation 1. Because simple polarization measurements are not subject to theoretical upper and lower bounds, this renders comparisons between different experiments difficult. A good example of this difficulty is an attempt to compare our results with those of Lobov et al.[26] Although there

المنارة للاستشارات
www.manaraa.com

are differences in the methods of sample preparation (we subject P3HT films to an electric field while they are drying; they place a P3HT nanofiber solution between two electrodes), nevertheless, we only use an electric field of 5.88 kV/m while they use a field of 600 kV/m. One would expect the higher field strength to yield a greater degree of orientation, but they report very small orientational effects. It is difficult to determine the origin of this discrepancy because of the arbitrariness which simple polarization measurements are subjected to.

Also, while polarized absorption provides some information that is comparable to our fluorescence anisotropy measurements, absorption is much more subject to artifacts arising from scattering in solid samples. Scattering can become even more problematic in very heterogeneous samples. Polarized electroluminescence is limited to semiconductor materials, and it does not address the possibility of losing anisotropy in other processes, such as molecular rotation and coupling between chromophores. Also, a nonuniform electric field, an anisotropic distribution of trap states, and molecular reorientation will directly alter the electroluminescence intensity. Finally, while emission anisotropy is a powerful tool (especially if time-resolved data are acquired and if care is taken to quantify rigorously the anisotropy) it is most useful when coupled with the excitation anisotropy.

Figure 3 (right ordinate) presents the fluorescence excitation spectrum (with parallel orientation of excitation and emission polarizers) of a P3HT film in the absence of an applied electric field. The maximum of the 0-0 transition is ~615 nm. The fluorescence excitation anisotropy spectra, constructed as described above, of P3HT films prepared at angles of 0°, 45°, and 90° with respect to the E-field, are presented in **Figure**

المنارة للاستشارات

www.manaraa.com

3 (left ordinate). In all cases, the anisotropy decreases from 0.35-0.40 (0.40 being the theoretical maximum[39]) at the reddest edge of the excitation spectrum (~690 nm), to 0.10-0.17 at the bluest part of the excitation spectrum that we excited (400 nm). Our ability to attain an anisotropy near the theoretical upper limit confirms the proper alignment of our apparatus and good extinction of the excitation and analyzer polarizers. Most importantly, however, there is a clear and reproducible decrease in the anisotropy of the entire spectrum in going from an angle of the applied electric field of 0˚ to 90˚. The lowest values of the anisotropy occur when there is no applied electric field. Thus, the 0˚-film exhibits the maximum anisotropy, that is, preferential orientation of the polymeric units in the plane parallel to the substrate. This is consistent with measured hole mobility in P3HT-based transistors, which showed an enhancement: 12.1×10^{-3} cm^2 V^{-1} s^{-1} for the 0˚-film, as opposed to 7.13×10^{-3} cm^2 V^{-1} s^{-1} for the film that was not exposed to electric field.[29]

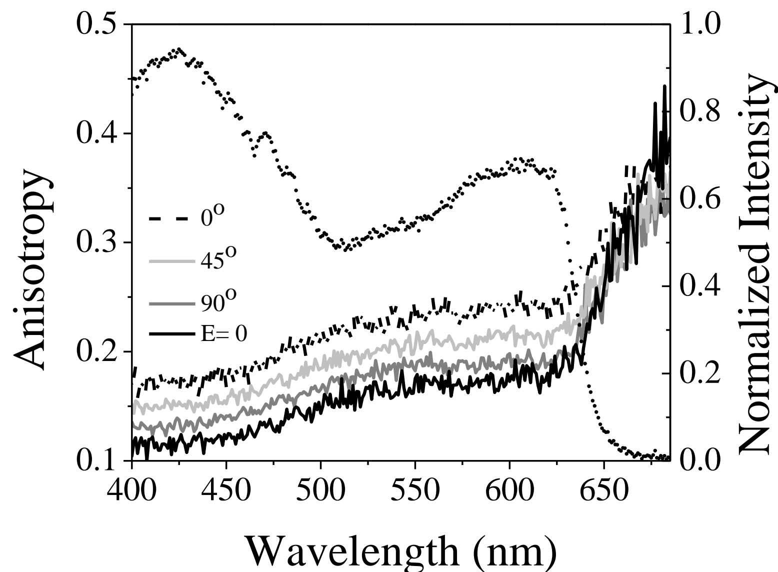

Figure 3: Fluorescence excitation spectrum of a P3HT film collected with parallel orientation of excitation and emission polarizers) (dotted curve, right ordinate).

المنارة للاستشارات
www.manaraa.com

Fluorescence excitation anisotropy of P3HT films prepared under different orientations of the applied electric field (left ordinate). $\lambda_{em} = 720$ nm.

Time-resolved fluorescence measurements: fluorescence lifetime and anisotropy decays

Time-resolved polarized emission of P3HT films is presented in **Figure 4**. The parameters for the decay of the fluorescence lifetime and anisotropy of the P3HT films are summarized in **Table II**. The average fluorescence lifetimes are 0.30, 0.25, 0.32, and 0.28 ns for the films made with E-field at 0°, 45°, 90°, and with no E-field, respectively. Time-resolved anisotropies of the films yield $r(0)$ values, that is, the anisotropies at $t = 0$, similar to those obtained from the steady-state measurements (**Table II**), as expected. This result provides another check on the accuracy of the steady-state anisotropy measurements presented in **Figure 3**. The fluorescence depolarization times, *i.e.*, the decay of the anisotropy, are on the order of a nanosecond. This is not attributed to rotational motion of the polymer film but rather to electronic coupling between the chromophores in the polymer, for which there is precedent for organic molecules.[44,56]

المنارة للاستشارات

www.manaraa.com

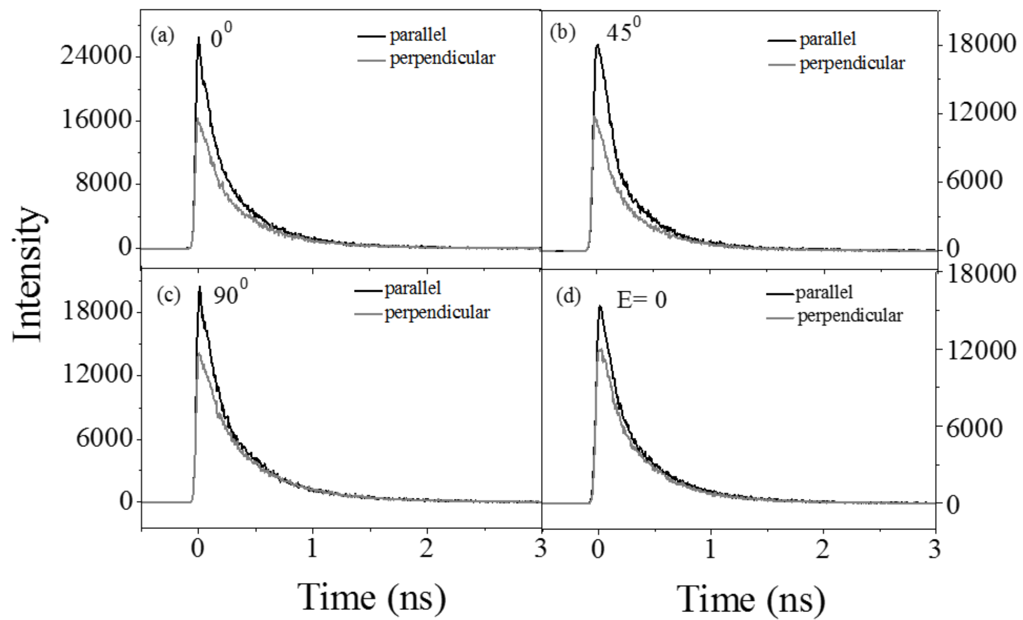

Figure 4: Time-resolved polarized emission of P3HT films prepared under (a) 0°, (b) 45°, (c) 90°, (d) and E = 0 with the emission polarizer parallel to the excitation polarizer (black), and the emission polarizer perpendicular to the excitation polarizer (gray). λ_{ex} = 425 ± 10 nm, and λ_{em} = 720 ± 5 nm.

المنارة للاستشارات
www.manaraa.com

Table II: Fluorescence Anisotropy Parameters for Oriented P3HT Films (λ_{ex} = 425 nm and λ_{em} = 720 nm).

E-field direction [a]	r_0 [b]	$r(0)$ [c]	τ_D **(ns)** [c]	τ_F **(ns)** [d]
0°	0.17 ± 0.01	0.18 ± 0.02	1.6 ± 0.4	0.30 ± 0.05
45°	0.15 ± 0.01	0.16 ± 0.01	1.3 ± 0.4	0.25 ± 0.03
90°	0.13 ± 0.01	0.12 ± 0.01	0.5 ± 0.3	0.32 ± 0.03
Reference (*i.e.*, E = 0)	0.11 ± 0.02	0.09 ± 0.02	0.7 ± 0.3	0.28 ± 0.05

[a] See **Figure 1** for the definitions of the angles specifying the E-field orientations.

[b] r_0 is the steady-state anisotropy: $-0.2 \leq r_0 \leq 0.4$

[c] Fluorescence anisotropy decays are constructed from equation 1 and fit to a single exponential of the form: $r(t) = r(0)exp(-t/\tau_D)$. $r(0)$ is the anisotropy at time zero (*i.e.*, the limiting anisotropy): $-0.2 \leq r(0) \leq 0.4$.[39] At the same excitation wavelength, r_0 should equal $r(0)$. τ_D is the fluorescence depolarization time, *i.e.*, the 1/e time at which the parallel and perpendicular curves coalesce. Factors that contribute to depolarization are molecular motion (such as rotational diffusion) or nonradiative events such as interactions between electronic states of different polarization.

[d] τ_F, the average fluorescence lifetime, *i.e.*, $<\tau_F> = A_1\tau_1 + A_2\tau_2$, where the A_i and the τ_i are the amplitudes and lifetimes of the two components in the double-exponential fit used to fit the fluorescence decay. The τ_1 and τ_2 are ~ 0.20 ns and ~ 0.62 ns, respectively in the reference film, which is consistent with the reported values in the literature.[64] The values of the two lifetime components are similar in the films exposed to electric field.

Raman measurements

المنارة للاستشارات
www.manaraa.com

Raman spectroscopy can be used to characterize polymer-based organic photovoltaic device morphology by measuring changes in the full-width at half-maximum (FWHM) and the resulting polarization of the scattered light.[47,48,57-60] Extensive work on P3HT aggregation has been reported by Grey et al.[61,62] They classify P3HT films with a ratio of the peak intensities for aggregated and unaggregated chains ($I_{1450\ cm^{-1}}/I_{1470\ cm^{-1}}$) greater than 1.5 as highly aggregated chains with correlated planarity and an average intrastack chain-to-chain spacing of approximately 3.8 Å. **Table III** presents measured parameters for the P3HT carbon-carbon double bond peak at 1450 cm^{-1} for films prepared in the absence of an external electric field, or with an electric field oriented in the noted directions. These parameters were also measured for a P3HT crystal. Representative spectra are presented in **Figure 5**. All films have statistically similar peak maxima and FWHM values. The films have $I_{1450\ cm^{-1}}/I_{1470\ cm^{-1}}$ values for both s and p polarized light ranging from 1.73 ± 0.01 to 1.923 ± 0.007. Based on the classification of Gray et al.,[61,62] these are highly aggregated chains with intra- and inter-chain order and long conjugation lengths.

www.manaraa.com

Table III: Average Peak Maximum, FWHM and Ratio of the p- to s-Polarized Scattered Light Intensity (I_p/I_s) for the 1450 cm^{-1} Band of P3HT

P3HT	Peak Max (cm^{-1})[a]	FWHM (cm^{-1})[a]	I_p/I_s
film, 0°	1450.1 ± 0.1	31.6 ± 0.3	0.490 ± 0.010
film, 45°	1449.8 ± 0.2	31.9 ± 0.4	0.490 ± 0.009
film, 90°	1449.9 ± 0.1	31.5 ± 0.2	0.499 ± 0.008
film, E = 0	1449.7 ± 0.2	32.1 ± 0.4	0.521 ± 0.007
crystal, E = 0	1453.5 ± 0.1	31.3 ± 0.3	0.512 ± 0.009

[a] The p- and s-polarized excitation spectra were averaged, as there was no statistically significant difference measured between the spectra collected with different polarizations.

The ratio of the polarized Raman scattered light is statistically lower for the 0°, 45°, and 90° films (**Table III**). Based on the work of Kleinhenz et al. and the polarized Raman data, there is an increasing order of the axis of the polymer backbone toward the orientation of the polarization of the excitation light for the 0°, 45°, and 90° films. The film prepared in the absence of an electric field (E = 0) has a statistically similar ratio of the polarized Raman scattered light as the P3HT crystal. Both fluorescence anisotropy and polarized Raman measurements show altered polymer orientation for the samples prepared in the electric field. The polarized Raman measurements, however, show no distinction between the 0°, 45°, and 90° films, indicating the fluorescence anisotropy measurement is a more sensitive technique in these cases.

المنارة للاستشارات
www.manaraa.com

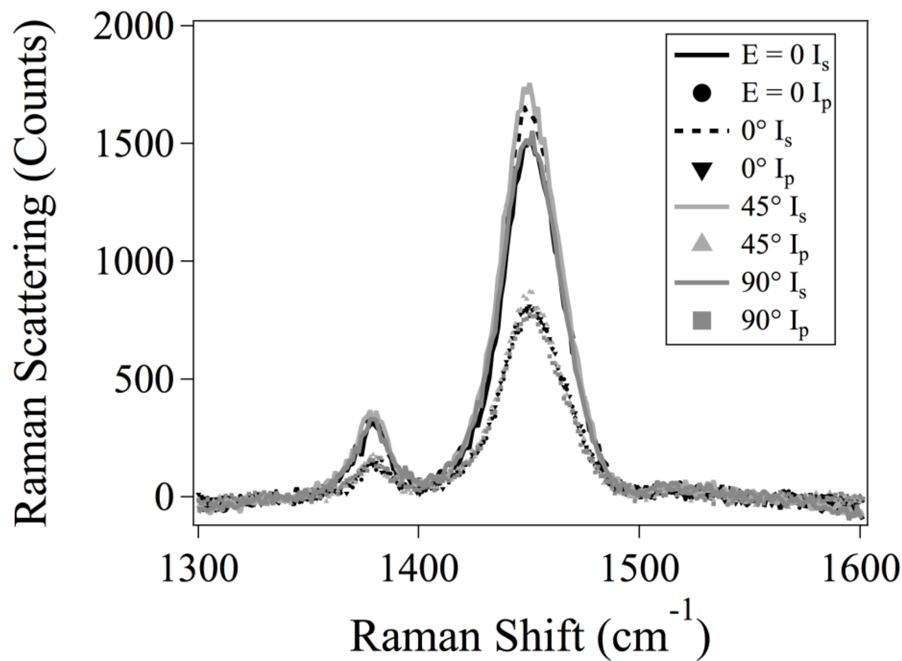

Figure 5: Example polarized Raman spectra for P3HT films oriented under an electric field. Peak location and FWHM values do not change. The relative intensities of I_p/I_s, however, do change for the samples prepared in an external electric field as reported in **Table 3**.

Conclusions

We have shown that the P3HT polymer units can be oriented when the films are subjected to a unipolar electric field of ~5.88 kV/m generated by Van de Graaff dome as they dry and that this orientation can be probed effectively by steady-state and time-resolved fluorescence anisotropy measurements. It is important to note that the degree of orientation is weak, which is likely a consequence of the relatively poor regio-regularity (92%) and the MW (which is well above the MW threshold for polymer self-folding).[17,33] Though electric fields have been used previously to align nanofibers, they were performed under a very controlled experimental conditions and in a microchannel

المنارة للاستشارات

www.manaraa.com

between two electrodes. Ours, however, is an easy and efficient method to use in conjunction with thin films prepared directly from P3HT solution *where amorphous domains are present* (degree of crystallinity is 39%), though the study by Srinivasarao and co-workers strongly suggest that this ordering is mediated by a liquid crystalline phase.[63] The highest degree of ordering, as quantified by the limiting anisotropy (r_0 for the steady-state measurement; $r(0)$, for the time-resolved measurement), is attained when the electric filed is parallel to the film, as depicted in **Figure 1**. In agreement with the anisotropy measurements, hole mobility in P3HT-based transistors increases when the films are exposed to electric field. The 0˚-film shows a 1.7-fold enhancement over control film (E = 0). The polarized emission spectra are also sensitive to the orientation of the electric field (**Figure 2** and **Table I**) as quantified by the ratio of the first two vibronic transitions, which are in turn related to the extent of H- or J-aggregation. Finally, polarized Raman experiments suggest differences between the samples in the presence and absence of electric field. Taken as a whole, these results suggest that the polymeric units of P3HT can be ordered with an electric field, that this ordering can be probed and quantified by spectroscopies using polarized light, and that applying an electric field more than 5.88 kV/m to drying films of P3HT could be beneficial in improving the performance of organic solar cells—or in systems where in-plane mobility is important.

المنارة للاستشارات

www.manaraa.com

Acknowledgements

This research is supported by the U.S. Department of Energy, Office of Basic Energy Sciences, Division of Chemical Sciences, Geosciences, and Biosciences through the Ames Laboratory. The Ames Laboratory is operated for the U.S. Department of Energy by Iowa State University under Contract No. DE-AC02-07CH11358. The work related to P3HT thin-film processing was supported by NSF (ECCS – 1055930). Moneim Elshobaki thanks the fellowship support from the Egyptian government, under the contract No. GM915.

References

(1) Shirakawa, H.; Louis, E. J.; MacDiarmid, A. G.; Chiang, C. K. H. *Chem. Comm.* **1977**, 578-580.

(2) Chiang, C. K. *Phys. Rev. Lett.* **1977**, *39*, 1098-1101.

(3) Schilinsky, P.; Waldauf, C.; Brabec, C. J. *Appl. Phys. Lett.* **2002**, *81*, 3885-3887.

(4) Padinger, F.; Rittberger, R. S.; Sariciftci, N. S. *Adv. Funct. Mater.* **2003**, *13*, 85-88.

(5) Ma, W.; Yang, C.; Gong, X.; Lee, K.; Heeger, A. J. *Adv. Funct. Mater.* **2005**, *15*, 1617-1622.

(6) Reyes, M. R.-.; Kim, K.; Dewald, J.; Sandoval, R. L.-.; Avadhanula, A.; Curran, S.; Carrol, D. L. *Org. Lett.* **2005**, *7*, 5749-5752.

(7) Zhao, G.; He, Y.; Li, Y. *Adv. Mater.* **2010**, *22*, 4355–4358.

(8) He, Z.; Zhong, C.; Su, S.; Xu, M.; Wu, H.; Cao, Y. *Nat. Photonics* **2012**, *6*, 591-595.

(9) Wang, H.; Wang, H.-Y.; Gao, B.-R.; Wang, L.; Yang, Z.-Y.; Du, X.-B.; Chen, Q.-D.; Song, J.-F.; Sun, H.-B. *Nanoscale* **2011**, *3*, 2280-2285.

للاستشارات المنارة
www.manaraa.com

(10) Noriega, R. *Nat. Mater.* **2013**, *12*, 1038-1044.

(11) Liu, Y. X.; Summers, M. A.; Edder, C.; Frechet, J. M. J.; McGehee, M. D. *Adv. Mater.* **2005**, *17*, 2960-+.

(12) Ma, W. L.; Yang, C. Y.; Gong, X.; Lee, K.; Heeger, A. J. *Adv. Funct. Mater.* **2005**, *15*, 1617-1622.

(13) Oklobia, O.; Shafai, T. S. *Sol. Energ. Mat. Sol. Cells* **2014**, *122*, 158-163.

(14) Miller, S.; Fanchini, G.; Lin, Y.-Y.; Li, C.; Chen, C.-W.; Su, W.-F.; Chhowalla, M. *J. Mater. Chem.* **2008**, *18*, 306-312.

(15) Li, G.; Yao, Y.; Yang, H.; Shrotriya, V.; Yang, G.; Yang, Y. *Adv. Funct. Mater.* **2007**, *17*, 1636-1644.

(16) Mihailetchi, V. D.; Xie, H.; de Boer, B.; Popescu, L. M.; Hummelen, J. C.; Blom, P. W. M.; Koster, L. J. A. *Appl. Phys. Lett.* **2006**, *89*, 12107.

(17) Brinkmann , M.; Hartmann, L.; Biniek, L.; Tremel, K.; Kayunkid, N. *Macromol. Rapid Commun.* **2014**, *35*, 9-26.

(18) Toney, M. F.; Russell, T. P.; Logan, J. A.; Kikuchi, H.; Sands, J. M.; Kumar, S. K. *Nature* **1995**, *374*, 709.

(19) Wittmann, J.-C.; Smith, P. *Nature* **1991**, *352*, 414.

(20) Ma, W.; Yang, C.; Gong, X.; Lee, K.; Heeger, A. J. *Adv. Funct. Mater.* **2005**, *15*, 1617-1622.

(21) Bao, Z.; Dodabalapur, A.; Lovinger, A. J. *Appl. Phys. Lett.* **1996**, *69*, 4108-4110.

(22) Chen, F.-C.; Tseng, H.-C.; Ko, C.-J. *Appl. Phys. Lett.* **2008**, *92*, -.

(23) Moon, J. S.; Takacs, C. J.; Cho, S.; Coffin, R. C.; Kim, H.; Bazan, G. C.; Heeger, A. J. *Nano Lett.* **2010**, *10*, 4005-4008.

المنارة للاستشارات
www.manaraa.com

(24) He, H.; Cai, W.; Lin, Y.; Chen, B. *Langmuir* **2010**, *26*, 8925-8932.

(25) Petchsang, N.; McDonald, M. P.; Sinks, L. E.; Kuno, M. *Adv. Mater.* **2013**, *25*, 601-605.

(26) Lobov, G. S.; Zhao, Y.; Marinins, A.; Yan, M.; Li, J.; Toprak, M. S.; Sugunan, A.; Thylen, L.; Wosinski, L.; Östling, M.; Popov, S. *Opt. Mater. Express* **2015**, *5*, 2642-2647.

(27) Fischer, F. S. U.; Tremel, K.; Sommer, M.; Crosslandbd, E. J. C.; Ludwigs, S. *Nanoscale* **2012**, *4*, 2138-2144.

(28) Tremel, K.; Ludwigs, S. *Adv. Polym. Sci.* **2014**, *265*, 39–82.

(29) Ismail, M. R. *Tailoring Device-Scale Properties in Organic Electronics: Morphological, Optical and Electrode-Interface Related Approaches*. Ph. D. Dissertation, Iowa State University, Ames, IA, 2015.

(30) Marsh, R. A.; Hodgkiss, J. M.; Albert-Seifried, S.; Friend, R. H. *Nano Lett.* **2010**, *10*, 923–930.

(31) Guo, J. M.; Ohkita, H.; Benten, H.; Ito, S. *J. Am. Chem. Soc.* **2010**, *132*, 6154–6164.

(32) Grell, M.; Bradley, D. D. C. *Adv. Mater.* **1999**, *11*, 895-905.

(33) Baghgar, M.; Labastide, J. A.; Bokel, F.; Hayward, R. C.; Barnes, M. D. *J. Phys. Chem. C* **2014**, *118*, 2229-2235.

(34) Clark, J.; Silva, C.; Friend, R. H.; F.C, S. *Phys. Rev. Lett.* **2007**, *98*, 206406.

(35) Paquin, F.; Latini, G.; Sakowicz, M.; Karsenti, P.-L.; Wang, L.; Beljonne, D.; Stingelin, N.; Silva, C. *Phys. Rev. Lett.* **2011**, *106*, 197401.

المنارة للاستشارات
www.manaraa.com

(36) Sirringhaus, H.; Brown, P. J.; Friend, R. H.; Nielsen, M. M.; Bechgaard, K.; Langeveld-Voss, B. M. W.; Spiering, A. J. H.; Janssen, R. A. J.; Meijer, E. W.; Herwig, P.; De Leeuw, D. M. *Nature* **1999**, *401*, 685-688.

(37) Elshobaki, M.; Anderegg, J.; Chaudhary, S. *ACS Appl. Mater. Interfaces* **2014**, *6*, 12196-12202.

(38) Yamamoto, S.; Yasuda, H.; Ohkita, H.; Benten, H.; Ito, S.; Miyanishi, S.; Tajima, K.; Hashimoto, K. *J. Phys. Chem. C* **2014**, *118*, 10584−10589.

(39) Fleming, G. R.; Morris, J. M.; Robinson, G. W. *J. Chem. Phys.* **1976**, *17*, 91-100.

(40) Cross, A. J.; Fleming, G. R. *Biophys. J.* **1984**, *46*, 45-56.

(41) Das, K.; Dertz, E.; Paterson, J.; Zhang, W.; Kraus, G. A.; Petrich, J. W. *J. Phys. Chem. B* **1998**, *102*, 1479-1484.

(42) Valeur, B.; Weber, G. *Photochem. Photobiol.* **1977**, *25*, 441-444.

(43) Eftink, M. R.; Selvidge, L. A.; Callis, P. R.; Rehms, A. A. *J. Phys. chem.* **1990**, *94*, 3469.

(44) Rich, R. L.; Chen, Y.; Neven, D.; Negrerie, M.; Gai, F.; Petrich, J. W. *J. Phys. chem.* **1993**, *97*, 1781-1788.

(45) Bhattacharjee, U.; Beck, C.; Winter, A.; Wells, C.; Petrich, J. W. *J. Phys. Chem. B* **2014**, *118*, 8471-8477.

(46) Fleming, G. R.; University Press: Oxford,London, 1986.

(47) Lesoine, M. D.; Bobbitt, J. M.; Carr, J. A.; Elshobaki, M.; Chaudhary, S.; Smith, E. A. *J. Phys. Chem. C* **2014**, *118*, 30229-30237.

(48) Zhao, J.; McCreery, R. L. *Langmuir* **1995**, *11*, 4036-4040.

المنارة للاستشارات

www.manaraa.com

(49) McCreery, R. L. *Raman spectroscopy for chemical analysis*; John Wiley & Sons, 2005; Vol. 225.

(50) Clark, J.; Silva, C.; Friend, R. H.; Spano, F. C. *Phys. Rev. Lett.* **2007**, *98*, 206406.

(51) Spano, F. C.; Jenny, C.; Silva, C.; Friend, R. H. *J. Chem. Phys.* **2009**, *130*, 074904.

(52) Niles, E. T.; Roehling, J. D.; Yamagata, H.; Wise, A. J.; Spano, F. C.; Moulé, A. J.; Grey, J. K. *J. Phys. Chem. Lett.* **2012**, *3*, 259-263.

(53) Spano, F. C.; Silva, C. *Annu. Rev. Phys. Chem.* **2014**, *65*, 477-500.

(54) Spano, F. C. *Acc. Chem. Res.* **2010**, *43*, 429-439.

(55) Pagliara, S.; Vitiello, M. S.; Camposeo, A.; Polini, A.; Cingolani, R.; Scamarcio, G.; Pisignano, D. *J. Phys. Chem. C* **2011**, *115*, 20399–20405.

(56) Ruggiero, A. J.; Todd, D. C.; Fleming, G. R. *J. Am. Chem. Soc.* **1990**, *112*, 1003-1014.

(57) Gao, Y.; Martin, T. P.; Niles, E. T.; Wise, A. J.; Thomas, A. K.; Grey, J. K. *J. Phys. Chem. C* **2010**, *114*, 15121-15128.

(58) Tsoi, W. C.; James, D. T.; Kim, J. S.; Nicholson, P. G.; Murphy, C. E.; Bradley, D. D.; Nelson, J.; Kim, J. S. *J. Am. Chem. Soc.* **2011**, *133*, 9834-9843.

(59) Veerender, P.; Saxena, V.; Chauhan, A. K.; Koiry, S. P.; Jha, P.; Gusain, A.; Choudhury, S.; Aswal, D. K.; Gupta, S. K. *Sol. Energ. Mat. Sol. Cells* **2014**, *120*, 526-535.

(60) Kleinhenz, N.; Rosu, C.; Chatterjee, S.; Chang, M.; Nayani, K.; Xue, Z.; Kim, E.; Middlebrooks, J.; Russo, P. S.; Park, J. O.; Srinivasarao, M.; Reichmanis, E. *Chem. Mater.* **2015**, *27*, 2687-2694.

(61) Gao, Y.; Grey, J. K. *J. Am. Chem. Soc.* **2009**, *131*, 9654-9662.

المنارة للاستشارات
www.manaraa.com

(62) Gao, Y.; Martin, T. P.; Thomas, A. K.; Grey, J. K. *J. Phys. Chem. Lett.* **2009**, *1*, 178-182.

(63) Park, M. S.; Aiyar, A.; Park, J. O.; Reichmanis, E.; Srinivasarao, M. *J. Am. Chem. Soc.* **2011**, *133*, 7244–7247.

(64) Piris, J.; Dykstra, T. E.; Bakulin, A. A.; Loosdrecht, P. H. M. V.; Knulst, W.; Trinh, M. T.; Schins, J. M.; Siebbeles, L. D. A. *J. Phys. Chem. C* **2009**, *113*, 14500–14506.

المنارة للاستشارات

www.manaraa.com

Supporting Information

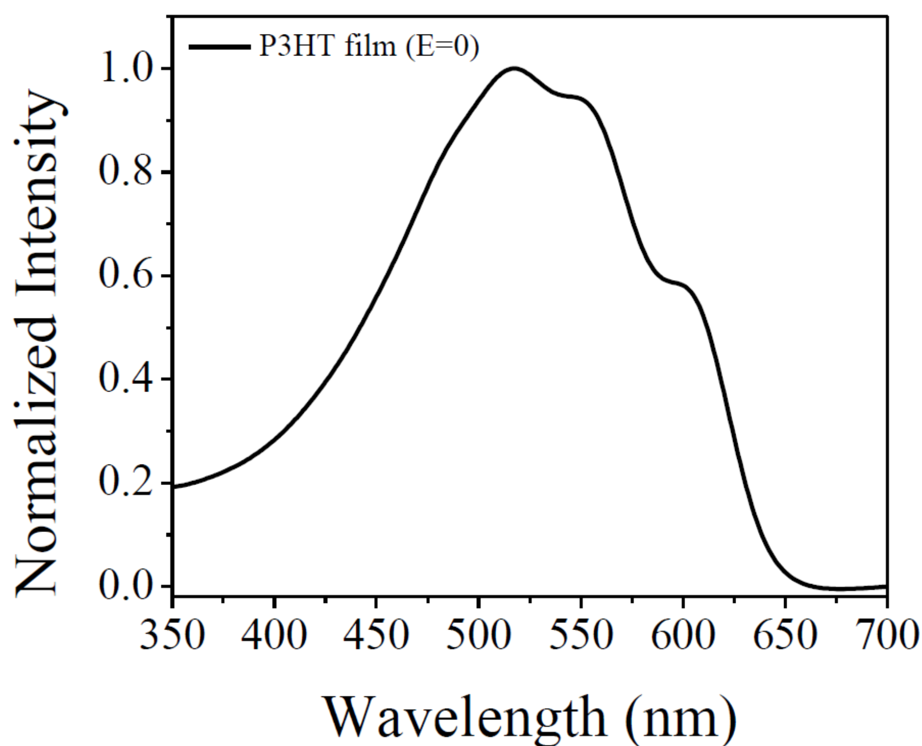

Figure S1: Absorption spectrum of reference P3HT film ($E = 0$). The absorption spectrum observed around 500-650 nm can be explained by a weakly interacting H-aggregate model[1]; and the remaining absorption at around 450 nm is largely attributed to amorphous domains present in the film. From the absorption ratio between the crystalline and amorphous regions, the degree of crystallinity, $\chi_c$has been calculated using the equation: $\chi_c = \frac{\left(\frac{\varepsilon_{460}}{\varepsilon_{600}}\right)A_{600}}{\left(\frac{\varepsilon_{460}}{\varepsilon_{600}}\right)A_{600}+A_{460}}$,[2] where $\left(\frac{\varepsilon_{460}}{\varepsilon_{600}}\right)$ (the extinction coefficient ratio) is 0.719,[1] A_{460} and A_{600} are the optical densities at 460 and 600 nm.

www.manaraa.com

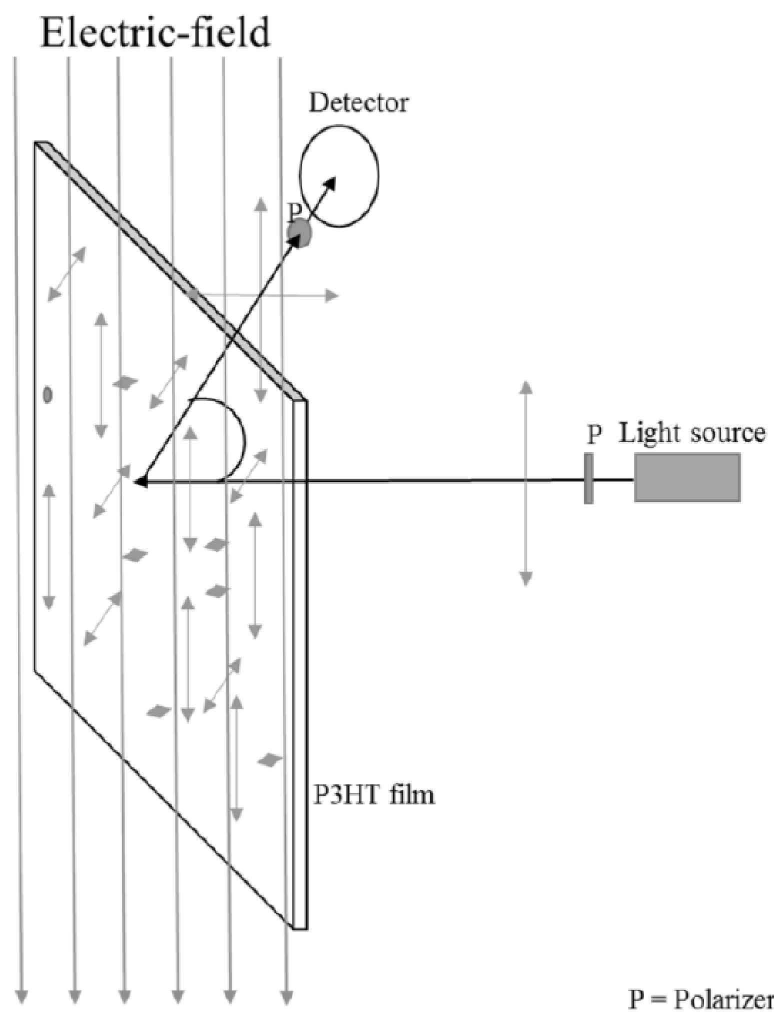

Figure S2: The orientation of the polarizers with respect to the electric field and the film. The excitation polarization is oriented along the same direction of the electric field (0°).

References

(1) Clark, J.; Chang, J.-F.; Spano, F. C.; Friend, R. H.; Silva, C. *Applied Physics Letters* **2009**, *94*, 117.

(2) Yamamoto, S.; Yasuda, H.; Ohkita, H.; Benten, H.; Ito, S.; Miyanishi, S.; Tajima, K.; Hashimoto, K. *The Journal of Physical Chemistry C* **20A14**, *118*, 10584-10589.

www.manaraa.com